

A comprehensive screening of plasma-facing materials for nuclear fusion

Andrea Fedrigucci^{1,2}*, Nicola Marzari^{1,3}, and Paolo Ricci²

¹*Theory and Simulation of Materials (THEOS), and National Centre for Computational Design and Discovery of Novel Materials (MARVEL),*

École Polytechnique Fédérale de Lausanne (EPFL), Lausanne CH-1015, Switzerland

²*Swiss Plasma Center (SPC), École Polytechnique Fédérale de Lausanne (EPFL), Lausanne CH-1015, Switzerland*

³*Laboratory for Materials Simulations, Paul Scherrer Institut, Villigen PSI 5232, Switzerland*

Plasma-facing materials (PFMs) represent one of the most significant challenges for the design of future nuclear fusion reactors. Inside the reactor, the divertor will experience the harshest material environment: intense bombardment of neutrons and plasma particles coupled with extremely large and intermittent heat fluxes. The material designated to cover this role in ITER is tungsten (W). While no other materials have shown the potential to match the properties of W, many drawbacks associated with its application remain, including: cracking and erosion induced by a low recrystallization temperature combined with a high ductile–brittle transition temperature and neutron-initiated embrittlement; surface morphology changes (He bubbles and fuzz layer) due to plasma-W interaction with subsequent risk of spontaneous material melting and delamination; low oxidation resistance in case of air contamination. Exploring alternatives to W requires the design of a multivariable optimization problem. This work aims to produce a structured and comprehensive materials screening of PFMs candidates based on known inorganic materials. The methodology applied in this study to identify the most promising PFM candidates combines peer-reviewed data present in the Pauling File database and first-principle DFT calculations of two key PFMs defects, namely the surface binding energy and the formation energy of a hydrogen interstitial. The crystal structures and their related properties, extracted from the Pauling File, are ranked according to the heat-balance equation of a PFM subject to the heat loads in the divertor region of an ITER-like tokamak. The materials satisfying the requirements are critically compared with the state-of-the-art literature, defining an optimal subset where to perform the first-principles electronic structure calculations. The majority of previously known and extensively studied PFMs, such as W, Mo, and carbon-based materials, are captured by this screening process, confirming its reliability. Additionally, less familiar refractory materials suggest performance that calls for further investigations.

I. INTRODUCTION

One of the major challenges on the way to fusion energy - one of the few options we have to provide mankind with a large-scale, sustainable and carbon-free energy source [1, 2] - is linked to the availability of in-vessel plasma-facing materials (PFMs) capable to sustain the severe operational condition of a fusion power plant [3] for an assumed lifetime of 1-2 full power years (fpy) [4, 5]. In particular, in modern tokamaks, such as ITER [6], the most external magnetic field lines are deviated toward the divertor, and the thermal loads that the divertor must withstand are the highest of all the components facing the plasma, making it one of the most challenging parts to build [7]. The divertor is expected to exhaust the heat and control the level of helium ash and other impurities, mainly resulting from erosion of the plasma-exposed surface, to minimize plasma contamination. In addition, the divertor protects the most delicate surrounding components from neutronic loads. The heat load on the divertor primarily results from a combination of five types of loads: ionic, neutral, radiation power, electrons, and surface recombination energy of incoming ion-electron pairs [8]. The power deposited on the divertor surface is dom-

inated by radiative and particle fluxes, with the latter mainly constituted by helium (He), hydrogen isotopes (deuterium and tritium), and impurities. Their flux at the divertor is the highest of the vacuum vessel, 10^{24} particles $\text{m}^{-2} \text{s}^{-1}$ with an average kinetic energy of 10 eV (during steady-state) [9, 10]. Last, 14.1 MeV neutrons bombard the PFM with a flux of 10^{18} particles $\text{m}^{-2} \text{s}^{-1}$ [9].

In ITER the thermal load at the divertor in quasi-stationary conditions is estimated to oscillate between 10 MW m^{-2} , in steady-state conditions lasting around 400 s, and 20 MW m^{-2} , during the slow-transient thermal loads, where a transition from detached divertor operation to fully attached operation is observed (< 10 s) [9, 11]. Moreover, intense and short transient loads are predicted to occur due to edge-localized modes (ELMs), that are quasi-periodic fluctuations of the plasma pressure at the plasma edge [9]. The thermal energy released on the divertor target during unmitigated ELMs can be as high as $10\text{--}15 \text{ MJ m}^{-2}$ with a frequency of 1-2 Hz and a duration of 0.1-1 ms [12-16]. In fact, ELM mitigation is required in ITER, and it will be based on increasing ELM frequency to 25-50 Hz, consequently lowering their heat flux to around 0.5 MJ m^{-2} and reducing the heat peak from tens to tenths of GW m^{-2} [12, 17, 18]. Finally, off-normal events, which may not be excluded during ITER operations, include vertical displacement events (VDEs), which result in energy pulses up to 30 MJ m^{-2} in 1-5 ms,

* andrea.fedrigucci@epfl.ch

plasma disruption, which can reach around 60 MJ m^{-2} and last 100–300 ms, and runaway electrons, which lead to 50 MJ m^{-2} pulses for less than 50 ms [9, 15, 19]. The simultaneous thermal, plasma, and neutron wall loads lead to complex dynamics and degradation process of the divertor armor. The initial ITER divertor design included both carbon fiber composite (CFC) and tungsten (W) as PFM, but given the high-level of tritium retention and surface erosion, the ITER Organization (IO) decided to switch to a fully W divertor since 2013 [20, 21]. While W has the highest melting point of all the metals and outstanding thermal properties, it suffers of (i) low recrystallization temperature combined with high ductile–brittle transition temperature (DBTT); (ii) neutron-induced embrittlement that leads to cracking and erosion of the W surface at high thermal loads; (iii) surface morphology changes (He bubbles and fuzz layer) due to plasma-W interaction with subsequent risk of spontaneous material melting and delamination; (iv) neutron-induced damages and transmutation affecting thermal and mechanical properties; and (v) low oxidation resistance in case of air contamination [7, 22]. While the PFM community is working to propose solutions for some of these issues, it is still unclear if a W-based divertor will be able to sustain operating fusion conditions in a fusion power plant. For instance, the design of the divertor is still open for DEMO [23], the power plant that will demonstrate the production of electric power from nuclear fusion. The primary PFM of DEMO divertor will withstand the same thermal loads as the one in ITER, but higher neutron loads (from $0.37\text{--}0.47 \text{ MW m}^{-2}$ to $1.8\text{--}2.4 \text{ MW m}^{-2}$) [24, 25]. The same risks previously mentioned related to erosion, melting, and cracking of the W surface will be faced. The more intense neutron bombardment will also lead to stronger displacement damage and transmutation effects, resulting in swelling, irradiation hardening, and radioactivity after exposure. These challenges pose even greater difficulties in the material choice for DEMO and future commercial fusion reactors.

Given the high cost and time required for both testing or simulating PFM in such a complex environment [26–28], only few classes of materials have been evaluated as potential alternatives to W [29] and a high-throughput protocol for PFM screening is missing in the literature. This multivariable optimization problem requires to define a set of design criteria that a material need to satisfy in order to sustain divertor conditions. In this study we define the first methodology to assess the potential of a large class of materials as PFM. The heat loads that PFM must endure are modeled using a heat balance equation, which takes into account both steady-state and transient loads. The thermal properties involved in this equation, such as thermal conductivity, melting temperature, heat capacity, and other related proxies are extracted from the inorganic crystal database MPDS [30], an online platform providing access to the PAULING FILE [31], which contains the peer-reviewed properties of, approximately, half a million

experimentally-confirmed structures. The best performing materials are ranked and then selected to calculate, in the framework of density-functional theory calculations (DFT) [32], surface binding energies (SBE), which are a proxy of the required energy for physical sputtering and therefore the erosion rate, and the hydrogen interstitial formation energies (H-IFE), as an indication of the hydrogen solubility into the crystal [33] and therefore its tritium retention.

The impact of neutron bombardment is not explored here, due to the significant computational burden associated with modeling its effects on candidate materials. Studies in the literature, such as those in Ref. [34, 35], have calculated the radioactivity of pure chemical elements following neutron bombardment in DEMO-like reactors. This information could serve as an additional design criterion, as threshold values have been proposed [36].

The paper is organized as follows. In Sec. II, we discuss the design criteria, data processing of the data extracted from MPDS, and the ranking procedures used to select the PMFs. In Sec. III, we show the best candidates emerging from the ranking criteria and in Sec. IV we present a comprehensive literature review on their applicability as PFM. Only the materials that pass both selection procedures undergo ab-initio calculations of SBE and H-IFE, and their results are presented in Sec. V. In Sec. VI we offer a conclusive evaluation of the top PFM candidates. Finally, Sec. VII provides a perspective on the development of the field of PFM.

II. METHODS

The set of design criteria needed for finding an exhaustive list of PFM candidates should include the effects produced by the three loads on the exposed material: heat, neutrons, and plasma particles. In this work, a first material screening, we consider known or easy-to-compute properties of experimentally observed crystal, therefore excluding the analysis of complex dynamics emerging at the atomic-scale level from degradation processes. The design criteria include the constraint dictated by thermal loads (Sec. II A), and the plasma-wall interactions (Sec. II B). For the heat load, the heat balance equation of a solid material exposed to a base load of steady-state heat flux and short-transient loads (ELMs) is being investigated as the primary design criterion. In Sec. II A 1, the maximum thickness that a given material possesses to avoid surface’s melting is used as first ranking procedure of the material retrieved from MPDS. If this cannot be estimated due to a lack of available properties, the concepts of Pareto fronts and win-fraction are defined in Sec. II A 2 to determine how materials performs in terms of thermal properties. To compare the consistency of the two ranking procedures the idea of a comparative ranking is presented in Sec. II A 3. Plasma-wall interactions are then explored by calculating the

formation energy of two common PFM defects, the surface binding energy (SBE) and the hydrogen interstitial formation energy (H-IFE). The relations between these crystal defects, the sputtering phenomena, and the tritium retention process are explained in Sec. II B 1 and II B 2, together with the Python workflows built to automate the first-principle calculation of these properties starting from a crystal structure.

A. Thermal loads

All materials-related data of this section are retrieved from the inorganic crystal database MPDS [30]. In MPDS multiple values can be associated to a single material property. Indeed, the database is composed of entries, and each entry corresponds to the value of a peer-reviewed measured (or, occasionally, calculated) property of a specified crystal. Multiple entries for the same property and material can differ because of their literature reference and/or experimental or simulated conditions, which are not always reported. For this reason, in this work, the value of a property of a material is defined through the use of the kernel density estimation method (KDE) [37]. This choice is based on the empirical observation that most of the reported values of a given property are around standard conditions ($T = 298$ K, $P = 1$ atm). The KDE creates a probability density function estimation, f , from the finite data sample of the available entries, x_i , that is:

$$f(h, x) = \sum_{i=1}^n K(x - x_i; h) \quad (1)$$

where h is the bandwidth parameters setting the level of smoothness of $f(h, x)$ ($h = 0.05$ in this work) and K is a kernel function (here a Gaussian $K = \exp[-9(x - x_i)^2/(2h^2)]$). The value of a property of a crystal used in this study is thus obtained as the value that maximises $f(h, x)$, unless otherwise specified. We note that some entries are calculated under high-pressure conditions; sometimes, MPDS identifies such entries with the "hp" flag in the crystal structure chemical formula. All entries with the "hp" flag are excluded from the screening process. In addition, 17 more materials, selected based on ranking criteria, are excluded from the dataset because their reported properties are measured under high-pressure conditions, as indicated in the literature references provided within the database.

The underlying assumption of the design criteria defined in this section is that a candidate material cannot melt during the steady-state (SS) tokamak operating conditions and ELM events, in order to keep its shielding functions and to avoid plasma contamination. In SS conditions the heat flux Φ_q to the PFM equals the heat flux that is removed on the cooling side, by assuming one dimensional thermal conduction through a material of thickness d [38]:

$$\Phi_q^{SS} = \frac{1}{d} \int_{T_{bott}}^{T_{surf}^{SS}} k(T) dT \quad (2)$$

where T_{surf}^{SS} and T_{bott} are the temperature on the plasma-facing and the cooling sides. Assuming constant thermal conductivity $k(T) = \langle k(T) \rangle$, Eq. (2) leads to:

$$T_{surf}^{SS} = T_{bott} + \Phi_q^{SS} \frac{d}{\langle k(T) \rangle} \quad (3)$$

In contrast, during short thermal transients, such as ELMs, the heat is deposited on the surface as a power pulse. The temperature at the end of the ELM event (T_{surf}^{ELMs}) can be estimated as:

$$T_{surf}^{ELMs} = T_{surf}^{SS} + \Phi_q^{ELMs} \sqrt{t} \frac{2}{\sqrt{\pi \rho \langle C_p(T) \rangle \langle k(T) \rangle}} \quad (4)$$

if the penetration depth d^* of the heat in the material surface is smaller than the material thickness d [39]:

$$d \geq d^* = 2\sqrt{t} \sqrt{\frac{\langle k(T) \rangle}{\rho \langle C_p(T) \rangle}} \quad (5)$$

where t is the duration of an ELM event, Φ_q^{ELMs} is the power flux density during ELMs, $\langle C_p(T) \rangle$ is average heat capacity of the material and ρ its density. Eq. (4) can be used to define a filter to assess the potential of a material to withstand the divertor thermal loads without melting ($T_m > T_{surf}^{ELMs}$), having excluded off-normal events. The material-dependent properties appearing in Eq. (4) are retrieved from the MPDS database. The thickness d is a target parameter, that is partially constrained by the erosion rate at the divertor, its assumed lifetime (e.g. twice as much CFC is needed compared to W metal [40] for a comparable lifetime of the armor material), and the material response to thermal stress.

Two ranking procedures are then pursued to select the most promising PFM candidates. The first is the direct application of the heat balance equations and is called thickness ranking; the second builds on the various material-related properties extrapolated from the same equations and selects materials based on a Pareto optimization procedure refined by a win-fraction ranking equation, and is called Pareto ranking. A third ranking procedure is applied with the main goal of comparing the accuracy of the two ranking methods and establish a unique ranking for all the materials retrieved from MPDS, which we denote as comparative ranking.

1. Thickness ranking

The first ranking method comes directly from the application of the heat balance equation in Sec. II A. The

TABLE I. Input parameters used to compute the heat balance equations: Eq. (3), (4) and (5).

Parameter	Unit	Value	Ref.
T_{bott}	K	415	[41]
Q^{SS}	MW m ⁻²	20	[9, 17]
t	ms	0.5	[12, 17]
Q^{ELMs}	GW m ⁻²	1	[12, 17]

list of materials for which is possible to collect all the variables in Eqs. (4) and (5) are ranked accordingly to the maximum thickness allowed to avoid melting during type-I ELMs (d^{ELMs}). If $C_p(T)$ is not available, then the maximum thickness allowed to avoid melting during steady-state (d^{SS}) is used as ranking criterion. The input values assumed to compute the material thickness are reported in Tab. I.

Given the large uncertainty around the real value of each property extrapolated from MPDS, the thicknesses calculated from Eqs. (3) and (4) are reported with a standard deviation (SD) that is obtained by the propagation of the standard deviation of every single property. Materials with $d^{ELMs} > 0$ mm and $d^{ELMs} - d^* > 0$ mm and materials with $d^{SS} \geq 3$ mm are considered PFM candidates; materials not passing this test are discarded. The threshold value of 3 mm for steady-state conditions is chosen since no material with a positive d^{ELMs} has a lower d^{SS} thickness.

It is important to remember that these values are calculated using three assumptions: (i) the value at the maximum of the KDE probability density function captures well the real value of the material property, (ii) these properties remain constant over large temperature ranges, (iii) degradation processes and materials defects are neglected. Therefore, the calculated d^{ELMs} and d^{SS} remain indicative of a trend and should not be considered for the engineering design.

2. Pareto ranking

For materials where neither d^{ELMs} nor d^{SS} can be calculated a ranking process that does not require the knowledge of an objective function is used. This is performed in order to extract materials from MPDS that are showing promising performance in a subset of the properties identified through thermal balance analysis. In order to expand the number of available PFM candidates, the properties retrievable from MPDS that showed a high Pearson correlation coefficient (≥ 0.7) with T_m , k , C_p are added to the list of properties. Of all the properties available on MPDS, T_m shows a Pearson correlation coefficient greater or equal than 0.7 along with 6 other properties: shear modulus (G), Young's modulus (E), adiabatic and isothermal bulk modulus (B_S and B_T), Mohs hardness (MH), Knoop hardness (KH); C_p with the heat capacity at constant volume (C_v). At

TABLE II. The 10 properties (p) retrieved from MPDS are classified into 3 categories (c). This classification is applied inside the Pareto and comparison ranking systems.

Category (c)	Property (p)
	T_m
	G
	E
Melting temperature + proxies	B_S
	B_T
	MH
	KH
Thermal conductivity	k
Heat capacity	C_p
	C_v

this stage, the total number of properties is 10 and they are categorized as follows: (i) melting temperature + proxies, (ii) thermal conductivity, (iii) heat capacity (at constant pressure and constant volume). In the following, for the sake of clarity, these 3 macro-categories are identified with the term categories (c), whereas the 10 features are called interchangeably features or properties (p) (see Tab. II). Note that the density is always available for every crystal structure reported in MPDS, therefore instead of using the heat capacity in molar units, it is converted in unit of volume as Eq. (4) suggests.

A rigorous way to treat an optimization problem for which the objective function is unknown is through the so-called Pareto set (or Pareto front), a collection of solutions (i.e. materials) that cannot be improved in one objective (i.e. property) without worsening at least one of the others [42]. Given a set of materials m of size M that share the same set of properties p of size P , the Pareto set \mathcal{P} of this system is defined as follow:

$$m_i \in \mathcal{P} \Leftrightarrow \nexists m_j : \begin{cases} p_{j,k} \geq p_{i,k} & \forall k = 1, \dots, P \\ \exists k_0 : p_{j,k_0} > p_{i,k_0} & \end{cases} \quad (6)$$

$$\forall i, j = 1, \dots, M$$

First, upstream of the Pareto optimization process, the data are standardized by subtracting its mean, so that the mean of the standardized values vanishes, and divided by the standard deviation of the standardized values is one. Then, different sets of materials that posses the same set of properties to apply the Pareto optimization are defined. Since the whole set of 10 p is not available for all the materials, it is crucial to define their subsets for which a Pareto set optimization is pursued. Here, we apply Pareto for every material possessing at least 1 property out of the 10 previously defined. Therefore, three subsets of materials are defined as follows: $3p$, which includes materials possessing at least one property for each of the three category; $2p$, which encompasses materials having at least one property in, at least, two different category; and $1p$, which includes materials with only one property per category. Then, for every subset of $3p/2p/1p$, all possible combinations of n properties that belong to n

TABLE III. A Pareto ranking is utilized to identify the most promising candidates that do not meet the criteria for thickness ranking due to insufficient retrievable properties. The materials were categorized into three subsets based on the number of available properties. For each subset, the first l Pareto fronts were selected, and only those with a WF_i 7 value exceeding a specified threshold were considered as PFM candidates.

Material class	l	WF_i
3p	≤ 5	$\geq 50\%$
2p	≤ 5	$\geq 70\%$
1p	≤ 100	$\geq 90\%$

different categories are used to define the feature space. For instance, in the 3p subset an allowed combination of features can be either T_m - C_p - k or T_m - C_v - k but not T_m - B_S - k or T_m - C_v - C_p since T_m - B_S and C_v - C_p are part of the same category (respectively melting temperature + proxies and heat capacity).

If the number of features is exhaustive for the description of a given problem, any solution that is not a Pareto front can be discarded from the list of interesting candidates, because it is worse in terms of performance. In the context presented here, the list of properties used as design criteria for an armor divertor material is far from being comprehensive; therefore, multiple Pareto set are considered as optimal solutions. Once a Pareto set is found, it is discarded from the list of candidates and those are re-evaluated. Each Pareto set can be conceptualized as a Pareto layer (l), which, once identified, is peeled off, and the subsequent layer is selected. This process is repeated for a specified number of cycles.

To distinguish between any of the candidates thus selected, the concept of win fraction, as proposed in Ref. [42], is revisited and applied.

$$WF_i = \frac{\sum_j \sum_k |p_{i,k} - p_{j,k}| \times \mathcal{H}(p_{i,k} - p_{j,k})}{\sum_j \sum_k |p_{i,k} - p_{j,k}|} \quad (7)$$

where WF_i is the win fraction of material i , $p_{i,k}$ is the value of the property k of material i and $\mathcal{H}(x)$ is the Heaviside step function that is equal to 0 for $x < 0$ and to 1 for $x > 0$. Contrary to the original reference, the ranking equation is not defined as the smallest win fraction that each materials i posses when compared with the other candidates j ; instead, it corresponds to a summation extended over all candidates of the selected Pareto fronts. In addition, it is implied that an unitary weight is assigned to every property of the summation. Once the ranking is pursued, the best candidates are selected. The number of Pareto sets l and the threshold value of WF_i used to identify the best candidates for each category of Pareto solutions is reported in Tab. III.

In order to avoid false positive, materials discarded from more stringent criteria of selection should not be captured by weaker filters. Hence, materials that are excluded by the thickness ranking scheme or by a Pareto

optimization with a higher number of properties are removed from the list of materials subject to a less stringent procedure. Fig. 1 introduces a visual representation that illustrates the materials space and the process of exploring it.

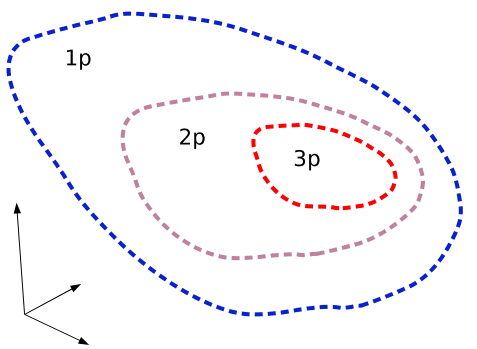
3. Comparative ranking

The third ranking procedure is then created as a visualization tool to collect all available materials in a single table, to rank them within a unique framework, and as a benchmark to compare the results of the previous two ranking scheme. For this procedure, the main issue is connected to the fact that materials with different available properties must produce a comparable ranking value. The win fraction concept might be re-used to define a ranking value for every available material, after applying some changes to the formulation presented in the previous section. Eq. (7) is intended to be applied to the set of properties that a material possesses, and the absence of certain features does not impact the final value of WF_i . If WF_i is used directly, materials with one single outperforming feature might rank at the top of the list, obscuring the rest of the candidates. On the other hand, if the win fraction is utilized for every material across the 10 retrieved properties, even in the presence of missing data, it becomes essential to specify how the missing values affect the win fraction. This depends on two factors: the weight assigned to each property and the value to be assigned to the missing ones. A unitary weight assigned to all the properties would reward materials with a lot of available data at the expense of others that have a smaller set of essential and high-performing features. A good compromise was found by subdividing the properties in three different categories (c), as proposed in Tab. II. Then, the weights are built by multiplying two coefficients:

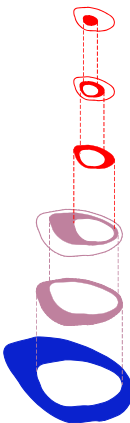
- The first term is a constant value that applies to all materials and is defined as $1/C$, where C is the number of categories. In this work, we always consider three categories, so the first term is equal to $1/3$.
- The second term is material-dependent and it is defined as $1/P_{i,z}$, where $P_{i,z}$ is the number of available properties of the z -th category of the i -th material.

In this way, materials lacking in the key categories - melting temperature + proxies, thermal conductivity, and heat capacity - are penalized, but the number of properties retrievable within a category does not affect the weight. Then, the weight of a given property is multiplied by the corresponding single-property win fraction $WF_{i,k}$, and the summation over the all features builds the weighted average win function $\overline{WF_i}$ as presented in the following equation:

MPDS material space (MS)



MS exploration via ranking criteria



PFM candidates

	total	selected
Thickness ranking: $d^{\text{ELMs}} > 0 \text{ mm}$	177	20
Thickness ranking: $d^{\text{SS}} \geq 3 \text{ mm}$	1	0
Pareto 3p: $I \leq 5, WF_i \geq 50\%$	39	6
Thickness ranking: $d^{\text{SS}} \geq 3 \text{ mm}$	175	13
Pareto 2p: $I \leq 5, WF_i \geq 70\%$	628	6
Pareto 1p: $I \leq 100, WF_i \geq 90\%$	6036	26
	7056	71

FIG. 1. Schematic representation of the material space in MPDS and its exploration based on the number of available properties and the corresponding ranking procedure, allowing for the identification of promising candidates through the application of multiple ranking criteria.

$$\begin{aligned} \overline{WF_i} &= \sum_{z,k} w_{i,z} WF_{i,k} \\ &= \sum_{z=1}^3 \frac{1}{3} \sum_{k=1}^{P_{i,z}} \frac{1}{P_{i,z}} WF_{i,k} \end{aligned} \quad (8)$$

where k represent the k -th property of the z -th category of the i -th material. If a category is not present for a given material, fictitious $WF_{i,k} = 0$ and $P_{i,z} = 1$ are assigned. This methodology can be generalized for any number of categories and any of their subsets. For instance, the melting temperature and proxies category might be split between actual T_m and proxies, generating a subset with two sub-categories. The results remain very similar whether or not this additional subcategory is included. Therefore, for the sake of simplicity, this approach is not discussed further.

B. Plasma-wall interactions

The interactions between hydrogen isotopes, alpha particles and the PFM have a complex dynamics, which requires large-scale (10^5 - 10^6 atoms) and long-timescale (10^2 - 10^3 ns) molecular dynamics (MD) simulations [43, 44]. For instance, the entire formation process of a W fuzz layer under plasma bombardment is out of the timescale explorable even with classical MD [45]. With the goal of finding indicators that reflect some of the undesired phenomena PFM may experience when interacting with a plasma particle flow, while being computationally efficient, we use two key defects, as proxies, surface

binding energies (SBE) and hydrogen interstitial formation energies (H-IFE), whose formation energies can be calculated within the DFT framework.

1. Surface binding energies

As mentioned above, the minimum thickness of a PFM is highly constrained by the rate of erosion of the materials surface under the plasma impingement, which in turn is measured through the sputtering flux of the surface atoms. For physical sputtering, the energy distribution of the sputtered particle flux, $\Phi(E_e)$, can be described within the binary collision approximation (BCA) by the Thompson energy spectrum [46]. The Thompson energy spectrum highlights an important proportionality between $\Phi(E_e)$ and the surface binding energy (SBE or E_{sb}) of a material:

$$\Phi(E_e) \propto \frac{E_e}{(E_e + E_{sb})^3} \quad (9)$$

This relation has a distribution that peaks at $E_e = E_{sb}/2$, where E_e is energy of the sputtered (emitted) particles leaving the surface. It is notable that the tail of the Thompson energy spectrum deviates from experimental values when the projectiles bombarding the surface have low-energy (< 500 eV) and it is corrected by the Falcone energy spectrum [47]. In both cases, SBEs highly affect the sputtered particle flux, therefore the erosion rate and the minimum thickness required from a given PFM. The SBE is defined as the energy that is necessary to remove an atom from the top surface layer (in

vacuum) during the physical sputtering process. We calculate SBEs from first principles, and we use these as a proxy of the material's resistance to physical sputtering. SBEs are often estimated using elemental enthalpies of sublimation in sputtering calculations. However, recent literature emphasizes that first-principles SBEs are essential to achieve more accurate outcomes [48–50]. In the context of density-functional theory (DFT), these are calculated through the following relation:

$$E_{sb} = E_a + E_{s+v} - E_s \quad (10)$$

where E_a is the DFT total energy of the single isolated (sputtered) atom a , E_s is the total energy of the crystal slab with a perfect surface, and E_{s+v} is the energy of the unrelaxed (for efficiency) slab with one surface vacancy at the position that was atom a . E_{sb} is obtained by developing the Surface Binding Energy (SBE) workflow, a semi-automated Python script created to make standardized SBE calculations (in-house, forthcoming). Once the candidate is selected and its crystal structure is defined, 6 main steps follow:

1. Relaxation of atomic positions and cell shape of the primitive crystal structure as obtained by MPDS, and calculation of its total energy.
2. From the relaxed lattice constants, all the inequivalent slabs that can be generated with Miller indices hkl up to 1 are created and relaxed and their surface energy is obtained through the following relation:

$$E_{surf}^{hkl,\alpha} = \frac{E_s^{hkl,\alpha} - \frac{N_s^{hkl,\alpha}}{N_b} E_b}{2A_s^{hkl}} \quad (11)$$

where E , N , A are the total energy, the number of atoms, and the area of the crystal slab, s and b are the subscripts indicating slab and bulk structures, and hkl and α indicate the Miller index and the termination of a specific facet of the crystal structure. A minimum distance of 10 Å of vacuum between repeated slabs is imposed as discussed in Refs. [51, 52].

3. The slab with the lowest $E_{surf}^{hkl,\alpha}$ is selected together with all possible terminations of the same Miller index, supercells are created and their total energy (E_s) is obtained. A minimum distance of 9 Å between periodic images is imposed to reduce vacancy-vacancy interaction.
4. One atom is removed from the surface of each supercell (per species and inequivalent positions) and the total energy (E_{s+v}) is calculated. One atom is considered a surface atom if it lies within 1 Å from one of the two surfaces. Atomic relaxation is neglected within this approximation.

5. The total energy of a single atom (E_a) in a cubic cell of side $\sqrt[3]{4000}$ Å is calculated for each element of the crystal.
6. E_{sb} is calculated following Eq. (10); if inequivalent sites of the same chemical element are found on the surface of given terminations α and/or multiple termination α are available, E_{sb} is calculated for each element as the arithmetic mean between all inequivalent sites of each termination.

All DFT simulations are performed by using the open-source computer code for electronic-structure calculations Quantum ESPRESSO (QE) [53, 54] and all parameters required to run the calculation are retrieved by Quantum Espresso Input Generator website [55–57] set for spin-unpolarized calculations, with maximum k-points distance of 0.2 Å⁻¹, a smearing width for metals of 0.2 eV and using the pseudopotentials library SSSP Efficiency PBEsol (version 1.2.0), where exchange and correlation effects are approximated using the Perdew-Burke-Ernzerhof revised for solids (PBEsol) functional. The kinetic energy cutoff for both charge density and wavefunctions is consistent across all calculations for a specific crystal and is set as the highest value suggested by the Quantum Espresso Input Generator among the elements present in the crystal.

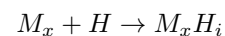
Once E_{sb} is known, the energy that a projectile must possess to sputter one atom from a perfect-crystal surface in a head-on elastic collision has to be greater or equal to the kinetic energy transferred to the recoil atom E_T :

$$E_p \geq E_T = E_{sb} \frac{(m_p + m_a)^2}{4m_p m_a} \quad (12)$$

where in the case of equality E_p is the minimum energy that the projectile (a plasma atom) of mass m_p must possess to produce physical sputtering on a target surface atom of mass m_a that is bonded to the surface with energy E_{sb} .

2. Formation energy for interstitial hydrogen and its isotopes

A similar design is used to provide an estimate of the interaction between a hydrogen isotope (hydrogen, deuterium or tritium), denoted as H for the sake of simplicity, and the host crystal structure (M). The solubility of hydrogen isotopes in a perfect crystal structure besides its porosity, is of particular relevance inside the reactor to estimate hazardous tritium retention. The formation energy of an interstitial hydrogen isotope $\Delta E^f(H_i)$ in a perfect crystal at 0 K can be calculated as follows:



and

$$\begin{aligned}\Delta E^f(H_i) &= E^{DFT}(M_x H_i) + E^{ZP}(M_x H_i) \\ &\quad - E^{DFT}(M_x) - E^{ZP}(M_x) \\ &\quad - E^{DFT}(H) - E^{ZP}(H)\end{aligned}\quad (13)$$

where E^{DFT} is the ground-state total energy calculated with a DFT code, E^{ZP} is the zero-point energy (ZPE). This expression can be approximated by considering $E^{ZP}(M_x H_i) \approx E^{ZP}(M_x) + E^{ZP}(H_i)$. Therefore, Eq. (13) can be re-written as reported in Ref. [58]:

$$\begin{aligned}\Delta E^f(H_i) &\approx E^{DFT}(M_x H_i) + E^{ZP}(H_i) \\ &\quad - E^{DFT}(M_x) - E^{DFT}(H) - E^{ZP}(H)\end{aligned}\quad (14)$$

As demonstrated in Refs. [59–61], the solubility of a gas within a crystal under low pressure conditions (< 100 atm) can be derived for a system in thermodynamic equilibrium between an ideal gas and the bulk of the perfect crystal. It is expressed as a function $\Delta E^f(H_i)$, along with additional entropic corrections (s_{corr}). Specifically:

$$\begin{aligned}\frac{N_{H_i}}{N_i} &\approx \exp - \left(\frac{\Delta E^f(H_i) - s_{corr}}{K_b T} \right) \\ s_{corr} &= T s^{vib}(H_i) + \Delta \mu(H)(T, p_0) + K_b T \ln \frac{p_H}{p_0}\end{aligned}\quad (15)$$

where N_{H_i} and N_i are the number H atoms and interstitial sites respectively, $T s^{vib}(H_i)$ is the vibrational entropy of a single H atom in an interstitial site, $\Delta \mu(H)(T, p_0)$ and the last factor account for the entropic contribution of H at temperature T and pressure p_H . Eq. (15) is derived by the separating vibrational and conformational entropy of the crystal with an interstitial hydrogen isotope ($W H_i$), as the sum of the entropies of the perfect crystal (W) and the hydrogen interstitial (H_i), while assuming $N_i \gg N_{H_i}$. To maintain computational affordability for screening purposes, we calculate $\Delta E^f(H_i)$ neglecting zero-point energy (ZPE) and entropic contributions, as outlined in Eq. (16). Consequently, under this formulation, the computed interstitial formation energy remains equivalent for any hydrogen isotope. However, it is worth noting that within the context of PFM, a more accurate approach would require to redefine the hydrogen reservoir as the hydrogen stored in the crystal surface at equilibrium, resulting from the impingement of high-energy plasma particles.

A second semi-automatized Python workflow, called the Hydrogen Interstitial Formation Energy (H-IFE) workflow, is built to calculate $\Delta E^f(H_i)$. The main challenge of this calculation lies on the identification of the interstitial hydrogen (H) sites with the lowest formation energy. Below, are the steps used to accomplish this task:

1. A supercell of the primitive crystal structure of a given material is created with a minimum size of $9 \times 9 \times 9$ Å³. The supercell is relaxed and its $E^{DFT}(M_x)$ is calculated.

2. N supercells of the same size of step 1 but containing one interstitial H atom are generated. The interstitial sites are randomly chosen from within the primitive cell of the supercell, with the only constraint being that the interstitial site of the $n+1$ supercell is at a minimum distance of 1 Å from all crystal atoms and the interstitial sites of all previous supercell. The number of interstitial sites, N , is determined based on the size of the primitive cell, and the random search for interstitial sites is terminated if more than 5,000 attempts are required. This approach ensures that the primitive cell of each crystal structure is uniformly explored in terms of interstitial site density. The interstitial supercell are then relaxed and their total energy is calculated.

3. $\Delta E^f(H_i)$ is calculated from the total energy of the interstitial supercell with lowest $E^{DFT}(M_x H_i)$, using the following equation:

$$\begin{aligned}\Delta E^f(H_i) &= E^{DFT}(M_x H_i) \\ &\quad - E^{DFT}(M_x) - E^{DFT}(H)\end{aligned}\quad (16)$$

The same DFT code and set up of the input parameters used for the SBE workflow are used for the H-IFE. For comparison with literature reference $\Delta E^f(H_i)$ is also computed for a hydrogen molecule (H_2) reservoir ($\frac{1}{2} E^{DFT}(H_2)$).

III. RANKING RESULTS

The MPDS database contains more than 500,000 crystal structures. When only the materials possessing at least one out of the ten properties previously selected are retained and radioactive and high pressure crystals are discarded, the total number of available candidates is reduced to 7,056.

The d^{ELMs} thickness ranking procedure is applied to the 177 crystal structures having the required properties. These materials are ranked as a function of their maximum allowable thickness to avoid melting during type-I ELMs, and it is found that only 20 materials meet the set prerequisites. Out of the 6879 remaining materials, 176 had the properties to be ranked on d^{SS} . Of these, 13 candidates are retained due to their ability to withstand steady-state conditions without melting. The remaining available structures are, instead, classified using the Pareto front procedure. From the latter, we identify 38 best-performing candidates, bringing the total number of selected materials from MPDS to 71. Fig. 1 illustrates a schematic representation of the material space in MPDS and its exploration, taking into account the number of available properties and the corresponding ranking procedure. All 7,056 candidates are then ranked according to the comparative ranking scheme, to show consistency across different ranking procedures and identify

any candidates that exhibit discrepancies among the various rankings.

We then assess the potential of the top candidates thanks to the analysis of literature on divertor materials. This serves as an additional benchmark to validate our findings and identify the materials that have already been explored and the corresponding advantages and disadvantages of their application. New d^{SS} and d^{ELMs} values are calculated for the most promising PFM candidates identified through the literature review. These calculations are based on the literature values of the properties required from heat balance equation (Eq. 4). Then, SBE and H-IFE workflows are applied to highlight possible drawbacks of the selected structures. Ultimately, a comprehensive ranking is provided to identify the most promising PFMs. Fig. 2 depicts the flowchart encompassing the entire process, beginning from the retrieval of MPDS data to the generation of a list comprising the top candidates for PFM. It should be noted that the chemical formulas of the materials presented in the tables and figures of this chapter correspond exactly to those documented in the MPDS database.

A. Thickness ranking during ELMs

In Fig. 3 and Tab. VIII in the Appendix, we present 20 PFM candidates able to sustain the divertor conditions during type-I ELMs without melting and satisfying Eq. (5). These selected materials can be summarized into 3 main categories.

1. Carbon-based materials: diamond (C dia).
2. Pure transition metals: W, Mo, Ir, Cu, Os, Ru, Rh, Re, Ta, Cr.
3. Ceramics: (carbides) TaC, HfC; (nitrides) AlN, GaN, TiN; (borides) HfB₂, TiB₂, ZrB₂.

This list includes the most extensively studied PFMs proposed as divertor materials in numerous experimental projects. In addition, other materials, such as TiB₂ and TiN, which have been employed as PFMs in tokamak limiters [9] subject to comparable thermal loads as divertor materials, appear in the selection.

It might result surprising that a few of the most well-known PFMs are not included in this initial selection. For example, a few complex alloys, such as stainless steel and Inconel [9], that have been utilized in past as PFMs do not appear just because they are not included in the MPDS database. However, these alloys do not withstand the high heat loads present in the divertor region. On the other hand, while Ti and Be are listed in the MPDS, not all the required properties are available to calculate d^{ELMs} . However, Be exhibits a thermal conductivity that falls just short of satisfying divertor conditions [62], while the thermal conductivity of pure Ti is significantly inadequate for the intended purpose [63]. Another group of materials previously employed as PFMs but excluded

through thickness ranking are TiC, pure B, Al, and boron carbide (B₄C) [9], as they are designed to withstand lower temperature regimes. Graphite and SiC-3C are excluded due to the underestimate of their actual thermal property values in the MPDS database.

B. Thickness ranking in steady-state conditions

Once the materials ranked with d^{SS} are excluded, we identify 13 materials with $d^{SS} \geq 3$ mm; these are reported in Fig. 4 (and Tab. IX). A comparison of their characteristics with those of the d^{ELMs} ranking candidates reveals that most of these materials rank at the bottom of the list in terms of performance, and they could potentially be excluded altogether unless unreasonably high heat capacities are considered. Additional literature investigations substantiate this hypothesis, except for three materials, W₂C and BN, which possess adequate melting temperatures, and VB₂, which exhibits sufficiently high thermal conductivity, warranting further scrutiny.

C. Pareto ranking

Pareto ranking is performed with materials whose properties cannot be assessed by the two thickness rankings. Of the 6,703 crystal structures analyzed, 6 are in the 3p category (Tab. X), 6 in the 2p category (Tab. XI), and 26 in the 1p category, including 5 polymorphs of BC₂N and C₃N₄ which are excluded from further analysis because they exhibit highly similar thermal properties (see Table XII). We increase the portfolio of properties for the selected materials with values found in the literature. Comparing these properties with those of materials selected through d^{ELMs} and d^{SS} rankings, we find that the number of remaining candidates qualifying as PFM is reduced to the following:

1. Metal alloys: Ta_{0.5}W_{0.5}.
2. Ceramics: BC₂N, C₃N₄, HfN, SiC-2H, Ta₂C, TaN, VC, VN, WC, W₂C.
3. Carbon-based materials: graphite intercalated with CoCl₂, FeCl₃, SbCl₅.
4. Boron-based materials: Mg₂B₂₅C₄, YB₆₆.
5. Perovskite nitrides: TiFe₃N, VFe₃N.

Among these materials, it is worth noting that the x-Fe₃N perovskite nitrides (TiFe₃N and VFe₃N) exhibit a high value for the isothermal bulk modulus. However, the literature lacks a comprehensive analysis of their thermo-mechanical properties, which is crucial for determining their applicability as PFMs. For these reasons, they are not further considered as potential PFM candidates.

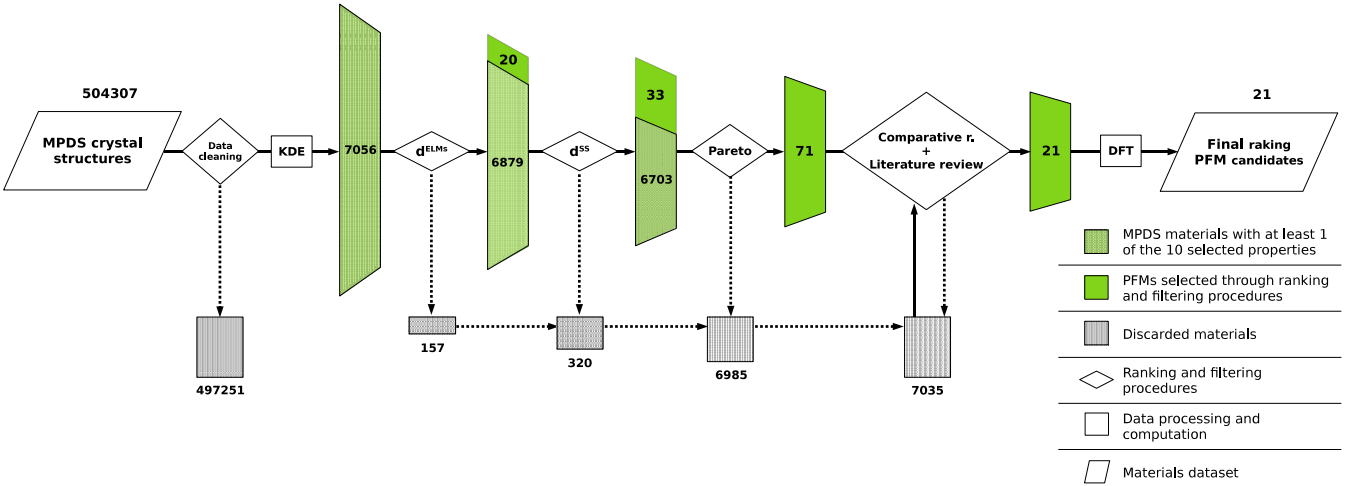


FIG. 2. Flowchart illustrating the PFM selection process, which involves all the steps described in Section II and the literature review. It starts from the MPDS materials and narrows down to a set of selected PFM candidates. The material selection is visually represented using a funnel chart.

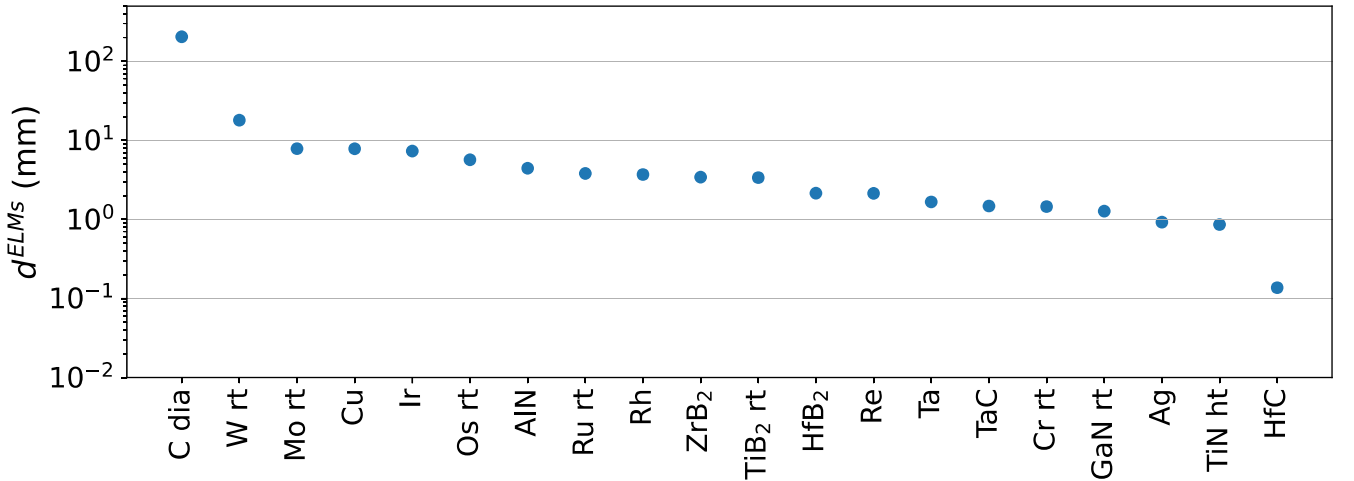


FIG. 3. d_{ELMs} logarithmic scale for the 20 selected PFM candidates extracted from MPDS. d_{ELMs} defines the maximum thickness for a material to withstand type-I ELMs without melting. Only materials with $d_{ELMs} > 0$ mm are selected.

D. Comparative ranking

The comparative ranking procedure is used as benchmark for the previous ranking processes. From the weighted average win-fraction definition (\overline{WF}_i), materials belonging to the subsets 3p, 2p, and 1p naturally separate, with their scores limited to 100%, 66.7%, and 33.3% respectively. The results of the comparative ranking procedure are presented in Fig. 5, illustrating the materials belonging to category 3p ranked from the 1st to the 100th position. Additionally, the Appendix includes materials from the 101st to the 200th position of category 3p, together with the top 200 materials from category 2p and 1p (Fig. 6 - 10). \overline{WF}_i is compared with the result coming from the thickness and Pareto ranking procedures. For the latter, a binary value is assigned to every material

in order to show its positive or negative detection by the ranking process. In order to emphasize the comparison between different ranking procedures, each of these is applied to the entire set of available materials, regardless of whether they are excluded by more stringent rankings.

The first 63 materials (out of 218) outperforming the 3p \overline{WF}_i ranking scale (Fig. 5) contain the whole set of the PFM candidates able to sustain divertor ELMs conditions, as indicated by the heat balance equation. Of the top 15 materials, 12 of them are selected by the d_{ELMs} ranking. All of these candidates are also selected by the d_{SS} ranking and one or more Pareto rankings, indicating an excellent consistency between the three ranking procedures. The importance of a comparative scheme is further emphasized by its ability to avoid false negatives in screening studies of this nature. Inconsistencies

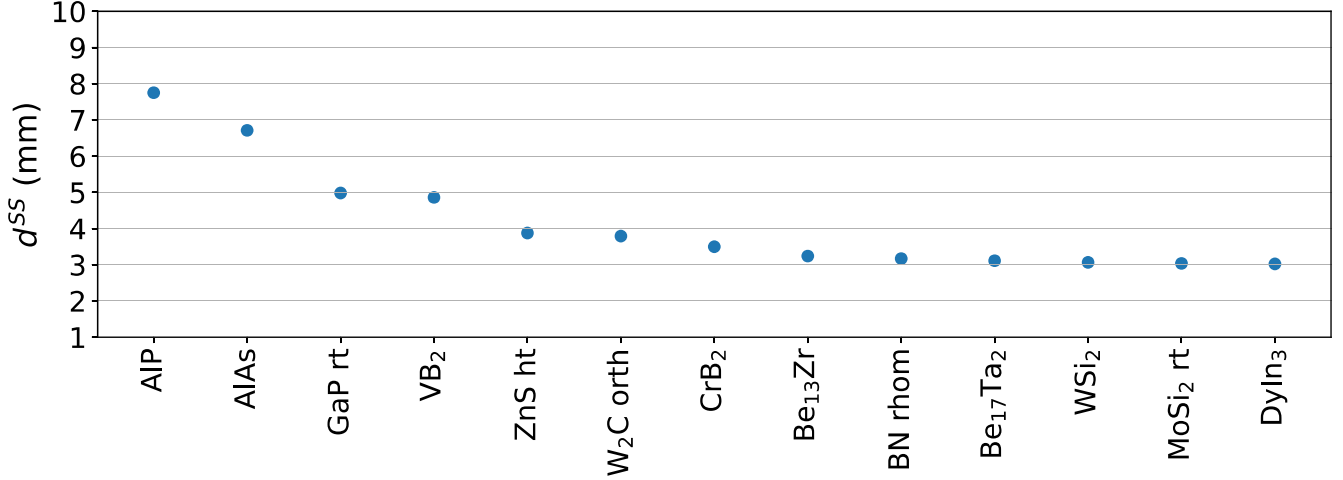


FIG. 4. d^{SS} defines the maximum thickness for a material to withstand steady-state condition without melting. The 13 materials showing $d^{SS} \geq 3$ mm are selected from MPDS once materials ranked through d^{ELMs} criteria are excluded.

among different selection criteria can bring to light previously dismissed candidates. Indeed, the two materials erroneously discarded according to the d^{ELMs} ranking (as indicated in Sec. III A), graphite and SiC-3C, are well-captured by the whole set of Pareto rankings when included. Consistently, other known refractory materials exhibiting excellent thermal properties are selected by lower level ranking procedures when included: TiC, pure B, BeO, ZrC, B₄C (as B₁₃C₂), and Li₂TiO₃. In particular, the latter material has been proposed as a tritium breeding material for the test blanket module of ITER [64]. Furthermore, another class of materials recently proposed as W-alternative plasma-facing materials is identified by examining the top 50 materials ranked by the 3p WF_i and in Fig. 5; this is the class of MAX phase materials, represented by Ti₃SiC₂ [65, 66]. Despite being these materials, and especially Ti₃SiC₂, refractory and possessing a good thermal conductivity, their decomposition temperature severely limits their suitability as divertor PFM's [67]. In the 2p and 1p WF_i ranking scales, which consist of 803 and 6,063 materials respectively, the top 200 candidates include the complete set of d^{SS} and 2p Pareto top candidates from the 2p set, and 20 out of 26 1p Pareto candidates from the 1p set. The clustering of the previously selected candidates near the top of the comparative ranking provides additional evidence of the reliability of the ranking procedure we have established.

IV. LITERATURE REVIEW OF THE PFM CANDIDATES

We analyse the four main macro-categories of materials, identified using the previous ranking criteria, based on previous literature results:

1. carbon-based materials;

2. boron-based materials;
3. transition-metal-based materials;
4. ceramics, which further divide into three main classes: borides, carbides, and nitrides.

Among the most promising materials, we select specific prototypical crystal structures as the foundation for calculating the formation energy of two commonly observed defects, the surface binding energy and the hydrogen interstitial formation energy, as described in Sec. V.

A. Carbon-based materials

The ranking procedure highlights two distinct allotropes of pure carbon: diamond and various types of intercalated graphite. Surprisingly, pure graphite is discarded by the d^{ELMs} ranking because of its low assigned KDE thermal conductivity value (see Fig. 6). In fact, the majority of the thermal conductivity values found in the MPDS database for graphite pertain to the direction perpendicular to its hexagonal plane. However, in the case of polycrystalline samples, such as those used for this applications, the primary contribution to thermal conductivity arises from heat transport parallel to the basal plane [68], which is thousands of times higher than the perpendicular one [63, 69]. The resultant thermal conductivity of these samples, accounting for the limiting factors inherent to the polycrystalline averages, remains of the order of hundreds of $\text{W m}^{-1} \text{K}^{-1}$ [68], considerably higher than the value extrapolated from the database (5.7 $\text{W m}^{-1} \text{K}^{-1}$) and sufficient to avoid melting during type-I ELMs. Consequently, graphite can be considered as a PFM candidate according to the d^{ELMs} ranking.

Graphite and carbon fiber composites (CFCs) were identified as the primary choices for (PFMs) for the ITER

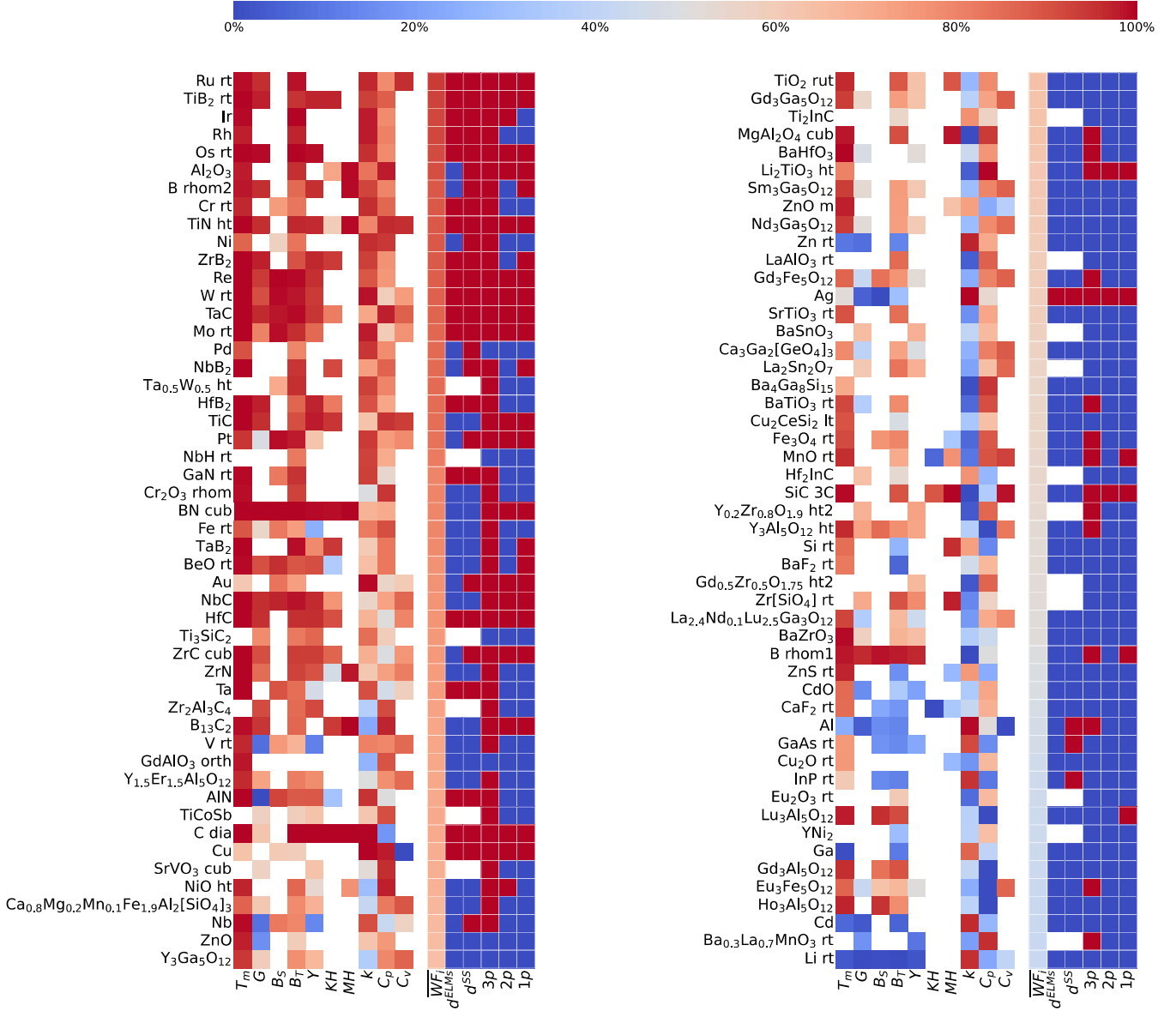


FIG. 5. Heatmap representation of the materials ranked from 1 (top left) to 100 (bottom right) according to the comparative ranking procedure. The materials are classified into the $3p$ subset and arranged in order based on their weighted average win-fraction (\overline{WF}_i) scores, with a maximum potential score of 100%. The figure also includes the individual win-fraction ($WF_{i,k}$) values for each property of the materials.

divertor [70]. Due to their remarkable thermal conductivity and high sublimation temperature [71], these materials have demonstrated the ability to withstand significant thermal loads with no structural damage or, at most, minimal degradation of the polyacrylonitrile fibers in the case of CFCs [72]. Furthermore, graphite-based materials pose low concerns regarding plasma core contamination due to their low-Z number, which minimizes radiative energy losses and allows for higher tolerance levels within the plasma. For this reason, fusion experiments worldwide continue to adopt graphite as the preferred PFM [7]. However, a material composed of low-Z elements is subject to surface erosion by physical sput-

tering processes, with the additional drawback of an enhanced chemical sputtering for graphite, due to the high reactivity between carbon atoms and the hydrogen isotopes contained in the plasma [73]. This leads to the formation of co-deposited layers of tritium-containing hydrocarbon on all in-vessel components, which increases the inventory of tritium [74]. In addition, the high thermal conductivity of graphite deteriorates rapidly under the influence of energetic neutrons [75, 76], an effect only partially mitigated by defects recombination that occurs at high-temperature.

Graphite-based materials have been tested for many years [77] and, even recently, carbon-based candidates

such as diamond or diamond-like carbon structures are re-considered and proposed as alternatives to W [78, 79]. However, effective suppression of the surface sputtering process, has not been demonstrated. Despite many attempts on suppressing chemical sputtering [80–82] and radiation enhanced sublimation [83], physical sputtering process plays a crucial role per se. Based on the literature data from the early 2000s [9, 40], one can see that even when considering only physical sputtering, the tritium co-deposition rate constant in graphite drops to approximately one-fifth of its original value. This reduction is inadequate to offset the tritium inventory limit that exceeds the threshold by two orders of magnitude [74, 84]. For carbon to be the main constituent of a candidate material, this constraint cannot be circumvented unless: (i) significantly higher SBE values are assumed for the surface carbon atoms of the candidate material, (ii) a different preferential target element is considered for the sputtering process (e.g. low-Z carbides), (iii) the kinetic energy of plasma particles is reduced below the threshold value of carbon sputtering, (iv) new tritium desorption techniques are proposed.

Carbon-based materials are, therefore, not considered optimal as divertor PFM in ITER-like devices. However, due to their impressive ability to withstand high thermal loads and their well-documented characterization in the literature, they are included as reference materials in the list of top PFM candidates. In particular, carbon diamond (C dia) and graphite (C gra) are chosen as representatives of the carbon-based materials category for the purpose of calculating defect formation energies.

B. Boron-based materials

The boron-based materials reported in this study belong to the family of compounds known as icosahedron-based borides. These materials consist of a main structure of B_{12} icosahedra, which may be interconnected through chains of carbon (or other nonmetallic) atoms. The voids within this framework can also accommodate metal atoms. Boron-based materials are selected through the 1p Pareto ranking procedure, due to their outstanding Knoop hardness, and fall into two classes. The first class includes RB_{66} , with R being a metallic atom. RB_{66} materials combine the physical and chemical properties of refractory crystals with the typical electrical, optical, and thermal properties of amorphous semiconductors. Despite their interesting stability under high temperature and abrasive conditions, they possess a really low thermal conductivity value because of their complex crystal structure [85, 86]. An example of the second class is $Mg_2B_{25}C_4$, where, beside the presence of metal in the boron structure, carbon acts as a bonding element between the various icosahedral B_{12} structures. The materials of this class have similar thermo-mechanical properties to the RB_{66} crystal class [87]. Boron carbide B_4C has one of the highest thermal conductivity within the second

class, reaching a value of approximately $28 \text{ W K}^{-1} \text{ m}^{-1}$ at room temperature. Under neutron irradiation, this value is significantly reduced [88], but it can be largely restored through high-temperature annealing, especially in the case of ^{11}B enriched samples [89]. However, this value of thermal conductivity is insufficient to avoid melting during ELM event, as confirmed by d^{ELMs} ranking procedure correctly discarding of this material from the list of potential candidates. It is worth noting that B_4C is identified by a compositional variation of boron carbide, $B_{13}\text{C}_2$, in MPDS. Due to its limited thermal conductivity, this class of materials is deemed unattractive for withstanding high heat loads and frequent thermal shocks and, therefore, it is not included in the list of top PFM candidates. It is worth noting that in combination with a highly conductive substrate, such as graphite, B_4C has been proposed as protective layer of the main divertor armor material [90].

We finally remark that the presence of ^{10}B (approximately 20% of natural elemental boron) poses significant limitations on the use of boron-based PFM. In fact, ^{10}B is known to undergo transmutation through the (n, α) reaction, resulting in the production of helium and lithium atoms and the formation of cavities or bubbles in the matrix and grain boundaries [91, 92]. This process leads to void-swelling, high-temperature helium embrittlement, and compromises the structural integrity of the crystal due to progressive loss of ^{10}B . The negative effects of ^{10}B transmutation can be mitigated by using isotopically enriched ^{11}B , which has a considerably lower transmutation cross-section to thermal neutrons [92, 93].

C. Transition metal-based materials

a. Tungsten The future and current generations of PFM candidates for the divertor region are W-based. Despite the fact that W outperforms all other alternatives tested so far, many downsides in its application remain, and are reported in literature. W can sustain the divertor thermal loads in a very narrow temperature window compared to the operating temperature interval of the PFM surface. In steady-state conditions the surface of the metal is close to its ductile–brittle transition temperature (DBTT), 200 to 600 °C, depending on the manufacturing processes, and below the DBTT the reduced thermal stress resistance leads to intense crack networks [94]. While W does not encounter any surface changes at heat loads of 10 MW m^{-2} , even during typical slow-transient of 20 MW m^{-2} , it shows severe surface damage and deep crack formations [95]. In addition, when the low recrystallization temperature of W (roughly 1,300 °C) is surpassed, grains growth and consequent increase of DBTT, brittleness and surface roughening, and decrease of thermal shock resistance and mechanical strength are observed [96, 97]. Finally, power pulses produced during ELMs can result into cracking of the surface, partial melting of the tiles edges, and depletion of the PFM sur-

face [94]; in particular, alarming levels of W erosion are reached when ELMs are combined with slow-transient loads [98, 99].

The heat load is associated with a flux of plasma particles and their implantation in the W armor, for a distance of a few nanometers [100]. The energy of the plasma particles (approximately 10 eV) is not sufficient to physically sputter the surface atoms of the W armor, as it is much lower than the W sputtering threshold energy (209 eV for D, 102 eV for He, at 20 °C [101]). Furthermore, the weak chemical reactivity between W bulk, hydrogen isotopes and He atoms does not lead to any additional chemical sputtering [102, 103]. Nevertheless, the erosion of the W surface is a reason of concern due the surface morphology changes produced by the interaction between He atoms and W crystal defects in the presence of hydrogen, which leads to the formation of helium bubbles and the so-called a fuzz layer, a process that is not yet completely understood [104]. Despite the well-known decrease of the effective thermal conductivity of the nano-fiber layer and consequent ejection of melted droplets [29], the effects on the net material erosion rate is still under debate [103, 105, 106]. Plasma particles can be retained by the PFM, which is problematic as mentioned above for CFCs. ELMs and fuzz formations seem to play an opposite role in terms of tritium retention in the W wall: the damaged surface produced by ELMs enhances its retention compared to steady-state conditions [107]; in contrast, the open porosity of the fuzz layer serves as an additional release channel for the hydrogen isotopes [100]. However, in the presence of He defects in W can affect its retention capacity; dislocation loops punched by helium bubbles are responsible for tritium trapping sites [108] and the total retention amount can increase drastically.

In this scenario, high-energy neutrons also play a role and irradiated-W samples showed more than double tritium retention compared with undamaged W [109]. Vacancy clusters of the neutron-damaged materials can act as additional traps for hydrogen isotopes [110]. 14.1 MeV neutrons are also responsible for the degradation of the wall armor under operational conditions via reduction of the thermal conductivity and embrittlement, due to defect accumulation and transmutation. For both properties, the worsening of performance dictated by the contribution of dislocations and voids is in large part recovered at higher temperature, thanks to the annihilation of the irradiation-induced defects [111, 112]. W transmutations leads to the production of rhenium (Re) and osmium (Os) in different percentages as a function of the neutron's flux [113]. In ITER, divertor replacement is planned after a displacement per atom (dpa) of 0.7 with 0.15% of Re content and less than half of that for Os content [114]; in DEMO this could be up to 20 times higher [115]. Thermal diffusivity is negatively affected by the presence of Re in the W bulk (around -25% of unirradiated W at 1,000 K) and temperature changes seem to be negligible at the relevant concentration [116, 117]. In

terms of ductility (and recrystallization temperature) Re addition to W is beneficial [29], but in presence of Os and dpa above 0.6-1 their concentration is enough to produce an intermetallic second phase precipitate, which leads towards strong hardening and embrittlement of the PFM, regardless of temperature variations [111]. Transmutation products dominate over the neutron-induced defects for the strengthening effect as long the irradiation dose is higher than 0.6 dpa, while the opposite is true below 0.3 dpa.

To summarize the aforementioned points, W is presently considered the most viable option to withstand the expected heat loads at the divertor of a tokamak reactor, securing its position among the most promising PFM candidates. However, its performance under extreme thermal stress conditions and its long-term structural integrity when exposed to the combined effects of plasma and neutrons remain unresolved issues and crucial areas of ongoing research in the field.

b. Molybdenum The most studied high-Z divertor PFM alternative to W is molybdenum (Mo). Mo was used as divertor PFM in the Alcator C-Mod tokamak reactor and its behavior extensively analyzed [118]. While Mo has a melting temperature and thermal conductivity lower than W, it shows some advantages when compared with W, such as a lower transmutation rate and therefore reduced formation of precipitates [113], and slightly lower H retention [119]. In addition, as in the case of W, Mo thermal conductivity is barely affected by high temperatures [120] and it can be restored to its high values thanks to annihilation of defects on neutron-irradiated samples [121]. However, neutron irradiation poses a clear drawback on the application of Mo as plasma-facing material. Both the US and UK waste disposal rating classify a Mo armor exposed to divertor neutron irradiation conditions as high-level-waste [26, 34, 35]. Despite this, plasma-Mo interactions under divertor conditions are still under investigation, and shows many similarities with plasma-W interaction. The erosion in steady-state conditions is mainly due to impurities in the plasma that have mass sufficiently large to sputter Mo (i.e. Mo itself and oxygen). Even if this erosion is predicted to be slightly higher than the case of W, it remains tolerable (1.5 mm/burn-year) [26]. As in the case of W, the interaction with He ions results in the creation of fuzz nanostructures on the surface exposed to the plasma [122]. The temperature window for their formation is narrower and lower than for the case of W [123], but it seems to follow the same pattern [122]. Also, under unmitigated type-I ELMs-like pulses the difference in erosion between the two metal with a pristine surface has not been fully elucidated yet. A recent study reported that the volume of Mo ablated from the surface by a single laser pulse is 10 times larger than W [124], whereas another study reports that after 100 laser pulses (of similar energy) the two materials do not show appreciable difference in the amount of mass loss [125]. In both experiments the energy required from the laser pulse for melting the two metals was found to be

above the energy of mitigated type-I ELMs, 1.0 MJ m^{-2} for Mo and 1.4 MJ m^{-2} for W [125]. Similar effects are produced by pulsed lasers, simulating unmitigated ELMs on fuzz form Mo surfaces [126]. When covered with a fuzz layer, the mass loss appears to be a linear function of the laser pulse, instead of exponential as for the pristine surface [125]. Under mitigated type-I ELMs, the fuzz layer gradually disappears, without any melting, with a mass loss that increases as a function of the surface temperature [103]. The extent to which this phenomenon, when combined with arcing, could pose a risk of core plasma contamination remains unclear. Additionally, it should be noted that a higher concentration tolerance is predicted for Mo ($10^{-3}\text{--}10^{-4}$ [127, 128]) compared to W (5×10^{-5} [129]) before plasma quenching. Overall, Mo is still considered an attractive alternative to W and is therefore included in the list of top PFM candidates for further investigations.

c. Copper A high-strength copper alloy material is envisaged for the cooling tube system running through the central region of the W monoblock of the ITER divertor target. Divertors designed for DEMO envisage the use of pure copper (Cu) as stress-relieving interlayer between W and the Cu-alloy [130, 131]. In fact, despite its impressive thermal conductivity, Cu cannot be exposed directly to the plasma flux, primarily because of its low hardness and softening temperature [132] and the very intense erosion to which it is subject to under hydrogen plasma flux [133]. In addition, even if Cu and Cu alloys are known to maintain high thermal conductivities at elevated temperatures [134], the exposure to neutron radiation can damage their crystal structure and cause transmutations, which can negatively affect their thermal diffusivity [135, 136]. Furthermore, the induced radioactivity caused by the high-energy fusion neutrons raises concerns about safety and waste disposal considerations [34, 35]. Due to these reasons, pure Cu is not directly employed as PFMs in fusion tokamak devices and is not included in the list of promising PFMs. However, application of Cu in the form of alloy as a thermal conductor material that is not exposed to plasma has been extensively investigated, and it is important to mention that, in a small number of studies, copper-alloys are also proposed as primary divertor and first-wall materials, in particular W-Cu [133, 137] and Cu-Li [138–140].

d. Platinum-group and noble metals A set of transition metals, belonging to the so-called platinoids and noble metals classes, are reported here for their valuable thermal properties. We consider in descending order of performance (see Fig. 3): iridium (Ir), osmium (Os), ruthenium (Ru), rhodium (Rh), rhenium (Re), and silver (Ag). The main limit to their use as pure metals is dictated by their high price (they typically range in cost from \$1,000 to \$100,000 USD per kilogram) and scarcity [141] and their thermo-mechanical properties, typically slightly inferior than more affordable alternatives (W and Mo). The main application of these elements is thus as dopants or alloying elements. Re, be-

ing one of the cheapest of this list, second only to Ag, has been proposed as alloying element for W due to its enhanced thermo-mechanical performance: higher ductility, high-temperature strength, plasticity, and corrosion resistance, stabilization of the grain structure with increased recrystallization temperature and weldability, and reduced degree of recrystallization embrittlement [29]. However, the high cost and scarcity of Re is already affecting other industrial sectors (platinum–rhenium catalysts and high-temperature superalloy for jet engines) and strategies to reduce its application, finding alternatives and recycling processes are under investigation [142, 143]. Despite its cost-related limitations, Re is included in the list of leading PFM candidates as the most favorable alternative within this class of materials, in terms of cost and performance. The least expensive Ag is discarded due to inferior thermal properties when compared to the aforementioned transition metals, primarily dictated by a low melting temperature.

e. Early transition metals Together with the already discussed Mo, W, and Re, there are a few more elements from the first 5 groups of the transition-metal class that exhibit notable thermal capabilities, in particular Ta and Cr. Ta was suggested as a potential PFM in the past: however two significant drawbacks are present: (i) its inferior thermal properties when compared with W [144] (ii) the exothermic hydrogen absorption process, which yields larger tritium retention than other metals (such as W) with positive heat of solution for hydrogen [145]. In contrast, Ta demonstrates a higher energy threshold for the formation of a "fuzz" structure when exposed to divertor-like He ion flux, which suggests that surface thermal and mechanical properties may not degrade as quickly as for W in extreme fusion environments [146]. Chromium has been recently proposed as PFM for the DEMO-divertor structural body of the monoblock. Cr-10%W displays superior mechanical properties to Cr at low temperatures, where W is brittle, and higher strength compared with pure Cr. Further investigations of its behaviour under actual divertor conditions must thus be carried out [147]. For these reasons, both Ta and Cr are added to the list of promising PFM candidates.

f. Transition metal alloys Only one material stands out in this category, exhibiting features comparable to those of the positive thickness materials under type-I ELMs, this is the $\text{Ta}_{0.5}\text{W}_{0.5}$ solid solution, possessing high level thermal conductivity, heat capacity, and isothermal bulk modulus, with a melting temperature of 3,450 K is reported in the literature [148]. The two constituents of this alloy exhibit complete solubility [149], but given the low mass contrast between its components, the phonon contribution to its thermal conductivity is not significantly diminished, in contrast to many other alloy systems. Previous studies also investigate the thermo-mechanical properties of Ta-W composites, wherein Ta fibers are dispersed within a nanostructured W matrix to enhance fracture toughness [150]. However, the ability of these composites to withstand plasma ir-

radiation conditions remains a topic of ongoing debate [150–152]. Our screening process did not identify any other promising alloys; nevertheless, one of the most promising research areas in terms of alloys is represented by the high-entropy alloys (HEAs). These materials are currently not included in MPDS but, in a recent study [153], a W-Ta-based HEA alloy (38% W, 36% Ta, 15% Cr, 11% V) was able to show outstanding neutron radiation resistance properties, high hardness and small irradiation-induced hardening [153]. The material capacity to sustain high-dose neutron irradiation is attributed to the equal mobilities of vacancies and self-interstitials, which maximizes recombination and reduces defect concentration. This is likely due to the rough energy landscape induced by local lattice distortion and the disparity in chemistry. While lattice distortions can affect the thermal conductivity (a common drawback of this class of materials [154]), very recent promising results for thermal conductivity have been shown for the class of medium-entropy alloy [155]. As a prototype of this class, the ordered cubic structure (B2-superstructure [156]) of TaW is added to the list of top PFM candidates for which defect formation energies are then calculated using the DFT workflows developed here.

D. Ceramics

Most of the ceramics identified by the three ranking criteria can be classified as ultra-high temperature ceramics (UHTCs). This family includes a variety of materials, such as borides, carbides, and nitrides of early transition metals, and are characterized by their extremely high melting temperatures, typically above 3,000 °C, and/or their ability to withstand continuous use at temperatures exceeding 1,600 °C [157]. One of the major challenge for UHTCs in thermostructural applications is their poor resistance to thermal shocks. However, the manufacture of fibrous monolith ceramics limit the formation and propagation of cracks to the cell boundaries and can partially address this problem [158].

a. Borides Refractory diborides, such as the here HfB₂, TiB₂, and ZrB₂ reported here, exhibit an unusual combination of high strength, moduli, melting temperature, and thermal conductivity. The possibility of using diborides as PFMs is now again under discussion, since the production of isotopically separated ¹¹B diborides is now demonstrated [93, 159]. In fact, neutron irradiation of naturally occurring B is indicated as the primary causes of swelling and catastrophic cracking of borides, due to the helium and lithium accumulation deriving from the (n, α) reaction of ¹⁰B, as showed in Sec. IV B. Neutron-irradiation experiments on Ti¹¹B₂ demonstrated reduced swelling (especially at high temperature), suppressed macroscopic damage and moderate micro-cracking formation [93]. Concerning the thermal properties, ZrB₂ shows the capability to maintain a level of thermal conductivity at high temperature that

is comparable to W. Furthermore, since the electronic contributions mostly determine the total thermal conductivity value, neutron-induced defects are expected to have a minimal effect [159]. Both TiB₂ and ZrB₂ show encouraging results in terms of erosion resistance under high-energy He ions: the TiB₂ sputtering yield is reduced when compared with those of pure Ti [160, 161], while ZrB₂ show comparable erosion depth with that of W [159]. ZrB₂ also shows an interesting oxidation mechanism that might lead to oxygen absorption at higher temperatures [157–159]. However, experiments at divertor conditions are still lacking. While showing the same oxidation mechanism as ZrB₂, HfB₂ has raised some concerns regarding the production of 20 MeV gamma rays when irradiated with 14 MeV neutrons [162].

Inspired by the growing field of high-entropy alloys (HEAs) where five or more elements are mixed in similar proportions to form a new alloy, ZrB₂-based ceramics are also proposed as high- and medium-entropy ceramics (HECs) [163], and their thermo-mechanical properties are investigated [164]. (Zr_xTi_yNb_yTa_y)B₂ systems containing Zr, Ti, Nb, and Ta at the highest mixing entropy posses the highest hardness and moduli, but also the highest phonon scattering with the lowest thermal conductivity. Similarly, carbon-boron-titanium compounds with varying B/C/Ti ratios have been studied. It is observed that the highest thermal shock resistance is achieved for compositions where the constituents are mixed in similar proportions, which also exhibited lower thermal conductivity compared to pure borides and carbides [165]. ZrB₂ is also proposed as alloying ceramic to produce W-ZrB₂ alloys, with improved bending strength and hardness thanks to the strengthening of the originally fragile W grain boundaries [166]. An additional diboride, VB₂, is also of interest, according to the d^{ss} ranking, due to its remarkable values of high melting temperature and thermal conductivity. Considering the combination of these properties, with the noteworthy volumetric heat capacity reported in the literature [167, 168] (exceeding 5 J K⁻¹ cm⁻³ at high temperatures), VB₂ has been previously suggested as a protective layer to mitigate the ingress of hydrogen isotopes into structural materials in fusion devices [169, 170]. Consequently, the crystal structures of all the presented diborides, namely HfB₂, TiB₂, ZrB₂, and VB₂, are included in the compilation of the most favorable PFM candidates.

b. Carbides Carbides of the same transition metal have usually larger melting temperature and hardness than the corresponding borides and nitrides [171], at the price of a substantially reduced thermal conductivity when compared with borides [172]. Despite obvious concerns associated with high carbon content, linked the high level of tritium retention caused by carbon sputtering and co-deposition, carbides have mainly been investigated as PFMs for doping or alloying W. Three polymorphs of SiC are reported in MPDS, but only the hexagonal polytype, SiC-2H, is selected according to the Pareto ranking thanks to its excellent melting tempera-

ture, around 3,100 K. In fact, the cubic polytype SiC-3C is discarded by the thickness (ELMs) ranking, due to a reported very low thermal conductivity. This is quite surprising, since SiC-3C is known for its outstanding thermal conductivity (SiC-3C possesses the highest thermal conductivity value [173], along with a comparable melting temperature and slightly inferior mechanical properties [174] than the other polymorphs). Indeed, an erroneous value of thermal conductivity is reported in the MPDS database, $0.49 \text{ W m}^{-1} \text{ K}^{-1}$, instead of the correct value, $490 \text{ W m}^{-1} \text{ K}^{-1}$. Once this is accounted for, SiC-3C appears at the top of the d^{ELMs} ranking. SiC is largely investigated as refractory and plasma-facing material due to its excellent thermal properties and low activation under fusion or fission neutron bombardment [175]. It is also considered as divertor PFM [176], motivated by its favourable erosion properties when compared with graphite. In particular, SiC-3C has been used as a coating PFM of graphite tiles during the 2017-19 DIII-D run campaigns [176], and the extrapolation of results to a DEMO-type device shows a 70% decrease of the erosion yield of carbon is expected with SiC as PFMs at the divertor with respect to graphite. The reduced erosion was also confirmed in a later study [177]. This effect, combined with the low solubility and diffusivity of tritium in SiC, [178] associated with a lower predicted tritium inventory in the co-deposited layer when compared with graphite (2/3 of the carbon material) [179], could motivate further investigations of SiC as divertor PFM. However, the reduced erosion has been extrapolated from very low concentration of C atoms in the plasma. In addition, the value of thermal conductivity of $490 \text{ W m}^{-1} \text{ K}^{-1}$ is not realistic under operational conditions where high temperature and neutron bombardment occur. The high temperature reduces significantly the thermal conductivity of the most well-known SiC polytypes [180, 181]. In addition, the presence of neutron-induced defects in SiC results in detrimental swelling and a significant decrease of the thermal conductivity, as demonstrated in several studies [182–185]. Despite the fact that these defects are partially recovered at high temperatures, the thermal conductivity values obtained for β -SiC at dpa levels comparable to ITER/DEMO devices decreases to around 1 to $10 \text{ W m}^{-1} \text{ K}^{-1}$ (depending on the irradiation temperature), making this material almost unsuitable for the expected thermal loads. This issue is ameliorated in modern SiC fiber composites that exhibit minimal degradation of their thermo-mechanical properties even when subject to high levels of neutron damage [176, 186]. However, their thermal conductivity in the pristine state values are low, and comparable to those of neutron-damaged monolithic CVD SiC. As a consequence, based on the current state of the literature, SiC does not meet the criteria to serve as a PFM in the divertor region.

With small percentages of TaC that fill up the grain boundaries, sintered W shows increased microhardness as a function of the TaC content, no cracking formation under ELMs-like thermal shock, and even increased

thermal conductivity at the low carbide percentage of 1% [187, 188]. Similar effects on the mechanical properties, thermal stability, and thermal conductivity are also reported for this W-HfC alloy [189]. However, the retention of hydrogen isotopes is generally increased under divertor-like deuterium bombardment [190] and can be one order of magnitude larger when compared with pure W in the case of W-1.1%TiC and W-3.3%TaC at 800 K, decreasing with increasing temperature. This might arise concerns on the tritium inventory. The direct use of TaC and HfC as PFMs has not been extensively investigated. Despite concerns related to their high carbon content, their thermal properties are at the threshold of meeting the requirements for withstanding divertor conditions without undergoing melting. However, the pure alloy system TaC-HfC, shows the highest melting point of the known materials at the right ratio of Ta and Hf (4:1) [191, 192] and decent values of thermal conductivity that, in contrast to pure metals or diborides, increase with rising temperature [193]. Further studies, including tritium inventory and behaviour under neutron irradiation, should be pursued, since at the experimentally reported values of the melting temperature, heat capacity and thermal conductivity [193], the 4TaC-1HfC alloy system would withstand type-I ELMs heat loads at the divertor with an armor thickness of about 5 mm. Rather than for their individual potential, TaC and HfC are added to the list of PFMs to calculate defects formation energies as a proxy of their ultra-high temperature alloys.

Given the melting temperature, heat capacity, and the thermal conductivity reported in literature [194], vanadium carbide (VC), can only withstand steady-state conditions, contrary to its boride form. Furthermore, its high-temperature stability is moderate, but its ability to act as a barrier for hydrogen permeation is noteworthy, which has led to the exploration of various type of vanadium carbides (V_xC_y) as a coating layer for structural fusion materials [195, 196]. The small hydrogen diffusion is attributed to its high hydrogen penetration barriers and large endothermic detrapping energy of H atoms in C vacancies. Previous test of the V_xC_y behavior under neutron irradiation reports hardening and increased electrical resistivity [197, 198]. Even if more investigation is required to understand degradation of the thermal properties induced in the presence of a plasma flux, this material does not qualify to sustain divertor heat loads and is discarded from the list of top PFM candidates.

Ta₂C, along with the other carbides emerging from the previous ranking selection criteria - TaC, HfC, WC, and W₂C - has also been proposed in the PMF field, but solely as a dispersion agent to enhance mechanical properties, suppress the embrittlement of W, and improve the migration of grain boundaries [199]. Ta₂C has been explored also as a bonding material for joining the structural materials or as a cooling system to the W armor [200]. Although Ta₂C is not extensively investigated as an alternative to W, its promising melting temperature

raises interest. However, the current lack of available literature on the heat capacity and thermal conductivity of this material hinders the determination of its capability to withstand divertor conditions and to compare it with the top PFM. Therefore, we refrain from conducting additional follow-up studies on Ta_2C at this time.

The last class of ceramic materials that emerges from the Pareto set analysis is that of tungsten carbides, in particular WC and W_2C . As previously mentioned, they might be applied as alloying compounds of a pure W armor [201, 202], but their thermo-mechanical properties and response under plasma and neutron irradiation are considered good enough to be considered and studied as an alternative PFM at the divertor [203, 204] and therefore these are retained in our ranking. At high temperatures, WC has a lower value of thermal conductivity when compared with pure W (reaching around 2/3 of its value). However, WC has a thermal shock coefficient that is 3 times higher, indicating better resistance to thermal shocks, and a Vickers hardness that is higher by a factor of 8 at room temperature to 20 at operating temperature. WC shows a good tolerance to neutron irradiation when compared to other carbides in terms of cracking resistance. Regarding the interaction with plasma, WC shows slightly higher sputtering rate and hydrogen retention than W. W_2C has been mainly applied as composites compound of both W [202] and WC [205]. When W_2C is subject to He ion bombardment, contrary to W, He bubbles do not form inside its crystal grains [202]. These bubbles are the early stages of the fuzz layer. The improved mechanical properties and surface layer stability of tungsten carbides are potentially offset by reduced thermal properties and increased sputtering and hydrogen retention, which has led to ongoing debates over their applicability as substitutes for W or as composites with the latter metal.

c. Nitrides The rhombohedral structure of boron nitride (BN) is selected according to the d^{SS} ranking, contrary to the cubic phase which is discarded due to the d^{ELMs} ranking. Other two polymorphs of boron nitride are well-known: the hexagonal polytype, discarded during the data cleaning procedure due to discrepancies in reported properties that matched another polymorph according to references, and the wurtzite polytype, not documented in MPDS. The melting temperatures and heat capacities of the polymorphs are in agreement with the KDE value extracted from MPDS [63, 206], but significant discrepancies arise in the thermal conductivities. Computed values of isotopically pure crystals of BN are around $1,900 \text{ W m}^{-1} \text{ K}^{-1}$ [207, 208], while experimental measurements report values that fall within the range of $150\text{--}550 \text{ W m}^{-1} \text{ K}^{-1}$ [209–213]. Thermal conductivities of this order of magnitude would justify the potential application of boron nitride as PFM, even at the divertor region, contrary to what the KDE values suggest. Although the effect of neutron bombardment on the thermal conductivity of BN is not extensively investigated, thermal annealing shows limited impact on the neutron-

induced damage of an irradiated BN structure [214], indicating a potential irreversible degradation of its thermal conductivity. Nonetheless, the chemical and thermal stability of BN, its limited physical sputtering, high thermal conductivity, and resistance to thermal shocks, has motivated its application as first-wall protective layer in fusion devices in the past [213, 215]. The interaction of BN with the plasma requires further investigation. On the one hand, cubic and hexagonal BN are highly promising for hydrogen barrier applications within the refractory nitrides class, exhibiting a diffusion barrier to hydrogen migration of approximately 3.0 eV [216]. On the other hand, BN shows high hydrogen permeability and solubility, which may lead to significant tritium inventories [217]. The ability of BN to efficiently store hydrogen molecules is linked to specific structural characteristics, such as nanotubes and hexagonal structures with high porosity and structural defects [218]. While these features are intentionally pursued for certain applications, they should be avoided when considering BN suitability as a PFM. Given its intriguing thermal properties and the necessity to conduct further investigations under operational conditions, BN is included in the list of leading PFM candidates, specifically in its cubic polymorph (c-BN). Recently, a material sharing the same crystal structure as c-BN, boron arsenide (BAs), has emerged as the second-highest thermally conducting material among all known isotropic crystals, after diamond [219, 220]. The highest experimentally measured thermal conductivity for BAs single crystals is $1,300 \text{ W m}^{-1} \text{ K}^{-1}$. However, the thermal stability of BAs is compromised as it decomposes into $B_{13}As_2$ at 1,200 K, releasing arsenic gas under atmospheric pressure [221]. This negates its application as PFM.

Another promising material, but quite unexplored for PFM application, is represented by the hexagonal, cubic, rhombohedral, orthorhombic, and amorphous boron-carbon nitride BC_2N . This material posses thermal and mechanical properties that lie between those of carbon diamond and boron nitride (c- and h-BN). Cubic, hexagonal and rhombohedral BC_2N show impressive Vickers hardness value (greater than c-BN) [222–225]. A thermal conductivity that is almost comparable with carbon diamond is calculated for h- BC_2N [224] and close to that of c-BN is estimated for orthorhombic BC_2N [226]. The Debye temperature of both hexagonal and orthorhombic BC_2N is estimated close or even higher than diamond, with values between 1,700–2,000 K [227, 228]. The heat capacity of the orthorhombic phase is predicted to lie between that of diamond and boron nitride [227, 229]. It can be assumed that the behavior of this class of compounds under divertor conditions is similar to their well-known precursors, as low-Z materials. However, differences are expected due to their chemical reactivity, and specific studies are necessary to determine their suitability as PFM. For these reasons, the hexagonal phase h- BC_2N is added to the list of top PFM candidates.

The C_3N_4 compound has been proposed in the past as

potential low-Z PFM alternative to graphite and CFCs, and a possible reduction of hydrogen diffusion and retention inside the material was hypothesized [230]. Given the difficulties connected with its synthesis [231], its thermo-mechanical properties are not well-known. Only estimates of its thermal conductivity are reported in literature, which range from 150 to 500 $\text{W m}^{-1} \text{K}^{-1}$ as a function of the phase considered [226, 232–234]. Bulk moduli rivaling that of diamond are also predicted for this crystal [233, 235]. Given the interesting thermo-mechanical features, the potentially reduced hydrogen inventory (a bottleneck in the application of carbon-based materials), and that synthesis paths to produce microcrystalline and noncrystalline C_3N_4 have been proposed [231, 236], the hexagonal structure $\beta\text{-C}_3\text{N}_4$ is also added to the list of top PFM candidates.

Vanadium nitride (VN) exhibits high heat capacity and moduli, but its inferior thermal properties, in terms of melting temperature and thermal conductivity [237], preclude it from any application as a PFM in a fusion tokamak reactor.

The case of aluminum nitride (AlN) can be compared to that of gallium nitride (GaN). For both of these materials, scientific literature on their potential use as divertor armor is limited (AlN) or absent (GaN). One of the biggest limitation in terms of applicability as PFM is dictated by their decomposition temperature in vacuum or at low N_2 level. Group III nitrides start to decompose in vacuum at temperatures that are in the order of one third of their melting temperature, and for AlN and GaN are calculated to be 1,040 and 850 K respectively [238]. This sets a temperature limit for high-temperature applications that is much lower than the estimate presented here; therefore, they are discarded from the list of promising PFMs. Despite this, AlN has also been proposed as a substrate for bolometric systems, which provide information on the spatial distribution of radiated power from the main plasma and the divertor region [239, 240]. It shows good impermeability to hydrogen isotopes [241, 242] and low susceptibility of its composition under low-energy H and He bombardment [243]. However, both neutron irradiation and high temperature have a detrimental effect on its thermal conductivity [244–246]. In contrast, GaN is mainly investigated for its electrical and optical properties for semiconductor device applications [247] and its thermo-mechanical behaviour under plasma and neutron bombardment is mostly unknown.

HfN shows thermo-mechanical properties that are not dissimilar from those of HfC [172], but a lower melting temperature which does not consent its application as primary PFM. However, alloy or composites of this material might be investigated in the future.

An ultra-high temperature ceramics that has only recently been identified as a ultra-high thermal conductive material is the hexagonal θ -phase of TaN [248]. Its astonishing thermal conductivity, estimated between 800–1,000 $\text{W m}^{-2} \text{K}^{-1}$ at room temperature (above 200 $\text{W m}^{-2} \text{K}^{-1}$

at 800 K), is just below that of c-BN, and more than double than the largest for a metal, silver. This might place θ -phase TaN at the top of the thickness ranking methods. To the best of our knowledge, its application as PFM has not been discussed yet, and a careful and critical analysis of its mechanical and thermal properties and their evaluation under plasma and neutron irradiation is thus needed. As stated in the reference article [248], phonons are the main heat carriers for this material, and the high thermal conductivity of the θ -phase TaN is caused by a particular combination of factors: (i) weak electron-phonon scattering, (ii) low isotopic mass disorder, (iii) large frequency gap between acoustic and optical phonon modes [220] that, together with (iv) acoustic bunching, impedes three-phonon processes (which is however dominated by four-phonon scattering). θ -TaN is also added to the list of top PFM candidates.

Thanks to its decent thermal properties, TiN is selected by the d^{ELMs} ranking as one of the lowest performing material, but still able to sustain divertor conditions in a thin layer. Consistently, TiN was used in a stellarator fusion device as coating layer of multiple plasma-facing components [249] and has been recently proposed for DEMO as tritium permeation barrier of the first-wall in a sandwich-like structure [250]. It shows the capability to withstand hydrogen plasma shots in IR-T1 tokamak with no significant morphology defects [251] and its permeability to hydrogen is also confirmed computationally [216]. Although it may not be considered a favorable choice for a primary plasma-facing material, TiN has the potential to be used as a coating layer on plasma-facing components. Therefore, it is included to expand the list of the most promising candidates.

Finally, all the nitrides presented here have in common the material activation issues associated with the presence of nitrogen. The transmutation of nitrogen (^{14}N) under neutron irradiation produces long-lived carbon isotopes ^{14}C [252, 253] that possess a time-to-low-level-waste (time-to-LLW) in the order of thousands of years [35].

E. Revisited thickness ranking

The collection of materials obtained through the two-step ranking procedure - thickness (ELMs and SS) and Pareto (3p, 2p, 1p) rankings - has been qualitatively evaluated with the indication of the comparative ranking, which highlighted potential false negatives, and then with the review of the literature for their application as PFMs. The finalized list of PFM candidates is presented in Tab. IV. Their capacity to withstand heat loads is re-evaluated by calculating d^{SS} and d^{ELMs} with heat properties extracted directly from the literature references reported in the table. Both high and low temperature properties are reported, in order to calculate the thickness values at the two temperature extrema. Considering the two temperature ranges reported in Tab. IV, high-

temperature conditions are more representative of the thermal demands that the designated PFM in the divertor region must withstand. Therefore, the candidates are ranked in descending order of maximum d^{ELMs} at high-temperature. The candidates with a larger maximum thicknesses that can avoid melting are prioritized because their surface temperature can be further decreased by reducing their thickness, while keeping a minimum width that can sustain erosive processes.

Carbon-based materials are ranked at the top of the list, diamond and graphite, followed closely by the ceramic materials C_3N_4 and BC_2N , which are novel in the field of PFM, and the well-known BN. Within the metal-based materials, W shows the highest performance, followed by Mo and three transition-metal borides: TiB_2 , ZrB_2 , and HfB_2 . The extensively researched WC [203, 204] and the recently investigated θ -TaN [248] exhibit adequate thermal properties, with maximum thicknesses of approximately 4 mm. All the other materials possess d^{ELMs} values ≤ 2.5 mm, significantly lower than the current minimum reported thickness design for a W divertor of 6 mm [254]. Consequently, pure Ta, Re, VB_2 , TaC, Cr, TaW, TiN are likely unsuitable for use as primary PFM. However, they could also be utilized as coating layers or dopants of the primary PFM. Additionally, they might be incorporated as constituents within alloy systems or composite materials. Only two materials within the selected set showed $d^{ELMs} \leq 0$ under both temperature conditions: W_2C and HfC. Although these materials do not exhibit exceptional performance, they are still included in the list. While the former may be considered as a potential contaminant of the high-performing WC, the latter represents one component of the two prototype crystals that constitute the aforementioned 4TaC-1HfC alloy system.

V. SBE AND H-IFE WORKFLOWS RESULTS

The crystal structures of the 21 PFM candidates are retrieved from MPDS if the selected polymorphs are available; otherwise, they are directly obtained from literature crystallographic data. The crystal structures are then employed as the only input required by the Surface Binding Energy (SBE) and the Hydrogen Interstitial Formation Energy (H-IFE) workflows.

The results of the SBE workflow screening are reported in Tab. V. E_b is the SBE of a surface atom, while $E_p(D)$ is threshold energy of physical sputtering, in this case the minimum energy that an impinging deuterium atom (D) must possess to remove the target atom from the surface (see Eq. 12). For each material, a single value for $\overline{E_b}$ and for $\overline{E_p}(D)$ is calculated by averaging the values of individual elements using stoichiometric weighted average (SWA). The weights for this averaging process are determined from the stoichiometric ratios of the elements present in the material. The PFM candidates are then ranked in descending order of $\overline{E_p}(D)$, which is the most

crucial value in assessing the material susceptibility to surface particle sputtering, thereby influencing the erosion rate and the contamination of the plasma core. The highest-performing materials are high-Z transition metals, in particular Re, TaW, W, and Ta, followed by their carbide, nitride and boride forms. The lowest $\overline{E_p}(D)$ values are obtained for low-Z transition metal and ceramics. As shown in Eq. 12, the mass difference between plasma ions and the target surface atom defines the amount of energy that can be transferred during an elastic collision, which is maximum at equal masses. This implies that, despite the chemistry at the surface, hence the SBE of a given atom, the atomic mass governs its susceptibility to sputtering. Indeed, even if the highest $\overline{E_b}$ are obtained for HfC, TaC, and graphite (C-194), low $\overline{E_p}(D)$ are also shown, due to the low atomic mass of the carbon atom. In particular, in the case of HfC, TaC, and WC, the transition metals in the carbide surface display impressive E_b values, higher than in their pure metallic forms. It is important to emphasize that in this cases preferential sputtering towards the carbon atom would occur, leaving a carbon-depleted surface with modified thermal properties.

The results of the H-IFE workflow are presented in Tab. VI, where the hydrogen interstitial formation energies $\Delta E^f(H_i)$ of the 21 PFM candidates are reported in descending order. Two values are reported, $\Delta E_a^f(H_i)$ and $\Delta E_m^f(H_i)$; the first is calculated from a reference hydrogen atom (*a*) as a reservoir, while the second from a reference hydrogen molecule (*m*), which is reported for comparison with literature. Their difference represent the H_2 binding energy, which in our calculation (excluding ZPE) is equal to -2.312 eV. A decrease of $\Delta E^f(H_i)$ leads to an exponential increase of the hydrogen solubility in the crystal, as reported in Eq. 15; this is an undesirable phenomenon for PFM, which need to minimize tritium inventory for reasons of safety and fuel efficiency. Only 4 materials exhibit a positive $\Delta E_a^f(H_i)$: BN, C graphite, BC_2N , and C_3N_4 , all of which possess high atomic density. Hence, aside from chemical interactions, there appears to be a correlation between smaller interstitial volumes, where atomic hydrogen must fit, and higher $\Delta E^f(H_i)$. The trend provided by $\Delta E^f(H_i)$ is only an initial indication that must be further refined by selecting more realistic energy references for hydrogen reservoirs, by including kinetic effects to define the hydrogen permeability inside the bulk of the crystal, and by considering damage and diffusion along pores and grains.

VI. COMPREHENSIVE EVALUATION OF PFM

The results obtained through the revisited thickness ranking, $d^{ELMs}(T_H)$, and the SBE and H-IFE workflows, $\overline{E_p}(D)$ and $\Delta E_a^f(H_i)$ respectively, are summarized in Tab. VII. The 21 PFM candidates selected are ranked according to the WF_i equation (see Sec. II A 2, Eq. 7).

The best PFM candidate according to this final rank-

TABLE IV. List of the top 21 PFM candidates identified in this study. The four properties required for the calculation of the heat balance equation (Eq. (4)) are retrieved directly from literature. Thermal conductivity k and heat capacity at constant pressure C_p are reported at both low (around RT) and high temperature. The actual values for low and high temperature may vary depending on the conditions documented in the literature. The maximum thickness to avoid melting in steady-state condition (d^{SS}) and during ELMs (d^{ELMs}) is calculated at low (T_L) and high (T_H) temperatures. Computational data are reported only when experimental measures are not available.

Formula	T_m (K)	Ref.	$k(T_L)$ (W m ⁻¹ K ⁻¹)	T_L (K)	$k(T_H)$ (W m ⁻¹ K ⁻¹)	T_H (K)	Ref.	$C_p(T_L)$ (J mol ⁻¹ K ⁻¹)	T_L (K)	$C_p(T_H)$ (J mol ⁻¹ K ⁻¹)	T_H (K)	Ref.	ρ (g cm ⁻³)	Ref.	MM (g mol ⁻¹)	$d^{SS}(T_L)$ (mm)	$d^{SS}(T_H)$ (mm)	$d^{ELMs}(T_L)$ (mm)	$d^{ELMs}(T_H)$ (mm)
C (diamond)	3,950 ⁽¹⁾⁽²⁾ [71, 255]		2,300	300	1,540	400	[63]	6.2	300	24	1,200	[63]	3.51	[63]	12.01	406.53	272.20	361.60	253.51
C (graphite)	3,950 ⁽²⁾ [71]		1,950	300	448	1,200	[63]	8.6	300	23	1,200	[63]	2.20	[63]	12.01	344.66	79.18	300.28	66.17
h-C ₃ N ₄	3,500 ⁽³⁾ [235]		520	300	520	300	[232]	30	300	80	1,200	[256]	3.53	[235]	92.06	80.21	80.21	53.39	63.78
h-BC ₂ N	3,500 ⁽³⁾ [229]		2,000	300	400	1,000	[224]	28	300	84	900	[227]	2.90	[222]	48.84	308.50	61.70	264.74	50.40
c-BN	3,240 [63]		550	300	350	650	[210]	20	300	42	1,200	[257]	3.49	[210]	24.82	77.69	49.44	60.04	39.73
W	3,687 [63]		174	300	112	1,200	[63]	24	300	28	1,200	[258]	19.26	[63]	183.84	28.47	18.32	17.97	10.53
TiB ₂	3,193 [63]		65	300	70	1,300	[259]	63	300	83	1,200	[260]	4.95	[63]	69.49	9.03	9.72	4.23	5.38
Mo	2,895 [63]		138	300	96	1,200	[120, 261]	22	300	30	1,200	[120]	10.23	[63]	95.94	17.11	11.90	7.44	4.99
ZrB ₂	3,323 [63]		58	300	65	1,300	[259]	45	300	75	1,200	[262]	6.17	[63]	112.85	8.43	9.45	2.31	4.43
HfB ₂	3,373 [63]		51	300	60	1,300	[259]	50	300	80	1,200	[262]	10.50	[63]	200.11	7.54	8.87	1.98	4.10
θ -TaN	3,363 [63]		70	300	70	300	[248, 263, 264]	41	300	41	300	[265]	13.70	[63]	194.95	10.32	10.32	4.10	4.10
WC	3,022 [63]		120	300	70	1,000	[204]	36	300	52	1,000	[266]	15.60	[63]	195.85	15.64	9.12	7.48	3.94
Ta	3,290 [63]		58	300	60	1,200	[267]	26	300	28	1,200	[268]	16.63	[63]	180.95	8.34	8.63	2.12	2.53
Re	3,458 [63]		48	300	45	520	[269]	23	300	31	1,200	[270]	21.02	[63]	186.21	7.30	6.85	1.88	2.32
VB ₂	2,723 [63]		42	300	42	1,300	[259]	45	300	70	1,200	[168]	5.07	[271]	72.56	4.85	4.85	0.24	1.15
TaC	4,153 [63]		22	300	22	300	[272]	30	300	52	1,200	[273]	14.65	[63]	192.96	4.11	4.11	0.19	1.13
Cr	2,180 [63]		94	300	62	1,200	[63]	22	300	32	1,200	[274]	7.20	[63]	52.00	8.30	5.47	1.29	0.75
TaW	3,450 [148]		54	673	60	1,400	[275, 276]	25	300	28	1,200	SWA ⁽⁴⁾	17.78	[156]	364.79	8.19	9.11	-0.20	0.74
TiN	3,220 [63]		25	500	25	1,200	[277]	45	500	55	1,200	[278]	5.21	[63]	61.87	3.51	3.51	0.27	0.58
W ₂ C	3,073 [63]		30	300	30	300	[279]	59	300	77	1,000	[280]	14.80	[63]	379.69	3.99	3.99	-0.57	-0.001
HfC	3,273 [63]		30	300	10	1,000	[278, 281]	37	300	49	1,000	[278]	12.20	[63]	190.50	4.29	1.43	-0.20	-0.82

(1) Diamond T_m is the same as graphite due to graphitization process happening above 1,900 K. (2) Graphite sublimates at atmospheric pressure. (3) T_m of C₃N₄ and BC₂N are defined between those of diamond and boron nitride by looking at the predicted Debye temperatures. (4) SWA indicates that the C_p of TaW is calculated as a stoichiometric weighted average of the C_p of its metallic single-element constituents.

TABLE V. Summary of the properties of the 21 PFM candidates, calculated through the SBE workflow. The space group number (SG) is reported to define the polymorph selected for each crystal. The surface orientation is chosen by finding the lattice plane with minimum surface energy at a given termination, $\min\{E_{surf}^{hkl,\alpha}\}$. The surface binding energy, E_b , and threshold energy of physical sputtering, $E_p(D)$, are calculated for each inequivalent surface atoms of the 21 PFM candidates. The stoichiometric weighted average values are calculated for each material, respectively \overline{E}_b and $\overline{E}_p(D)$. The PFM candidates are reported in descending order of $\overline{E}_p(D)$.

Formula	SG	$\min\{E_{surf}^{hkl,\alpha}\}$ eV Å ⁻²	Miller index	element	E_b eV	$E_p(D)$ eV	element	E_b eV	$E_p(D)$ eV	element	E_b eV	$E_p(D)$ eV	\overline{E}_b eV	$\overline{E}_p(D)$ eV
Re	194	0.19	$\langle 001 \rangle$	Re	11.72	276.81							11.72	276.81
TaW	221	0.20	$\langle 110 \rangle$	Ta	12.34	283.44	W	10.90	254.28				11.62	268.86
W	229	0.22	$\langle 110 \rangle$	W	11.16	260.38							11.16	260.38
Ta	229	0.17	$\langle 110 \rangle$	Ta	10.92	250.67							10.92	250.67
HfC	225	0.12	$\langle 100 \rangle$	C	9.83	19.98	Hf	16.68	378.03				13.26	199.00
TaC	225	0.11	$\langle 100 \rangle$	Ta	15.12	347.25	C	9.39	19.10				12.26	183.17
W ₂ C	60	0.19	$\langle 111 \rangle$	W	11.10	258.83	C	9.80	19.93				10.67	179.20
WC	187	0.25	$\langle 100 \rangle$	C	7.91	16.09	W	12.87	300.11				10.39	158.10
TaN	187	0.19	$\langle 100 \rangle$	Ta	12.63	289.98	N	7.48	17.01				10.05	153.50
Mo	229	0.19	$\langle 110 \rangle$	Mo	8.66	107.49							8.66	107.49
HfB ₂	191	0.21	$\langle 101 \rangle$	Hf	11.21	253.89	B	8.12	15.34				9.15	94.86
ZrB ₂	191	0.20	$\langle 101 \rangle$	B	8.03	15.17	Zr	11.13	131.63				9.06	53.99
TiN	225	0.09	$\langle 100 \rangle$	N	8.90	20.25	Ti	11.32	73.06				10.11	46.65
Cr	229	0.22	$\langle 110 \rangle$	Cr	6.21	43.26							6.21	43.26
C	194	0.001	$\langle 001 \rangle$	C	16.71	33.96							16.71	33.96
TiB ₂	191	0.22	$\langle 101 \rangle$	B	8.16	15.40	Ti	10.31	66.51				8.87	32.44
VB ₂	191	0.15	$\langle 101 \rangle$	B	8.01	15.13	V	9.20	62.86				8.41	31.04
C	227	0.35	$\langle 110 \rangle$	C	11.23	22.83							11.23	22.83
BC ₂ N	160	0.23	$\langle 001 \rangle$	C	12.58	25.57	N	7.68	17.46	B	10.33	19.52	10.79	22.03
BN	216	0.04	$\langle 111 \rangle$	B	12.29	23.20	N	8.76	19.93				10.53	21.57
C ₃ N ₄	176	0.04	$\langle 100 \rangle$	N	7.76	17.66	C	12.30	25.01				9.71	20.81

ing is carbon diamond (C-227), which outperforms most of the alternatives in terms of thermal properties and hydrogen interstitial formation energy. However, its low resistance to physical sputtering and consequent hydrogen retention remains a bottleneck for its usage as pri-

mary PFM. The energy threshold of physical sputtering is even lower than that of graphite, which is notorious for its low resistance to hydrogen sputtering. The application of diamond and diamond-like carbon as coating layer might be more appealing, as it has been already studied

TABLE VI. Formation energy for hydrogen interstitial of the 21 PFM candidates. $\Delta E_a^f(H_i)$ and $\Delta E_m^f(H_i)$ are calculated using Eq. 16, hence not including ZPE effects, taking respectively the hydrogen atom and the hydrogen molecule as reference hydrogen reservoirs. The deviations from known literature values range around ± 0.1 eV. This variance can be attributed to both differences in the size of the supercells (larger in this study compared to most of the cited works), the utilization of different functionals, and the choice of a different H_2 chemical potential.

Formula	SG	$\Delta E_a^f(H_i)$		$\Delta E_m^f(H_i)$	
		(eV)	(eV)	This work	This work
BN	216	2.81	5.12	-	
C	227	2.71	5.02	4.9	[282]
BC ₂ N	160	1.45	3.76	-	
C ₃ N ₄	176	0.27	2.58	-	
TiN	225	-0.13	2.18	-	
VB ₂	191	-0.42	1.89	-	
TaC	225	-0.54	1.77	-	
HfB ₂	191	-0.67	1.64	-	
C	194	-0.94	1.37	-	
ZrB ₂	191	-1.01	1.30	-	
TiB ₂	191	-1.09	1.22	-	
TaN	187	-1.50	0.81	-	
W	229	-1.53	0.78	0.87	[283]
HfC	225	-1.57	0.74	-	
WC	187	-1.77	0.54	0.7	[284]
Mo	229	-1.80	0.51	0.62	[285]
Cr	229	-1.81	0.51	-	
W ₂ C	60	-1.88	0.43	-	
Re	194	-2.39	-0.076	-	
TaW	221	-2.46	-0.15	-0.02	[286]
Ta	229	-2.82	-0.51	-	

in the past [78, 79]; nevertheless, the current literature is missing a realistic estimation of diamond erosion rates under the plasma flux of the divertor region, a parameter that constrains the layer lifetime and defines the tritium co-deposition rate and total tritium inventory. Diamond might also be applied in composite materials, but further research on the effects of degradation processes on the diamond thermal properties and intragranular hydrogen solubility at divertor conditions is needed. BN shows similar capabilities than carbon diamond, despite a lower $d^{ELMs}(T_H)$; thus, quantifying how BN thermal properties are affected by neutron-induced defects at high temperatures is crucial to assess its applicability as primary PFM. BN low sputtering resistance should be investigated to define its tritium co-deposition rate, but less interaction with hydrogen isotopes is expected than for pure carbon. Swelling and cracking of BN can be mostly avoided if isotopically separated ¹¹B is utilized to synthesize the crystal; however, nitrogen transmutation into radioactive ¹⁴C can pose challenges in disposing the material at the end of its lifecycle. As expected and reassuringly, W is ranked at the top of the PFM candidates, showing the best thermal properties among

all metal-based materials and significant sputtering resistance, mainly dictated by its high atomic mass. W shows a negative $\Delta E_a^f(H_i)$; however, the diffusion of hydrogen in the perfect crystal is limited by the energy migration barrier. Indeed, it has been shown that diffusion through vacancy hydrogen traps dominates over interstitial diffusion below 1,500 K [287]. Both BC₂N and C₃N₄ show properties that are comparable with the high-performing BN. These materials are understudied for their refractory properties due to difficulties with their synthesis, and little is known about their interaction with the extreme environment of a fusion reactor. Their low threshold energy of physical sputtering should be of primary concern, given the presence of carbon atoms in the crystal structure. Therefore, their response to plasma ion bombardment, coupled with tritium retention assessment, is key in evaluating their potential applicability. TaC and HfC have both good threshold energies of physical sputtering and reasonable hydrogen solubility compared to the other PFM candidates. However, a bottleneck is presented by their thermal properties: $d^{ELMs}(T_H)$ is slightly above 1 mm for TaC and even becomes negative for HfC. Exploring their potential as primary PFMs should then involve their alloy system 4TaC-1HfC. While availability of thermal properties for this alloy is limited, it has an estimated $d^{ELMs}(T_H)$ of about 5 mm, as shown in Sec. IV D. Re and Ta exhibit comparable performance, a high resistance towards physical sputtering due to their high atomic mass, reasonable thermal properties and very high hydrogen solubility. Their use as primary PFMs is limited by a $d^{ELMs}(T_H)$ around 2 mm, that might severely restrict their lifetime under erosion conditions. Furthermore, high tritium intake can be expected given the strongly negative $\Delta E_a^f(H_i)$. TaW is the second-best candidate in terms of $\overline{E_p}(D)$, surpassed only by Re. Its thermal properties seem to limit its applicability as primary PFM; however, most of the literature sources are based on experimental measures on alloys of various compositions, and reliable data on the ordered crystal are still lacking. TaW shows some of the highest potential in terms of hydrogen solubility. Graphite's $d^{ELMs}(T_H)$ is second only to carbon diamond and its resistance to physical sputtering is the highest among all carbon-based materials, with hydrogen finding its lowest-energy interstitial site when adsorbed on top of a carbon site between two hexagonal planes. The interlayer space can accommodate interstitial hydrogen, in particular when the hexagonal structure is damaged. Despite that, the primary processes governing hydrogen migration into the graphite bulk involve intergranular diffusion on pore surfaces and penetration through grain boundaries. In the latter section of the ranking, a limited set of materials lacks outstanding performance, but their appealing thermal characteristics render them worthy of attention. TaN, HfB₂, WC, Mo, ZrB₂, and TiB₂ have $d^{ELMs}(T_H)$ values around 4 mm, and $\overline{E_p}(D)$ equal or higher than graphite. Evaluating their properties under divertor conditions would be of great relevance, since most of have not been tested as

TABLE VII. The selected 21 PFM candidates are ranked accordingly to the WF_i equation applied on the three properties calculated in this study: (i) maximum thickness to avoid melting during ELMs, $d^{ELMs}(T_H)$; (ii) threshold energy of physical sputtering, $\overline{E_p}(D)$; (iii) hydrogen interstitial formation energy, $\Delta E_a^f(H_i)$. The Pareto layer number l of each material is also reported, showing consistency with the WF_i ranking method.

WF_i (%)	l	Formula	SG	$d^{ELMs}(T_H)$ (mm)	$\overline{E_p}(D)$ (eV)	$\Delta E_a^f(H_i)$ (eV)
86.3	1	C	227	253.51	22.83	2.71
69.6	1	BN	216	39.73	21.57	2.81
64.8	1	W	229	10.53	260.38	-1.53
63.1	2	BC ₂ N	160	50.40	22.03	1.45
60.3	1	TaC	225	1.13	183.17	-0.54
55.9	2	C ₃ N ₄	176	63.78	20.81	0.27
54.4	1	Re	194	2.32	276.81	-2.39
51.7	2	TaW	221	0.74	267.35	-2.46
48.5	2	HfC	225	-0.82	199.00	-1.57
45.8	2	Ta	229	2.53	250.67	-2.82
45.7	1	C	194	66.17	33.96	-0.94
39.8	1	TaN	187	4.10	153.33	-1.50
39.3	2	W ₂ C	60	-0.001	177.19	-1.88
37.6	1	HfB ₂	191	4.10	94.85	-0.67
36.8	2	WC	187	3.94	156.59	-1.77
33.8	1	TiN	225	0.58	46.66	-0.13
25.6	1	VB ₂	191	1.15	31.04	-0.42
23.7	2	Mo	229	4.99	107.49	-1.80
21.3	1	ZrB ₂	191	4.43	53.94	-1.01
15.8	2	TiB ₂	191	5.38	32.44	-1.09
6.3	3	Cr	229	0.75	43.26	-1.81

primary PFMs, except for WC and Mo, which are well-studied materials considered as alternatives to pure W divertors. Finally, due to the low $d^{ELMs}(T_H)$, combined with mediocre sputtering and hydrogen solubility resistances, W₂C, TiN, VB₂ and, Cr are unlikely to be employed as primary PFMs, protective layers, or composite materials, given that superior alternatives are available.

VII. CONCLUSIONS AND OUTLOOK

The goal of finding divertor PFMs alternative to W has been assessed by defining a target dataset of crystal structures and properties, the inorganic crystal database MPDS [30, 31], and a set of physical constraints that every candidate needs to satisfy. Three main loads affect the PFM of the divertor - heat, plasma particles, and neutrons - and following for a few milliseconds these interactions is computationally prohibitive even for a single material. In this work we first focused on the heat balance equation that the PFM is subject to during steady-state conditions and ELM events. Three experimentally measurable thermal properties are used (T_{melt} , k , and C_p), and when all of these are available on MPDS, the heat balance equation is used via the thickness ranking procedure to discriminate between materials that melts

or not under divertor heat loads, discarding the latter. When the heat equation could not be solved due to the lack of measure properties, materials were ranked accordingly to the Pareto ranking method on the subset of the available thermal properties. 71 PFM candidates have been selected at this stage, and all of them have gone through a selective literature review of their properties under relevant operational conditions. This has led to a further screening of the candidates, which, following the use of the comparative ranking criteria to test for false negatives (i.e., materials erroneously discarded) results in a total of 21 potential PFMs. The crystal structures of these materials are used as single input of the two first-principles workflows developed to calculate the candidate surface biding energy (SBE) and the hydrogen-interstitial formation energy (H-IFE). These two properties are used as proxies for two undesired phenomena produced by the plasma bombardment of exposed PFM: (i) the erosion of the surface due to sputtering; (ii) the inventory of tritium inside the material due to hydrogen isotopes diffusion. The materials selected via the screening process together with the properties calculated in this study are summarized in Tab. VII. Well-known and already proposed PFMs appear in this list, such as tungsten in its pure metallic (W) and carbide forms (WC and W₂C), diamond and graphite, boron nitride, and other transition metals, such as Mo, Ta and Re. Other less investigated refractory materials show interesting characteristic that are worth further analysis, such as TaN in its θ -phase, HfB₂, ZrB₂, and TiB₂. These do not excel in terms of threshold energy for physical sputtering or hydrogen-interstitial formation energy, but they are still acceptable when compared with those of graphite and tungsten. Especially, their good thermal properties make these appealing as primary PFMs, in particular since the recent possibility to synthesize borides with isotopically separated ¹¹B, which avoids the boron transmutation reaction. Novel PFMs are also reported, in particular BC₂N, C₃N₄, TaW in its ordered cubic structure, and 4TaC-1HfC, which, for simplicity, is examined in this study in terms of its carbide components. To the best of the authors' knowledge, there is no literature investigation of the thermal properties of these materials at high temperature under plasma and neutron bombardment. Some limitation come from challenging synthesizability, especially with the goal of obtaining homogeneous phases. In this context, computational studies may offer valuable insights by predicting their thermal properties across different conditions.

This work also highlights the importance of considering the engineering constraints that a PFM in the divertor region needs to satisfy; the combination of the heat, plasma, and neutron loads narrows down the material space available for potential candidates. The three thermal properties - melting temperature, thermal conductivity, and heat capacity - of a new PFM candidate must always be measured or computed, if the aim is to prevent melting and thermal shock damages. When these

constraints are accounted for, many recently proposed W alternatives are excluded from consideration as divertor PFMs. In addition, their evolution during degradation processes induced by plasma and neutron bombardment, as well as changes in composition resulting from elemental transmutation, should be evaluated. Last, the creation of the two semi-automated workflows is also meant as a proof of concept for the application of the proposed protocol to large high-throughput studies of materials, since the calculated properties have broader utility beyond this specific domain of application.

VIII. ACKNOWLEDGEMENTS

This work has been carried out within the framework of the EUROfusion Consortium, via the Euratom Research and Training Programme (Grant Agreement No 101052200 - EUROfusion) and funded by the Swiss State Secretariat for Education, Research and Innovation (SERI). Views and opinions expressed are however those of the author(s) only and do not necessarily reflect those of the European Union, the European Commission, or SERI. Neither the European Union nor the European Commission nor SERI can be held responsible for them. N.M. acknowledges support from NCCR MARVEL, the National Centre of Competence in Research on Computational Design and Discovery of Novel Materials, funded by the Swiss National Science Foundation (Grant No. 205602).

APPENDIX

TABLE VIII. Ranking of the top 20 PFM candidates based on the minimum thickness (d^{ELMs}) required to prevent surface melting under divertor operation conditions during type-I ELMs. The KDE (Kernel Density Estimated) and SD (Standard Deviation) columns provide information on the estimated value and variability of each property in the database. SD values are expressed as a percentage of the KDE value. The calculation of d^{ELMs} is performed using Eq. (4) and the input data presented in Tab. I, while its SD is obtained through error propagation.

Chemical formula	T_m (K)		G (GPa)		B_s (GPa)		B_T (GPa)		E (GPa)		KH (GPa)		MH (-)		k ($W K^{-1} m^{-1}$)		$C_p \cdot \rho$ ($JK^{-1} cm^{-3}$)		d^{ELMs} (mm)	
	kde	SD (%)	kde	SD (%)	kde	SD (%)	kde	SD (%)	kde	SD (%)	kde	SD (%)	kde	SD (%)	kde	SD (%)	kde	SD (%)	kde	SD (%)
C dia	4,712.1	17.9	96.5	332.4			443.0	7.8	1,186.0	0.0	68.6	0.0	10.0	52.7	1,100.2	42.8	1.8	122.5	205.0	52.2
W rt	3,687.1	16.9	160.2	23.7	297.0	1.9	310.7	6.1	410.1	0.0					174.0	15.8	2.5	25.0	18.0	37.2
Mo rt	2,895.5	11.9	126.5	0.0	285.0	5.7	260.0	4.1	326.9	0.0					138.0	0.0	2.6	26.3	7.9	34.2
Cu	1,357.1	10.4			137.0	24.3	141.9	19.5					401.0	5.6	5.2	11.0	7.9	38.0		
Ir	2,718.9	6.3					385.0	13.9					138.8	3.5	2.9	0.2	7.3	17.8		
Os rt	3,307.7	9.5	320.0	0.0			389.8	12.4	800.0	0.0			86.7	54.7	2.9	0.0	5.7	91.2		
AlN	3,286.9	13.3	3.5	0.0	202.0	0.0	207.5	8.3	353.0	0.0	12.0	0.0	82.4	203.9	2.4	0.0	4.4	379.5		
Ru rt	2,606.0	6.4	199.0	0.3			314.9	8.2					103.0	11.8	2.9	6.5	3.8	34.2		
Rh	2,236.2	6.3					276.6	6.8					132.5	19.4	3.0	0.2	3.7	48.6		
ZrB ₂	3,323.0	0.6	220.0	4.1			216.0	19.5	493.5	5.8	27.6	22.7	64.4	65.4	2.9	7.7	3.4	123.5		
TiB ₂ rt	3,191.4	4.1	226.7	37.8			252.3	21.8	500.5	31.2	33.1	9.1	64.5	49.2	3.3	0.0	3.4	91.2		
HfB ₂	3,373.1	3.1	224.7	4.0			200.0	18.2	503.1	3.5	22.2	6.0	51.0	99.4	2.8	7.8	2.1	228.6		
Re	3,455.1	14.9	179.0	1.3	365.2	0.0	364.0	21.5	454.0	0.0			47.9	3.8	2.9	0.0	2.1	57.1		
Ta	3,279.3	26.4			190.0	0.0	193.6	4.2	181.0	14.1			54.0	4.6	2.3	13.0	1.7	141.2		
TaC	4,153.1	1.3	200.6	10.7	265.0	5.3	344.0	4.3	424.8	28.8	22.1	10.5	22.2	0.0	5.0	11.1	1.5	13.3		
Cr rt	2,179.9	4.0			157.0	0.0	189.4	24.5					93.4	18.2	3.2	30.1	1.5	93.3		
GaN rt	2,782.6	26.6			170.0	8.3	251.7	12.3					65.7	111.7	2.5	0.0	1.3	430.8		
Ag	1,234.6	28.1	28.2	7.0			101.0	19.8					428.6	5.8	2.5	2.4	0.9	822.2		
TiN ht	3,220.0	1.9	196.7	57.7			271.4	35.5	473.6	47.7	17.4	13.2	9.0	0.0	29.0	7.3	4.5	3.7	0.9	22.2
HfC	4,188.1	12.6	192.0	0.0			254.0	3.1	461.0	0.0	25.1	10.1	20.0	0.0	2.4	0.0	0.1	500.0		

TABLE IX. Ranking of the top 13 PFM candidates based on the minimum thickness (d^{SS}) required to prevent surface melting under divertor operation conditions in steady-state. The KDE (Kernel Density Estimated) and SD (Standard Deviation) columns provide information on the estimated value and variability of each property in the database. SD values are expressed as a percentage of the KDE value. The calculation of d^{SS} is performed using Eq. (3) and the input data presented in Tab. I, while its SD is obtained through error propagation.

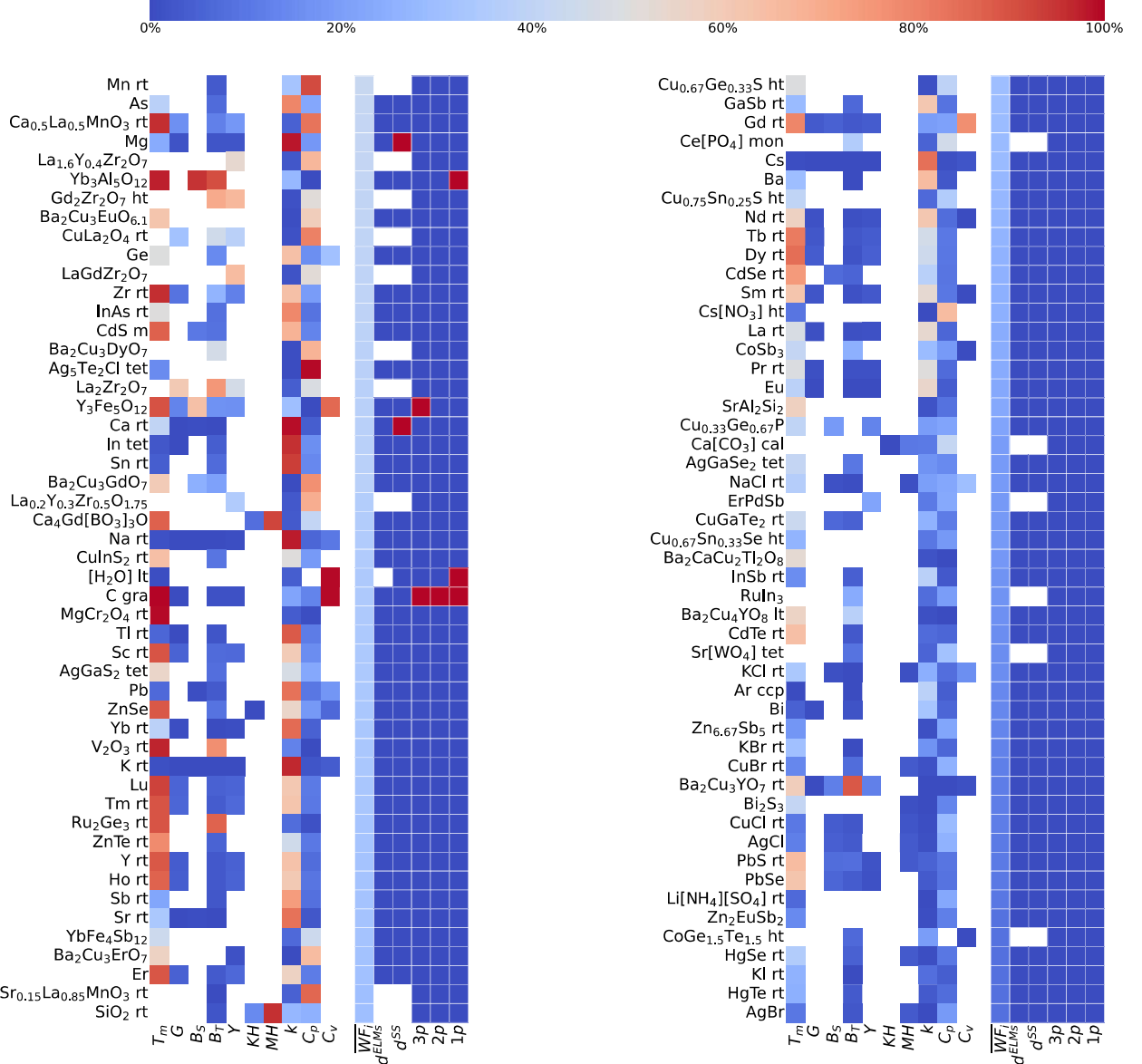
Chemical formula	T_m (K)		G (GPa)		B_s (GPa)		B_T (GPa)		E (GPa)		KH (GPa)		MH (-)		k ($W K^{-1} m^{-1}$)		d^{SS} (mm)		
	kde	SD (%)	kde	SD (%)	kde	SD (%)	kde	SD (%)	kde	SD (%)	kde	SD (%)	kde	SD (%)	kde	SD (%)	kde	SD (%)	
AlP	2,100.1	24.0					86.5	4.2					5.5	0.0	92.0	0.0	7.8	29.9	
AlAs	2,013.0	0.0			72.0	0.0	74.0	3.2							84.0	0.0	6.7	0.0	
GaP rt	1,740.0	3.4					86.9	8.3	110.9	27.8					75.2	0.0	5.0	4.5	
VB ₂	2,722.9	6.5	241.0	0.0			281.9	7.5	340.1	46.4	24.0	0.0			42.1	34.8	4.9	35.6	
ZnS ht	2,100.1	2.6					78.5	0.0							46.0	0.0	3.9	3.2	
W ₂ C orth	3,003.0	0.0					329.0	0.0	216.0	0.0					29.3	0.0	3.8	0.0	
CrB ₂	2,473.0	0.0													34.0	37.7	3.5	37.7	
Be ₁₃ Zr	2,200.0	0.0													36.3	8.7	3.2	8.7	
BN rhom	3,240.0	0.0					33.4	0.0							22.4	34.8	3.2	34.8	
Be ₁₇ Ta ₂	2,261.0	0.0							240.0	0.0	110.1	122.0				33.7	13.9	3.1	13.9
WSi ₂	2,438.0	0.5													30.3	3.6	3.1	3.6	
MoSi ₂ rt	2,273.0	1.4							230.0	0.0	402.6	34.1				32.7	39.6	3.0	39.6
DyIn ₃	1,423.0	0.0													60.0	0.0	3.0	0.0	

TABLE X. Top 6 PFM candidates based on the Pareto ranking procedure applied to the 3p subset of materials, where only materials with at least one property per category are classified (see Tab. II). The procedure criteria are summarized in Tab. III. The KDE (Kernel Density Estimated) and SD (Standard Deviation) columns provide information on the estimated value and variability of each property in the database. SD values are expressed as a percentage of the KDE value. Materials undergoing the thickness rankings are excluded from this procedure.

Chemical formula	T_m (K)		G (GPa)		B_s (GPa)		B_T (GPa)		E (GPa)		KH (GPa)		MH (-)		k ($W K^{-1} m^{-1}$)		$C_p \cdot \rho$ ($JK^{-1} cm^{-3}$)		$C_v \cdot \rho$ ($JK^{-1} cm^{-3}$)	
	kde	SD (%)	kde	SD (%)	kde	SD (%)	kde	SD (%)	kde	SD (%)	kde	SD (%)	kde	SD (%)	kde	SD (%)	kde	SD (%)	kde	SD (%)
Ba _{0.3} La _{0.7} MnO ₃ rt	46.4	0.0					85.3	11.5					5.4	0.0	4.3	8.2				
SrVO ₃ cub	90.0	0.0			151.0	0.0	255.9	4.0	224.0	0.0			12.8	0.0	4.3	0.0				
Ta _{0.5} W _{0.5} ht	91.0	0.0					142.0	0.0	224.0	0.0			65.0	7.4	3.0	19.2				
TiCoSb	105.0	0.0					257.0	16.6					16.6	43.2	3.5	23.6				
Y _{0.2} Zr _{0.8} O _{1.9} ht ₂	161.0	0.0					196.0	0.0	379.0	0.0			2.0	5.3	3.2	5.6				
Zr ₂ Al ₃ C ₄													8.8	52.2	3.6	0.0	0.1	500.0		

TABLE XI. Top 6 PFM candidates based on the Pareto ranking procedure applied to the $2p$ subset of materials, where only materials with at least one property in two different categories are classified (see Tab. II). The procedure criteria are summarized in Tab. III. The KDE (Kernel Density Estimated) and SD (Standard Deviation) columns provide information on the estimated value and variability of each property in the database. SD values are expressed as a percentage of the KDE value. Materials undergoing the thickness and $3p$ Pareto rankings are excluded from this procedure.

TABLE XII. Top 21 PFM candidates based on the Pareto ranking procedure applied to the $1p$ subset of materials, where only materials with at least one property are classified (see Tab. II). The procedure criteria are summarized in Tab. III. The KDE (Kernel Density Estimated) and SD (Standard Deviation) columns provide information on the estimated value and variability of each property in the database. SD values are expressed as a percentage of the KDE value. Materials undergoing the thickness, $3p$ and $2p$ Pareto rankings are excluded from this procedure. The full list consists of 26 materials, but only 21 are shown in the table. The remaining 5 materials, which belong to the same polymorphs (BC_2N and C_3N_4), have been omitted as they exhibit highly similar properties. $\text{CoC}_{36}\text{Cl}_2$ sta4, $\text{FeC}_{24}\text{Cl}_3$, and $\text{SbC}_{16.09}\text{C}$ are the MPDS chemical formulas for graphite intercalated with CoCl_2 , FeCl_3 , and SbCl_5 .



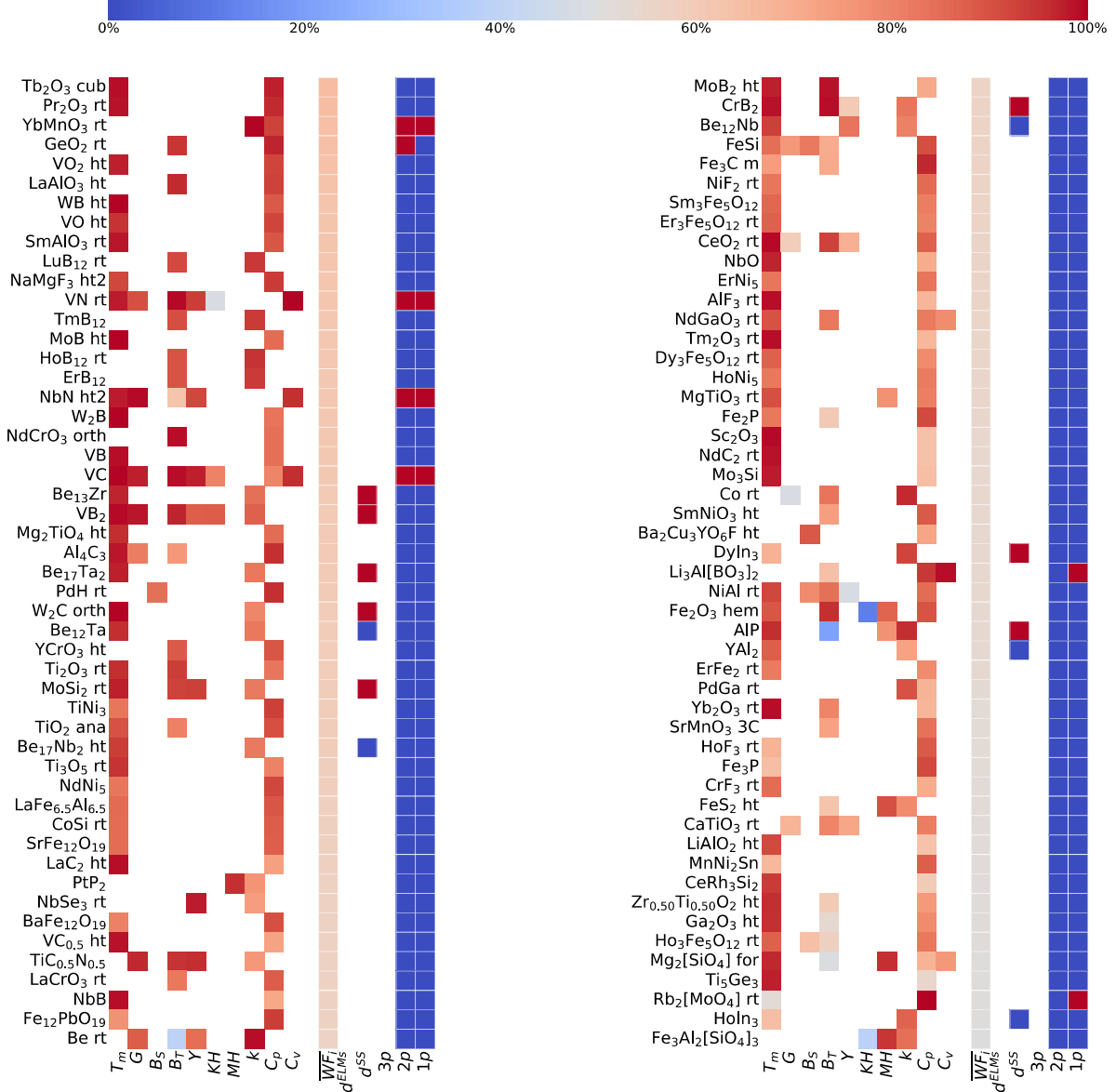


FIG. 7. Heatmap representation of the materials ranked from 1 (top left) to 100 (bottom right) according to the comparative ranking procedure. The materials are classified into the $2p$ subset and arranged in order based on their weighted average win-fraction (WFi) scores, with a maximum potential score of 66.7%. The figure also includes the individual win-fraction ($WF_{i,k}$) values for each property of the materials.

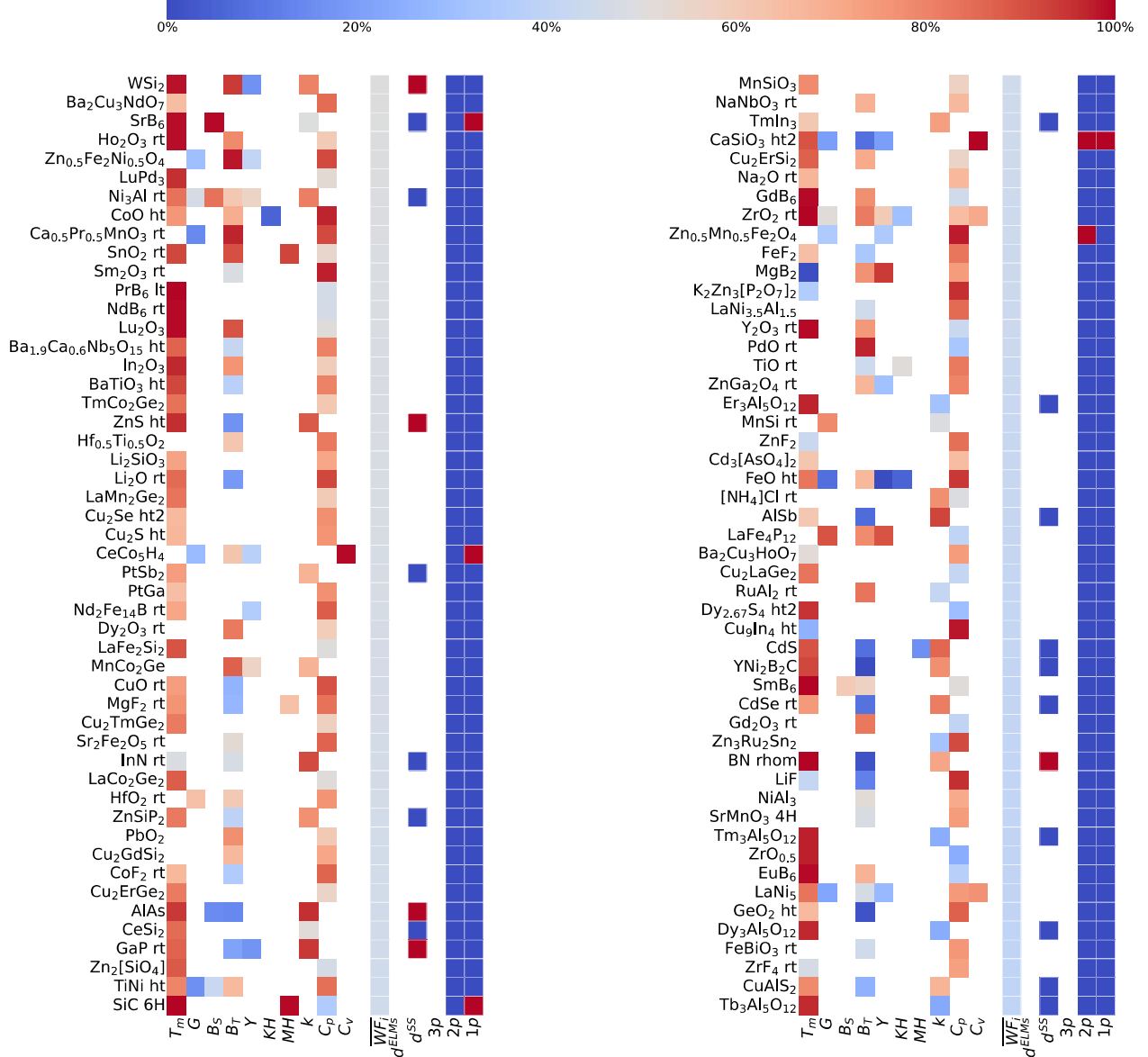


FIG. 8. Heatmap representation of the materials ranked from 101 (top left) to 200 (bottom right) according to the comparative ranking procedure. The materials are classified into the 2p subset and arranged in order based on their weighted average win-fraction (\overline{WFi}) scores, with a maximum potential score of 66.7%. The figure also includes the individual win-fraction ($WF_{i,k}$) values for each property of the materials.

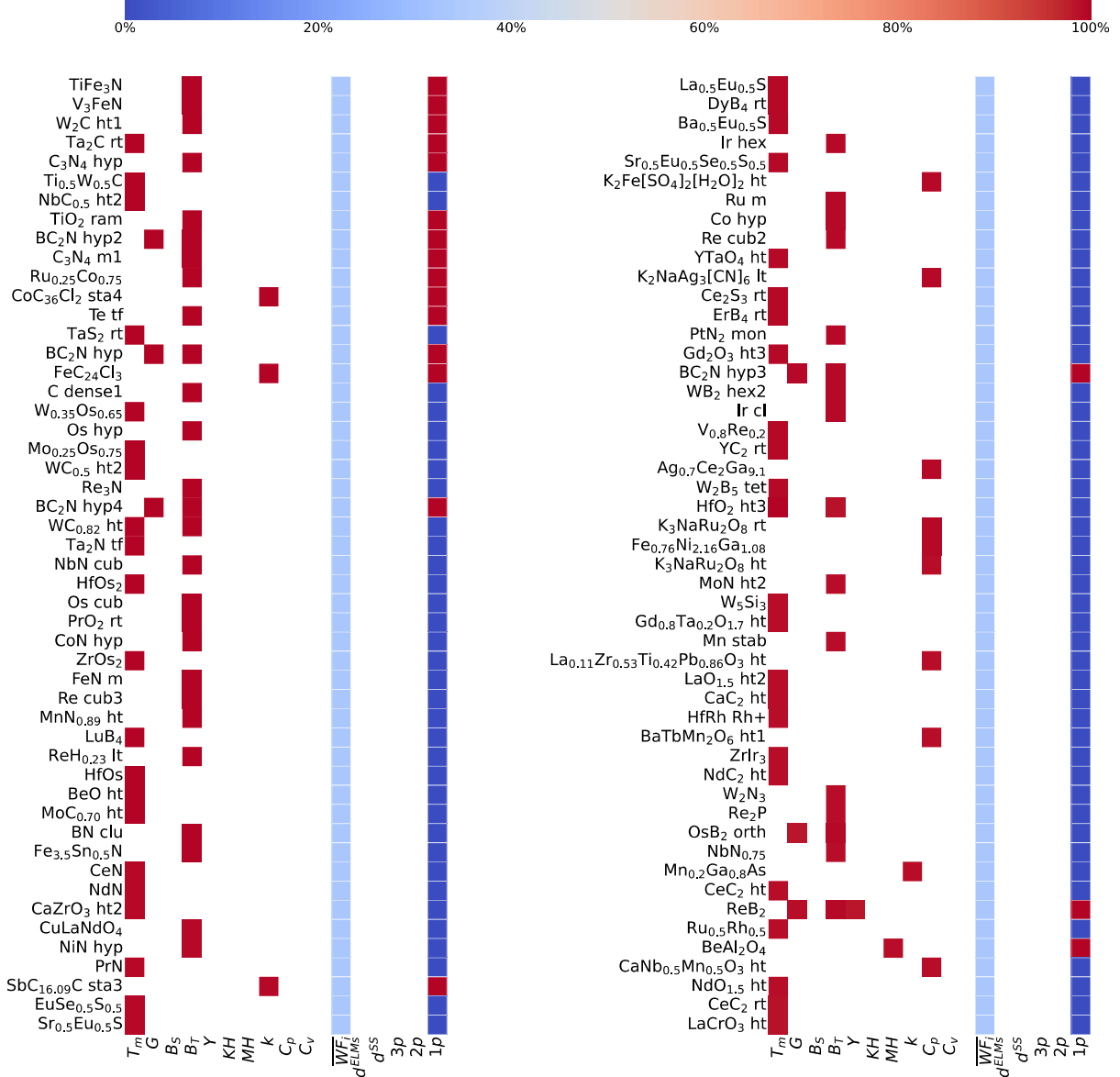


FIG. 9. Heatmap representation of the materials ranked from 1 (top left) to 100 (bottom right) according to the comparative ranking procedure. The materials are classified into the $1p$ subset and arranged in order based on their weighted average win-fraction ($\overline{WF_i}$) scores, with a maximum potential score of 33.3%. The figure also includes the individual win-fraction ($WF_{i,k}$) values for each property of the materials.

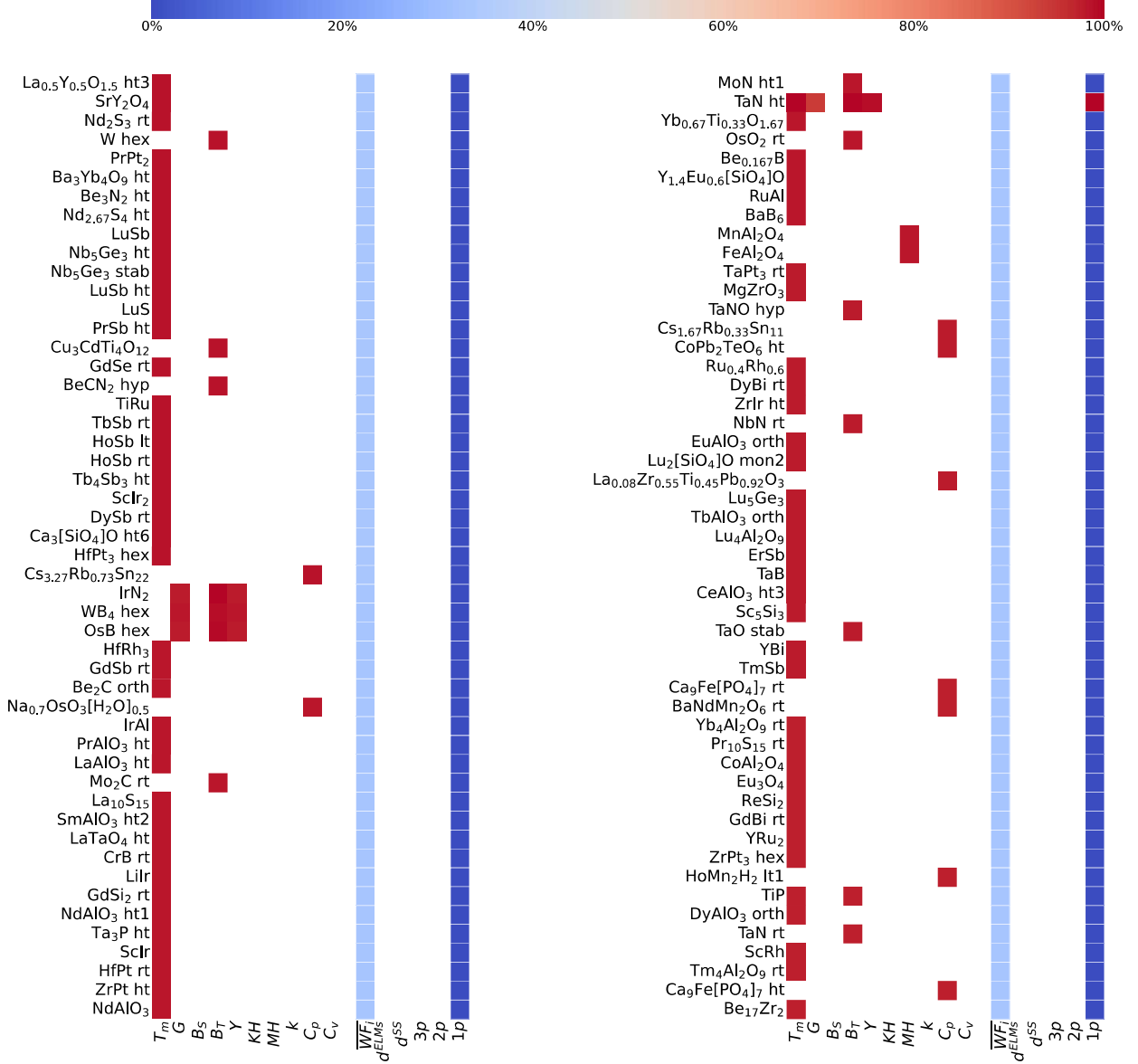


FIG. 10. Heatmap representation of the materials ranked from 101 (top left) to 200 (bottom right) according to the comparative ranking procedure. The materials are classified into the $1p$ subset and arranged in order based on their weighted average win-fraction (\overline{WF}_i) scores, with a maximum potential score of 33.3%. The figure also includes the individual win-fraction ($WF_{i,k}$) values for each property of the materials.

[1] Advantages of fusion (2022), [Online; accessed 22. Nov. 2022].

[2] S. Banacloche, A. R. Gamarra, Y. Lechon, and C. Bustrelo, Socioeconomic and environmental impacts of bringing the sun to earth: A sustainability analysis of a fusion power plant deployment, *Energy* **209**, 118460 (2020).

[3] A. Fasoli, Essay: Overcoming the obstacles to a magnetic fusion power plant, *Physical Review Letters* **130**, 220001 (2023).

[4] J. Knaster, A. Moeslang, and T. Muroga, Materials research for fusion, *Nature Physics* **12**, 424 (2016).

[5] F. Arbeiter, E. Diegèle, U. Fischer, A. Garcia, A. Ibarra, J. Molla, F. Mota, A. Möslang, Y. Qiu, M. Serrano, *et al.*, Planned material irradiation capabilities of ifmif-dones, *Nuclear Materials and Energy* **16**, 245 (2018).

[6] ITER - the way to new energy (2022), [Online; accessed 22. Nov. 2022].

[7] J. Linke, J. Du, T. Loewenhoff, G. Pintsuk, B. Spilker, I. Steudel, and M. Wirtz, Challenges for plasma-facing components in nuclear fusion, *Matter and Radiation at Extremes* **4**, 056201 (2019).

[8] K. Hoshino, K. Shimizu, N. Asakura, T. Takizuka, M. Nakamura, and K. Tobita, Simulation study of an extended divertor leg for heat control in the slimcs demo reactor, *Contributions to Plasma Physics* **52**, 550 (2012).

[9] G. Federici, C. H. Skinner, J. N. Brooks, J. P. Coad, C. Grisolia, A. A. Haasz, A. Hassanein, V. Philipp, C. S. Pitcher, J. Roth, *et al.*, Plasma-material interactions in current tokamaks and their implications for next step fusion reactors, *Nuclear Fusion* **41**, 1967 (2001).

[10] R. Behrisch, G. Federici, A. Kukushkin, and D. Reiter, Material erosion at the vessel walls of future fusion devices, *Journal of Nuclear Materials* **313**, 388 (2003).

[11] G. Federici and A. R. Raffray, Raclette: a model for evaluating the thermal response of plasma facing components to slow high power plasma transients. part ii: Analysis of iter plasma facing components, *Journal of Nuclear Materials* **244**, 101 (1997).

[12] T. Evans, Elm mitigation techniques, *Journal of Nuclear Materials* **438**, S11 (2013).

[13] A. Loarte, G. Saibene, R. Sartori, D. Campbell, M. Beccoulet, L. Horton, T. Eich, A. Herrmann, G. Matthews, N. Asakura, *et al.*, Characteristics of type i elm energy and particle losses in existing devices and their extrapolation to iter, *Plasma Physics and Controlled Fusion* **45**, 1549 (2003).

[14] Y. Igitkhanov and B. Bazylev, Modeling of demo pfc erosion due to elm impact, *IEEE Transactions on Plasma Science* **42**, 2284 (2014).

[15] Y. Ueda, K. Schmid, M. Balden, J. Coenen, T. Loewenhoff, A. Ito, A. Hasegawa, C. Hardie, M. Porton, and M. Gilbert, Baseline high heat flux and plasma facing materials for fusion, *Nuclear Fusion* **57**, 092006 (2017).

[16] J. Blanchard, C. Martin, and W. Liu, Effect of elms and disruptions on fnsf plasma-facing components, *Fusion Engineering and Design* **135**, 337 (2018).

[17] G. De Temmerman, T. Hirai, and R. Pitts, The influence of plasma-surface interaction on the performance of tungsten at the iter divertor vertical targets, *Plasma Physics and Controlled Fusion* **60**, 044018 (2018).

[18] S. Van den Kerkhof, M. Blommaert, R. Pitts, W. Dekeyser, S. Carli, and M. Baelmans, Impact of elm mitigation on the iter monoblock thermal behavior and the tungsten recrystallization depth, *Nuclear Materials and Energy* **27**, 101009 (2021).

[19] J. M. Linke, T. Hirai, M. Rödig, and L. A. Singheiser, Performance of plasma-facing materials under intense thermal loads in tokamaks and stellarators, *Fusion science and technology* **46**, 142 (2004).

[20] R. Pitts, X. Bonnin, F. Escourbiac, H. Frerichs, J. Gunn, T. Hirai, A. Kukushkin, E. Kaveeva, M. Miller, D. Moulton, *et al.*, Physics basis for the first iter tungsten divertor, *Nuclear Materials and Energy* **20**, 100696 (2019).

[21] Design review for tungsten divertor shows way ahead (2022), [Online; accessed 22. Nov. 2022].

[22] J. W. Coenen, Fusion materials development at forschungszentrum jülich, *Advanced Engineering Materials* **22**, 1901376 (2020).

[23] J. You, G. Mazzzone, E. Visca, C. Bachmann, E. Autissier, T. Barrett, V. Cociolovo, F. Crescenzi, P. Domalapally, D. Dongiovanni, *et al.*, Conceptual design studies for the european demo divertor: Rationale and first results, *Fusion Engineering and Design* **109**, 1598 (2016).

[24] N. Asakura, K. Hoshino, H. Utoh, Y. Someya, S. Suzuki, C. Bachmann, H. Reimerdes, R. Wenninger, H. Kudo, S. Tokunaga, *et al.*, Plasma exhaust and divertor studies in japan and europe broader approach, demo design activity, *Fusion Engineering and Design* **136**, 1214 (2018).

[25] J. Reiser and M. Rieth, Optimization and limitations of known demo divertor concepts, *Fusion Engineering and Design* **87**, 718 (2012).

[26] J. Brooks, L. El-Guebaly, A. Hassanein, and T. Sizyuk, Plasma-facing material alternatives to tungsten, *Nuclear Fusion* **55**, 043002 (2015).

[27] G. Pintsuk and A. Hasegawa, Tungsten as a plasma-facing material, in *Comprehensive Nuclear Materials: Second Edition* (Elsevier, 2020) pp. 19–53.

[28] M. R. Gilbert, K. Arakawa, Z. Bergstrom, M. J. Caturla, S. L. Dudarev, F. Gao, A. Goryaeva, S. Hu, X. Hu, R. J. Kurtz, *et al.*, Perspectives on multiscale modelling and experiments to accelerate materials development for fusion, *Journal of Nuclear Materials* **554**, 153113 (2021).

[29] M. Rieth, R. Doerner, A. Hasegawa, Y. Ueda, and M. Wirtz, Behavior of tungsten under irradiation and plasma interaction, *Journal of Nuclear Materials* **519**, 334 (2019).

[30] feedback@tilde. pro, Materials Platform for Data Science (2022), [Online; accessed 22. Nov. 2022].

[31] Pauling File (2022), [Online; accessed 22. Nov. 2022].

[32] N. Marzari, A. Ferretti, and C. Wolverton, Electronic-structure methods for materials design, *Nature materials* **20**, 736 (2021).

[33] K. Lee, M. Yuan, and J. Wilcox, Understanding deviations in hydrogen solubility predictions in transition metals through first-principles calculations, *The Journal of Physical Chemistry C* **119**, 19642 (2015).

[34] M. R. Gilbert, M. Fleming, and J.-C. Sublet, Automated inventory and material science scoping calculations under fission and fusion conditions, Nuclear Engineering and Technology **49**, 1346 (2017).

[35] M. R. Gilbert, T. Eade, T. Rey, R. Vale, C. Bachmann, U. Fischer, and N. Taylor, Waste implications from minor impurities in european demo materials, Nuclear Fusion **59**, 076015 (2019).

[36] G. Federici, W. Biel, M. Gilbert, R. Kemp, N. Taylor, and R. Wenninger, European demo design strategy and consequences for materials, Nuclear Fusion **57**, 092002 (2017).

[37] G. R. Terrell and D. W. Scott, Variable kernel density estimation, The Annals of Statistics , 1236 (1992).

[38] R. Behrisch and G. Venus, Heat removal by the divertor plate and limiter materials in fusion reactors, Journal of nuclear materials **202**, 1 (1993).

[39] R. Behrisch, Evaporation for heat pulses on ni, mo, w and atj graphite as first wall materials, Journal of Nuclear Materials **93**, 498 (1980).

[40] G. Federici, J. Brooks, D. Coster, G. Janeschitz, A. Kukushkin, A. Loarte, H. Pacher, J. Stober, and C. Wu, Assessment of erosion and tritium codeposition in iter-feat, Journal of nuclear materials **290**, 260 (2001).

[41] A. Raffray, J. Schlosser, M. Akiba, M. Araki, S. Chiocchio, D. Driemeyer, F. Escourbiac, S. Grigoriev, M. Merola, R. Tivey, *et al.*, Critical heat flux analysis and r&d for the design of the iter divertor, Fusion Engineering and Design **45**, 377 (1999).

[42] K. Lejaeghere, S. Cottenier, and V. Van Speybroeck, Ranking the stars: A refined pareto approach to computational materials design, Physical Review Letters **111**, 075501 (2013).

[43] K. D. Hammond, S. Blondel, L. Hu, D. Maroudas, and B. D. Wirth, Large-scale atomistic simulations of low-energy helium implantation into tungsten single crystals, Acta Materialia **144**, 561 (2018).

[44] P. Hatton, M. Hatton, D. Perez, and B. P. Uberuaga, The importance of long-timescale simulations for driven systems: An example of he bubble growth at a w gb, MRS Communications , 1 (2022).

[45] D. Dasgupta, R. D. Kolasinski, R. W. Friddle, L. Du, D. Maroudas, and B. D. Wirth, On the origin of ‘fuzz’ formation in plasma-facing materials, Nuclear Fusion **59**, 086057 (2019).

[46] M. W. Thompson, Physical mechanisms of sputtering, Physics Reports **69**, 335 (1981).

[47] A. Goehlich, N. Niemöller, and H. Döbele, Anisotropy effects in physical sputtering investigated by laser-induced fluorescence spectroscopy, Physical Review B **62**, 9349 (2000).

[48] X. Yang and A. Hassanein, Atomic scale calculations of tungsten surface binding energy and beryllium-induced tungsten sputtering, Applied surface science **293**, 187 (2014).

[49] L. Morrissey, O. Tucker, R. Killen, D. Herschback, and D. W. Savin, *Simulating Solar-Wind-Ion Sputtering of Sodium from Mercury’s Surface: The Importance of the Surface Binding Energy*, Tech. Rep. (Copernicus Meetings, 2021).

[50] M. Gyoeroek, A. Kaiser, I. Sukuba, J. Urban, K. Hermansson, and M. Probst, Surface binding energies of beryllium/tungsten alloys, Journal of Nuclear Materials **472**, 76 (2016).

[51] R. Tran, Z. Xu, B. Radhakrishnan, D. Winston, W. Sun, K. A. Persson, and S. P. Ong, Surface energies of elemental crystals, Scientific data **3**, 1 (2016).

[52] N. E. Singh-Miller and N. Marzari, Surface energies, work functions, and surface relaxations of low-index metallic surfaces from first principles, Physical Review B **80**, 235407 (2009).

[53] Home Page - Quantum Espresso (2022), [Online; accessed 30. Nov. 2022].

[54] P. Giannozzi, S. Baroni, N. Bonini, M. Calandra, R. Car, C. Cavazzoni, D. Ceresoli, G. L. Chiarotti, M. Cococcioni, I. Dabo, *et al.*, Quantum espresso: a modular and open-source software project for quantum simulations of materials, Journal of physics: Condensed matter **21**, 395502 (2009).

[55] Quantum ESPRESSO input generator (2022), [Online; accessed 22. Nov. 2022].

[56] G. Prandini, A. Marrazzo, I. E. Castelli, N. Mounet, and N. Marzari, Precision and efficiency in solid-state pseudopotential calculations, npj Computational Materials **4**, 1 (2018).

[57] K. F. Garrity, J. W. Bennett, K. M. Rabe, and D. Vanderbilt, Pseudopotentials for high-throughput dft calculations, Computational Materials Science **81**, 446 (2014).

[58] C. G. Van de Walle, Hydrogen as a cause of doping in zinc oxide, Physical review letters **85**, 1012 (2000).

[59] K. Reuter and M. Scheffler, Composition and structure of the ruo 2 (110) surface in an o 2 and co environment: Implications for the catalytic formation of co 2, Physical Review B **68**, 045407 (2003).

[60] S. Shao, M. J. Mahtabi, N. Shamsaei, and S. M. Thompson, Solubility of argon in laser additive manufactured α -titanium under hot isostatic pressing condition, Computational Materials Science **131**, 209 (2017).

[61] R. Kirchheim and A. Pundt, Hydrogen in metals physical metallurgy (2014).

[62] K. Wilson, R. Causey, W. Hsu, B. Mills, M. Smith, and J. Whitley, Beryllium—a better tokamak plasma-facing material?, Journal of Vacuum Science & Technology A: Vacuum, Surfaces, and Films **8**, 1750 (1990).

[63] W. M. Haynes, *CRC handbook of chemistry and physics* (CRC press, 2016).

[64] T. Hoshino, K. Kato, Y. Natori, F. Oikawa, N. Nakano, M. Nakamura, K. Sasaki, A. Suzuki, T. Terai, and K. Tatenuma, Development of advanced tritium breeding material with added lithium for iter-tbm, Journal of nuclear materials **417**, 684 (2011).

[65] J. D. Coburn, T. Gebhart, C. M. Parish, E. Unterberg, J. Canik, M. Barsoum, and M. Bourham, Surface erosion of plasma-facing materials using an electrothermal plasma source and ion beam micro-trenches, Fusion Science and Technology **75**, 621 (2019).

[66] H. Zhang, R. Su, L. Shi, and D. O’Connor, Helium irradiation tolerance of ti {sub 3} sic {sub 2} max phase material, Transactions of the American Nuclear Society **116** (2017).

[67] M. Barsoum, T. El-Raghy, C. Rawn, W. Porter, H. Wang, E. Payzant, and C. Hubbard, Thermal properties of ti3sic2, Journal of Physics and Chemistry of Solids **60**, 429 (1999).

[68] R. Taylor, K. Gilchrist, and L. Poston, Thermal conductivity of polycrystalline graphite, Carbon **6**, 537 (1968).

[69] G. Fugallo, A. Cepellotti, L. Paulatto, M. Lazzeri, N. Marzari, and F. Mauri, Thermal conductivity of graphene and graphite: collective excitations and mean free paths, *Nano letters* **14**, 6109 (2014).

[70] G. Matthews, P. Edwards, T. Hirai, M. Kear, A. Lioure, P. Lomas, A. Loving, C. Lungu, H. Maier, P. Mertens, *et al.*, Overview of the iter-like wall project, *Physica Scripta* **2007**, 137 (2007).

[71] J. Abrahamson, Graphite sublimation temperatures, carbon arcs and crystallite erosion, *Carbon* **12**, 111 (1974).

[72] B. Riccardi, P. Gavila, R. Giniatulin, V. Kuznetsov, R. Rulev, N. Klimov, D. Kovalenko, V. Barsuk, V. Koidan, and S. Korshunov, Effect of stationary high heat flux and transient elms-like heat loads on the divertor pfcs, *Fusion Engineering and Design* **88**, 1673 (2013).

[73] J. Roth, E. Vietzke, and A. Haasz, Erosion of graphite due to particle impact, *Atomic and Plasma-Material Interaction Data for Fusion* **1**, 63 (1991).

[74] J. Roth, E. Tsitrone, A. Loarte, T. Loarer, G. Counsell, R. Neu, V. Philipps, S. Brezinsek, M. Lehnchen, P. Coad, *et al.*, Recent analysis of key plasma wall interactions issues for iter, *Journal of nuclear materials* **390**, 1 (2009).

[75] T. Maruyama and M. Harayama, Neutron irradiation effect on the thermal conductivity and dimensional change of graphite materials, *Journal of Nuclear Materials* **195**, 44 (1992).

[76] J. Bonal and C. Wu, Neutron irradiation effects on the thermal conductivity and dimensional stability of carbon fiber composites at divertor conditions, *Journal of nuclear materials* **228**, 155 (1996).

[77] L. L. Snead and M. Ferraris, 6.03 - graphite and carbon fiber composite for fusion, in *Comprehensive Nuclear Materials (Second Edition)*, edited by R. J. Konings and R. E. Stoller (Elsevier, Oxford, 2020) second edition ed., pp. 54–92.

[78] G. De Temmerman, J. Dodson, J. Linke, S. Lisgo, G. Pintsuk, S. Porro, and G. Scarsbrook, Thermal shock resistance of thick boron-doped diamond under extreme heat loads, *Nuclear Fusion* **51**, 052001 (2011).

[79] D. Hughes, J. Penrose, C. Corr, S. Harmer, and J. Quinton, Degradation of fusion reactor plasma-facing materials through surface plasma etching, in *Proceedings of the 1st Corrosion and Materials Degradation Web Conference*, edited by R. J. Raman Singh Monash, Digby Macdonald (MDPI, 2021).

[80] S. Kato, M. Watanabe, H. Toyoda, and H. Sugai, Laboratory experiment on lithium chemistry and its application to effective wall conditioning, *Journal of nuclear materials* **266**, 406 (1999).

[81] C. Garcia-Rosales and J. Roth, Chemical sputtering of pyrolytic graphite and boron doped graphite usb15 at energies between 10 and 1000 ev, *Journal of nuclear materials* **196**, 573 (1992).

[82] G. De Temmerman, R. Doerner, P. John, S. Lisgo, A. Litnovsky, L. Marot, S. Porro, P. Petersson, M. Rubel, D. Rudakov, *et al.*, Interactions of diamond surfaces with fusion relevant plasmas, *Physica Scripta* **2009**, 014013 (2009).

[83] L. Begrambekov, O. Buzhinskij, B. Y. Kokushkin, M. Nikolskij, V. Otroshchenko, A. Pustobaev, L. Razumov, V. Tel'kovskij, Y. V. Fedorov, and I. Shlenov, Development of cc composites with low coefficients of sputtering by ions at high temperatures, *Journal of Nuclear Materials*, on Metallurgy, Ceramics and Solid State Physics in the Nuclear Energy Industry;(Netherlands) **170** (1990).

[84] J. Roth, E. Tsitrone, T. Loarer, V. Philipps, S. Brezinsek, A. Loarte, G. F. Counsell, R. P. Doerner, K. Schmid, O. V. Ogorodnikova, *et al.*, Tritium inventory in iter plasma-facing materials and tritium removal procedures, *Plasma Physics and Controlled Fusion* **50**, 103001 (2008).

[85] T. Mori and T. Tanaka, Effect of transition metal doping and carbon doping on thermoelectric properties of yb66 single crystals, *Journal of Solid State Chemistry* **179**, 2889 (2006).

[86] V. Novikov, D. Avdashchenko, N. Mitroshenkov, A. Matovnikov, and S. L. Bud'ko, Thermal expansion and lattice dynamics of rb 66 compounds at low temperatures, *Physics of the Solid State* **56**, 2069 (2014).

[87] V. Adasch, M. Schroeder, D. Kotzott, T. Ludwig, N. Voiteer, and H. Hillebrecht, Synthesis, crystal structure, and properties of mgxb50c8 or mgx(b12)4(cbc)2(c2)2 (x = 2.4-4), *Journal of the American Chemical Society* **132**, 13723 (2010), pMID: 20839790.

[88] Z. Qu, C. Yu, Y. Wei, X. Su, and A. Du, Thermal conductivity of boron carbide under fast neutron irradiation, *Journal of Advanced Ceramics* **11**, 482 (2022).

[89] Y. Morohashi, T. Maruyama, T. Donomae, Y. Tachi, and S. Onose, Neutron irradiation effect on isotopically tailored 11b4c, *Journal of nuclear science and technology* **45**, 867 (2008).

[90] O. Buzhinskij, I. Opimach, V. Barsuk, V. Otroshchenko, A. Zhitlukhin, A. Trazhenkov, W. West, P. Trester, P. Valentine, R. Watson, *et al.*, Performance of boron containing materials under disruption simulations and tokamak divertor plasma testing, *Journal of nuclear materials* **220**, 922 (1995).

[91] E. Grinik, V. Ogorodnikov, and A. Krainy, Fracturing of borides under neutron irradiation, *Journal of nuclear materials* **233**, 1349 (1996).

[92] A. Bhattacharya, C. M. Parish, T. Koyanagi, C. M. Petrie, D. King, G. Hilmas, W. G. Fahrenholtz, S. J. Zinkle, and Y. Katoh, Nano-scale microstructure damage by neutron irradiations in a novel boron-11 enriched tib2 ultra-high temperature ceramic, *Acta Materialia* **165**, 26 (2019).

[93] T. Koyanagi, Y. Katoh, C. Ang, D. King, G. E. Hilmas, and W. G. Fahrenholtz, Response of isotopically tailored titanium diboride to neutron irradiation, *Journal of the American Ceramic Society* **102**, 85 (2019).

[94] M. Wirtz, J. Linke, T. Loewenhoff, G. Pintsuk, and I. Uytdehouwen, Transient heat load challenges for plasma-facing materials during long-term operation, *Nuclear Materials and Energy* **12**, 148 (2017).

[95] G. Pintsuk, I. Bobin-Vastra, S. Constans, P. Gavila, M. Rödig, and B. Riccardi, Qualification and post-mortem characterization of tungsten mock-ups exposed to cyclic high heat flux loading, *Fusion Engineering and Design* **88**, 1858 (2013).

[96] M. Li and J.-H. You, Interpretation of the deep cracking phenomenon of tungsten monoblock targets observed in high-heat-flux fatigue tests at 20 mw/m², *Fusion Engineering and Design* **101**, 1 (2015).

[97] A. Suslova, O. El-Atwani, D. Sagapuram, S. Harilal, and A. Hassanein, Recrystallization and grain growth induced by elms-like transient heat loads in deformed

tungsten samples, *Scientific reports* **4**, 1 (2014).

[98] N. Klimov, V. Podkorytov, D. Kovalenko, A. Zhitlukhin, V. Barsuk, I. Mazul, R. Giniyatulin, V. Y. Kuznetsov, B. Riccardi, A. Loarte, *et al.*, Experimental study of divertor plasma-facing components damage under a combination of pulsed and quasi-stationary heat loads relevant to expected transient events at iter, *Physica Scripta* **2011**, 014064 (2011).

[99] V. Makhraj, I. Garkusha, N. Aksenov, A. Chuvilo, V. Chebotarev, I. Landman, S. Malykhin, S. Pestchanyi, and A. Pugachov, Dust generation mechanisms under powerful plasma impacts to the tungsten surfaces in iter elm simulation experiments, *Journal of Nuclear Materials* **438**, S233 (2013).

[100] A. Kreter, D. Nishijima, R. Doerner, M. Freisinger, C. Linsmeier, Y. Martynova, S. Möller, M. Rasinski, M. Reinhart, A. Terra, *et al.*, Influence of plasma impurities on the fuel retention in tungsten, *Nuclear fusion* **59**, 086029 (2019).

[101] W. Eckstein, C. Garcia-Rosales, J. Roth, and W. Ottenberger, *Sputtering data* (Max-Planck-Institut für Plasmaphysik, 1993).

[102] A. Lasa, C. Björkas, K. Vörtler, and K. Nordlund, Md simulations of low energy deuterium irradiation on w, wc and w₂c surfaces, *Journal of nuclear materials* **429**, 284 (2012).

[103] G. De Temmerman, K. Bystrov, R. Doerner, L. Marot, G. Wright, K. Woller, D. Whyte, and J. Zielinski, Helium effects on tungsten under fusion-relevant plasma loading conditions, *journal of Nuclear Materials* **438**, S78 (2013).

[104] J. A. Wright, A review of late-stage tungsten fuzz growth, *Tungsten* , 1 (2022).

[105] G. Sinclair, J. Tripathi, and A. Hassanein, Erosion dynamics of tungsten fuzz during elm-like heat loading, *Journal of Applied Physics* **123**, 133302 (2018).

[106] D. Hwangbo, S. Kawaguchi, S. Kajita, and N. Ohno, Erosion of nanostructured tungsten by laser ablation, sputtering and arcing, *Nuclear Materials and Energy* **12**, 386 (2017).

[107] A. Poskakalov, Y. M. Gasparyan, V. Efimov, D. Kovalenko, V. Barsuk, N. Klimov, M. Zibrov, and O. Ogorodnikova, Influence of plasma heat loads relevant to iter transient events on deuterium retention in tungsten, *Physica Scripta* **2020**, 014062 (2020).

[108] H. Iwakiri, K. Morishita, and N. Yoshida, Effects of helium bombardment on the deuterium behavior in tungsten, *Journal of nuclear materials* **307**, 135 (2002).

[109] E. Hodille, E. Bernard, S. Markelj, J. Mougenot, C. Bequaert, R. Bisson, and C. Grisolia, Estimation of the tritium retention in iter tungsten divertor target using macroscopic rate equations simulations, *Physica Scripta* **2017**, 014033 (2017).

[110] T. Toyama, K. Ami, K. Inoue, Y. Nagai, K. Sato, Q. Xu, and Y. Hatano, Deuterium trapping at vacancy clusters in electron/neutron-irradiated tungsten studied by positron annihilation spectroscopy, *Journal of Nuclear Materials* **499**, 464 (2018).

[111] X. Hu, T. Koyanagi, M. Fukuda, N. K. Kumar, L. L. Snead, B. D. Wirth, and Y. Katoh, Irradiation hardening of pure tungsten exposed to neutron irradiation, *Journal of Nuclear Materials* **480**, 235 (2016).

[112] S. Cui, R. P. Doerner, M. J. Simmonds, C. Xu, Y. Wang, E. Dechaumphai, E. Fu, G. R. Tynan, and R. Chen, Thermal conductivity degradation and recovery in ion beam damaged tungsten at different temperature, *Journal of Nuclear Materials* **511**, 141 (2018).

[113] G. Cottrell, Sigma phase formation in irradiated tungsten, tantalum and molybdenum in a fusion power plant, *Journal of nuclear materials* **334**, 166 (2004).

[114] H. Bolt, V. Barabash, G. Federici, J. Linke, A. Loarte, J. Roth, and K. Sato, Plasma facing and high heat flux materials-needs for iter and beyond, *Journal of Nuclear Materials* **307**, 43 (2002).

[115] D. Stork, P. Agostini, J.-L. Boutard, D. Buckthorpe, E. Diegele, S. Dudarev, C. English, G. Federici, M. Gilbert, S. Gonzalez, *et al.*, Developing structural, high-heat flux and plasma facing materials for a near-term demo fusion power plant: the eu assessment, *Journal of nuclear materials* **455**, 277 (2014).

[116] M. Fujitsuka, B. Tsuchiya, I. Mutoh, T. Tanabe, and T. Shikama, Effect of neutron irradiation on thermal diffusivity of tungsten-rhenium alloys, *Journal of nuclear materials* **283**, 1148 (2000).

[117] T. Tanabe, C. Eamchotchawalit, C. Busabok, S. Taweethavorn, M. Fujitsuka, and T. Shikama, Temperature dependence of thermal conductivity in w and w-re alloys from 300 to 1000 k, *Materials Letters* **57**, 2950 (2003).

[118] J. Brooks, J. Allain, D. Whyte, R. Ochoukov, and B. Lipschultz, Analysis of c-mod molybdenum divertor erosion and code/data comparison, *Journal of nuclear materials* **415**, S112 (2011).

[119] J. Sharpe, R. Kolasinski, M. Shimada, P. Calderoni, and R. Causey, Retention behavior in tungsten and molybdenum exposed to high fluences of deuterium ions in tpe, *Journal of nuclear materials* **390**, 709 (2009).

[120] N. Rasor and J. McClelland, Thermal properties of graphite, molybdenum and tantalum to their destruction temperatures, *Journal of Physics and Chemistry of Solids* **15**, 17 (1960).

[121] X. Yi, L. Zhang, W. Han, J. Chen, P. Liu, Y. Lv, J. Song, L. Xue, D. Geng, K. Yoshida, *et al.*, Defect characterization, mechanical and thermal property evaluation in cvd-w after low-dose neutron irradiation, *International Journal of Refractory Metals and Hard Materials* **85**, 105004 (2019).

[122] G. De Temmerman, K. Bystrov, J. J. Zielinski, M. Balden, G. Matern, C. Arnas, and L. Marot, Nanosstructuring of molybdenum and tungsten surfaces by low-energy helium ions, *Journal of Vacuum Science & Technology A: Vacuum, Surfaces, and Films* **30**, 041306 (2012).

[123] J. Tripathi, T. Novakowski, G. Joseph, J. Linke, and A. Hassanein, Temperature dependent surface modification of molybdenum due to low energy he+ ion irradiation, *Journal of Nuclear Materials* **464**, 97 (2015).

[124] R. Montanari, E. Pakhomova, R. Rossi, M. Richetta, and A. Varone, Surface morphological features of molybdenum irradiated by a single laser pulse, *Coatings* **10**, 67 (2020).

[125] G. Sinclair, J. Tripathi, P. Diwakar, and A. Hassanein, Melt layer erosion during elm-like heat loading on molybdenum as an alternative plasma-facing material, *Scientific Reports* **7**, 1 (2017).

[126] G. Sinclair, J. Tripathi, P. Diwakar, and A. Hassanein, Structural response of transient heat loading on a molybdenum surface exposed to low-energy helium ion irradiation, *Nuclear Fusion* **56**, 036005 (2016).

[127] G. Mazzitelli, M. Apicella, M. Iafrati, G. Apruzzese, F. Bombarda, F. Crescenzi, L. Gabellieri, A. Mancini, M. Marinucci, A. Romano, *et al.*, Experiments on the frascati tokamak upgrade with a liquid tin limiter, *Nuclear Fusion* **59**, 096004 (2019).

[128] J. Winter, P. Wienhold, H. Esser, L. Koenen, U. Samm, U. Littmark, E. Kny, and W. Grasserbauer, Test of a carbonized molybdenum limiter in textor, in *Europhysics Conference Abstracts*, Vol. 15 (1991) pp. III-173.

[129] A. Kallenbach, R. Neu, R. Dux, H. Fahrbach, J. Fuchs, L. Giannone, O. Gruber, A. Herrmann, P. Lang, B. Lipschultz, *et al.*, Tokamak operation with high-z plasma facing components, *Plasma physics and controlled fusion* **47**, B207 (2005).

[130] M. Li, E. Werner, and J.-H. You, Low cycle fatigue behavior of iter-like divertor target under demo-relevant operation conditions, *Fusion Engineering and Design* **90**, 88 (2015).

[131] S. J. Zinkle, Applicability of copper alloys for demo high heat flux components, *Physica Scripta* **2016**, 014004 (2015).

[132] X. Zhang, Y. Yuan, S. Zhao, J. Zhang, and Q. Yan, Microstructure stability, softening temperature and strengthening mechanism of pure copper, cu-cr-zr and cu-al2o3 up to 1000°C, *Nuclear Materials and Energy* **30**, 101123 (2022).

[133] G. Bondarenko, Y. Y. Udris, and V. Yakushin, On behaviour of w-cu composition as a candidate divertor material under irradiation by high intensive hydrogen plasma, *Fusion engineering and design* **51**, 81 (2000).

[134] P. Nath and K. Chopra, Thermal conductivity of copper films, *Thin Solid Films* **20**, 53 (1974).

[135] S. Zinkle and S. Fabritsiev, Copper alloys for high heat flux structure applications, *Atomic and Plasma-Material Interaction Data for Fusion (supplement to Nuclear Fusion)* **5**, 163 (1994).

[136] S. Fabritsiev and A. Pokrovsky, Effect of high doses of neutron irradiation on physico-mechanical properties of copper alloys for iter applications, *Fusion engineering and design* **73**, 19 (2005).

[137] S. H. Lee, S. Y. Kwon, and H. J. Ham, Thermal conductivity of tungsten-copper composites, *Thermochimica acta* **542**, 2 (2012).

[138] A. Krauss, D. Gruen, J. Brooks, M. Mendelsohn, R. Mattas, and A. DeWald, Self-sustaining coatings for fusion applications-copper lithium alloys, *Fusion Technology* **8**, 1269 (1985).

[139] A. Krauss, M. Mendelsohn, D. Gruen, R. Conn, D. Goebel, Y. Hirooka, W. Leung, and J. Bohdansky, Temperature and composition dependence of the high flux plasma sputtering yield of cu-li binary alloys, *Nuclear Instruments and Methods in Physics Research Section B: Beam Interactions with Materials and Atoms* **23**, 511 (1987).

[140] R. Schorn, E. Hintz, B. Baretzky, J. Bohdansky, W. Eckstein, J. Roth, and E. Taglauer, The suitability of copper/lithium alloys for application as wall material in tokamaks, *Journal of Nuclear Materials* **162**, 924 (1989).

[141] Wikipedia, Prices of chemical elements (2023), [Online; accessed 17. Apr. 2023].

[142] P. J. Fink, J. L. Miller, and D. G. Konitzer, Rhenium reduction—alloy design using an economically strategic element, *Jom* **62**, 55 (2010).

[143] L. Shen, F. Tesfaye, X. Li, D. Lindberg, and P. Taskinen, Review of rhenium extraction and recycling technologies from primary and secondary resources, *Minerals Engineering* **161**, 106719 (2021).

[144] T. Hirai, M. Rubel, V. Philipps, A. Huber, T. Tanabe, M. Wada, T. Ohgo, A. Pospieszczyk, G. Sergienko, and P. Wienhold, Testing of tungsten and tantalum limiters at the textor tokamak: material performance and deuterium retention, *Physica Scripta* **2003**, 59 (2003).

[145] I. Takagi, S. Nagaoka, K. Shirai, K. Moritani, and H. Moriyama, Trapping of hydrogen in tantalum bombarded with helium-3 ions, *Physica Scripta* **2003**, 121 (2003).

[146] T. Novakowski, J. Tripathi, and A. Hassanein, Effect of high-flux, low-energy he+ ion irradiation on ta as a plasma-facing material, *Scientific Reports* **6**, 1 (2016).

[147] D. Terentyev, T. Khvan, J.-H. You, and N. Van Steenberge, Development of chromium and chromium-tungsten alloy for the plasma facing components: Application of vacuum arc melting techniques, *Journal of Nuclear Materials* **536**, 152204 (2020).

[148] R. W. Cahn, *Binary alloy phase diagrams*—second edition. tb massalski, editor-in-chief; h. okamoto, pr subramanian, l. kacprzak, editors. asm international, materials park, ohio, usa. december 1990. xxii, 3589 pp., 3 vol., (1991).

[149] H. Okamoto, T. Massalski, *et al.*, *Binary alloy phase diagrams* (ASM International, Materials Park, OH, USA, 1990).

[150] M. Dias, R. Mateus, N. Catarino, N. Franco, D. Nunes, J. B. Correia, P. A. Carvalho, K. Hanada, C. Sârbu, and E. Alves, Synergistic helium and deuterium blistering in tungsten-tantalum composites, *Journal of nuclear materials* **442**, 69 (2013).

[151] M. Dias, N. Catarino, D. Nunes, E. Fortunato, I. Nogueira, M. Rosinki, J. Correia, P. Carvalho, and E. Alves, Helium and deuterium irradiation effects in w-ta composites produced by pulse plasma compaction, *Journal of Nuclear Materials* **492**, 105 (2017).

[152] S. L. K. Konuru, A. Sarma, *et al.*, Deposition of tungsten-tantalum composite coating on rafm steel by sputtering deposition process, *Fusion Engineering and Design* **160**, 111972 (2020).

[153] O. El-Atwani, N. Li, M. Li, A. Devaraj, J. Baldwin, M. M. Schneider, D. Sobieraj, J. S. Wróbel, D. Nguyen-Manh, S. A. Maloy, *et al.*, Outstanding radiation resistance of tungsten-based high-entropy alloys, *Science advances* **5**, eaav2002 (2019).

[154] X. Wang, H. Huang, J. Shi, H.-Y. Xu, and D.-Q. Meng, Recent progress of tungsten-based high-entropy alloys in nuclear fusion, *Tungsten* **3**, 143 (2021).

[155] J. Cui, Z. Cheng, D. Chen, T. Wang, L. Zhang, and J. Sun, Studies on the design and properties of fecrvtx medium-entropy alloys for potential nuclear applications, *Journal of Alloys and Compounds* **894**, 162398 (2022).

[156] P. Turchi, A. Gonis, V. Drchal, and J. Kudrnovský, First-principles study of stability and local order in substitutional ta-w alloys, *Physical Review B* **64**, 085112

(2001).

[157] W. Fahrenholtz and G. Hilmas, Oxidation of ultra-high temperature transition metal diboride ceramics, International Materials Reviews **57**, 61 (2012).

[158] W. G. Fahrenholtz, G. E. Hilmas, I. G. Talmy, and J. A. Zaykoski, Refractory diborides of zirconium and hafnium, Journal of the American Ceramic Society **90**, 1347 (2007).

[159] L. M. Garrison, G. L. Kulcinski, G. Hilmas, W. Fahrenholtz, and H. M. Meyer III, The response of zrb2 to simulated plasma-facing material conditions of he irradiation at high temperature, Journal of Nuclear Materials **507**, 112 (2018).

[160] M. Kaminsky, S. Lam, and K. Moy, Sputtering of tib2 coatings under d+ and 4he+ ion bombardment, Thin Solid Films **73**, 91 (1980).

[161] T. Nenadović, B. Gaković, B. Todorović, and T. Jokić, Sputtering yield and morphological changes of tib2 coatings induced by different incident beams, Nuclear Instruments and Methods in Physics Research Section B: Beam Interactions with Materials and Atoms **115**, 523 (1996).

[162] M. M. Nasseri, The behavior of hfb2 at neutron irradiation: a simulation study, Radiation Effects and Defects in Solids **171**, 252 (2016).

[163] C. Oses, C. Toher, and S. Curtarolo, High-entropy ceramics, Nature Reviews Materials **5**, 295 (2020).

[164] Y. Wu, W. Bao, X.-Q. Shen, J.-X. Liu, Y. Qin, Y. Liang, F. Xu, and G.-J. Zhang, Zrb2-based solid solution ceramics and their mechanical and thermal properties, International Journal of Applied Ceramic Technology **20**, 790 (2023).

[165] T. Tanabe, T. Baba, A. Ono, M. Fujitsuka, T. Shikama, and H. Shinno, Thermal properties of carbon-boron-titanium compounds as plasma facing materials, Journal of nuclear materials **191**, 382 (1992).

[166] Y. Wang and Q. Yan, Microstructure and strengthening mechanism of grain boundary strengthened w-zrb2 alloy, Journal of Materials Research and Technology **9**, 4007 (2020).

[167] O. H. Krikorian, *Estimation of heat capacities and other thermodynamic properties of refractory borides*, Tech. Rep. (California Univ., 1971).

[168] Y. Cao, T. Li, Y. Xu, P. Wang, J. Liu, D. Zhang, J. Duan, and S. Zhou, Theoretical predictions of stability, electronic properties, elastic anisotropy, thermodynamics, and optical properties of mb2 (m= v, nb, zr), Journal of Materials Science **57**, 4605 (2022).

[169] A. Pontau and K. Wilson, Vb2: A thin film coating on vanadium for reduced tritium inventory in controlled fusion devices, Thin Solid Films **73**, 109 (1980).

[170] B. Doyle, D. Brice, and W. Wampler, Hydrogen in fusion first wall surfaces, IEEE Transactions On Nuclear Science **28**, 1299 (1981).

[171] C. Wang, S. Akbar, W. Chen, and V. Patton, Electrical properties of high-temperature oxides, borides, carbides, and nitrides, Journal of materials science **30**, 1627 (1995).

[172] E. Wuchina, M. Opeka, S. Causey, K. Buesking, J. Spain, A. Cull, J. Routbort, and F. Guitierrez-Mora, Designing for ultrahigh-temperature applications: the mechanical and thermal properties of hfb 2, hfc x, hfn x and αhf (n), Journal of Materials Science **39**, 5939 (2004).

[173] Z. Cheng, J. Liang, K. Kawamura, H. Zhou, H. Asamura, H. Uratani, J. Tiwari, S. Graham, Y. Ohno, Y. Nagai, *et al.*, High thermal conductivity in wafer-scale cubic silicon carbide crystals, Nature Communications **13**, 7201 (2022).

[174] B. Yang, Q. Deng, Y. Su, X. Peng, C. Huang, A. Lee, and N. Hu, The effects of atomic arrangements on mechanical properties of 2h, 3c, 4h and 6h-sic, Computational Materials Science **203**, 111114 (2022).

[175] P. Rocco and M. Zucchetti, Criteria for defining low activation materials in fusion reactor applications, Fusion engineering and design **15**, 235 (1991).

[176] T. Abrams, S. Bringuer, D. M. Thomas, G. Sinclair, S. Gonderman, L. Holland, D. L. Rudakov, R. S. Wilcox, E. A. Unterberg, and F. Scotti, Evaluation of silicon carbide as a divertor armor material in diii-d h-mode discharges, Nuclear Fusion **61**, 066005 (2021).

[177] S. Abe, C. Skinner, A. Liu, J. Garcia, Z. Lin, S. Bringuer, T. Abrams, and B. Koel, Computational investigation of incident ion angles and material erosion at rough graphite and silicon carbide divertor surfaces, Physics of Plasmas **29**, 102503 (2022).

[178] R. A. Causey and W. R. Wampler, The use of silicon carbide as a tritium permeation barrier, Journal of Nuclear materials **220**, 823 (1995).

[179] R. A. Causey, Sputtering and codeposition of silicon carbide with deuterium, Journal of nuclear materials **313**, 450 (2003).

[180] N. H. Protik, A. Katre, L. Lindsay, J. Carrete, N. Mingo, and D. Broido, Phonon thermal transport in 2h, 4h and 6h silicon carbide from first principles, Materials Today Physics **1**, 31 (2017).

[181] T. Wang, Z. Gui, A. Janotti, C. Ni, and P. Karandikar, Strong effect of electron-phonon interaction on the lattice thermal conductivity in 3c-sic, Physical Review Materials **1**, 034601 (2017).

[182] R. Price, Thermal conductivity of neutron-irradiated pyrolytic β-silicon carbide, Journal of Nuclear Materials **46**, 268 (1973).

[183] Y. Katoh, T. Nozawa, L. L. Snead, K. Ozawa, and H. Tanigawa, Stability of sic and its composites at high neutron fluence, Journal of Nuclear Materials **417**, 400 (2011).

[184] Y. Katoh, L. L. Snead, C. H. Henager Jr, A. Hasegawa, A. Kohyama, B. Riccardi, and H. Hegeman, Current status and critical issues for development of sic composites for fusion applications, Journal of Nuclear Materials **367**, 659 (2007).

[185] L. Snead, T. Nozawa, M. Ferraris, Y. Katoh, R. Shinnavski, and M. Sawan, Silicon carbide composites as fusion power reactor structural materials, Journal of Nuclear Materials **417**, 330 (2011).

[186] Y. Katoh, K. Ozawa, C. Shih, T. Nozawa, R. J. Shinnavski, A. Hasegawa, and L. L. Snead, Continuous sic fiber, cvi sic matrix composites for nuclear applications: Properties and irradiation effects, Journal of Nuclear Materials **448**, 448 (2014).

[187] X.-Y. Tan, L.-M. Luo, Z.-L. Lu, G.-N. Luo, X. Zan, J.-G. Cheng, and Y.-C. Wu, Development of tungsten as plasma-facing materials by doping tantalum carbide nanoparticles, Powder Technology **269**, 437 (2015).

[188] F. Feng, Y. Lian, X. Liu, J. Wang, and Y. Xu, Effect of high-energy-rate forging on microstructure and properties of w-tac alloys, IEEE Transactions on Plasma Sciences **42**, 1000 (2014).

ence **46**, 2314 (2018).

[189] Y. Wang, S. Miao, Z. Xie, R. Liu, T. Zhang, Q. Fang, T. Hao, X. Wang, C. Liu, X. Liu, *et al.*, Thermal stability and mechanical properties of hfc dispersion strengthened w alloys as plasma-facing components in fusion devices, *Journal of Nuclear Materials* **492**, 260 (2017).

[190] M. Zibrov, K. Bystrov, M. Mayer, T. W. Morgan, and H. Kurishita, The high-flux effect on deuterium retention in tic and tac doped tungsten at high temperatures, *Journal of Nuclear Materials* **494**, 211 (2017).

[191] R. Andrievskii, N. Strel'nikova, N. Poltoratskii, E. Kharkhardin, and V. Smirnov, Melting point in systems zrc-hfc, tac-zrc, tac-hfc, *Soviet Powder Metallurgy and Metal Ceramics* **6**, 65 (1967).

[192] O. Cedillos-Barraza, D. Manara, K. Boboridis, T. Watkins, S. Grasso, D. D. Jayaseelan, R. J. Konings, M. J. Reece, and W. E. Lee, Investigating the highest melting temperature materials: A laser melting study of the tac-hfc system, *Scientific reports* **6**, 1 (2016).

[193] O. Cedillos-Barraza, S. Grasso, N. Al Nasiri, D. D. Jayaseelan, M. J. Reece, and W. E. Lee, Sintering behaviour, solid solution formation and characterisation of tac, hfc and tac-hfc fabricated by spark plasma sintering, *Journal of the European Ceramic Society* **36**, 1539 (2016).

[194] W. Li, E. A. Olevsky, O. L. Khasanov, C. A. Back, O. Izhvanov, J. Opperman, and H. E. Khalifa, Spark plasma sintering of agglomerated vanadium carbide powder, *Ceramics International* **41**, 3748 (2015).

[195] Y. Liu, S. Huang, J. Ding, Y. Yang, and J. Zhao, Vanadium carbide coating as hydrogen permeation barrier: A dft study, *International Journal of Hydrogen Energy* **44**, 6093 (2019).

[196] S. Huang, J. Tian, and Y. Liu, Atomic study of hydrogen behavior in different vanadium carbides, *Journal of Nuclear Materials* **554**, 153096 (2021).

[197] H. Takahashi, S. Ohnuki, H. Kinoshita, R. Nagasaki, and K. Abe, The effects of damage structures on mechanical properties of neutron irradiated vanadium, *Journal of Nuclear Materials* **155**, 982 (1988).

[198] H. Matsui, K. Nesaki, and M. Kiritani, Neutron irradiation damage in transition metal carbides, *Journal of nuclear materials* **179**, 461 (1991).

[199] Z. Yan, Y. Huang, Y. Wu, L. Luo, L. A. Saul, and G. Yao, Microstructural effects of y 2 o 3 and tic additions in tungsten, *Journal of Fusion Energy* **40**, 1 (2021).

[200] J. Matějíček and P. Chráska, Development of advanced coatings for iter and future fusion devices, *Advances in Science and Technology* **66**, 47 (2011).

[201] K. Cunningham, G. Odette, K. Fields, D. Gragg, F. Zok, and C. Henager, Recent progress in the fabrication and characterization of ductile-phase-toughened tungsten composites for plasma-facing materials, *Fusion Reactor Materials Program* **56** (2014).

[202] A. Šestan, L. Sreekala, S. Markelj, M. Kelemen, J. Zavašník, C. H. Liebscher, G. Dehm, T. Hickel, M. Čeh, S. Novak, *et al.*, Non-uniform he bubble formation in w/w2c composite: Experimental and ab-initio study, *Acta Materialia* **226**, 117608 (2022).

[203] P. Träskelin, C. Björkas, N. Juslin, K. Vörtler, and K. Nordlund, Radiation damage in wc studied with md simulations, *Nuclear Instruments and Methods in Physics Research Section B: Beam Interactions with Materials and Atoms* **257**, 614 (2007).

[204] S. A. Humphry-Baker and G. D. Smith, Shielding materials in the compact spherical tokamak, *Philosophical Transactions of the Royal Society A* **377**, 20170443 (2019).

[205] T. Dash, B. Nayak, M. Abhangi, R. Makwana, S. Vala, S. Jakhar, C. Rao, and T. Basu, Preparation and neutronic studies of tungsten carbide composite, *Fusion Science and Technology* **65**, 241 (2014).

[206] K. Gavrichev, V. Solozhenko, V. Gorbunov, L. Golushina, G. Totrova, and V. Lazarev, Low-temperature heat capacity and thermodynamic properties of four boron nitride modifications, *Thermochimica acta* **217**, 77 (1993).

[207] P. Chakraborty, G. Xiong, L. Cao, and Y. Wang, Lattice thermal transport in superhard hexagonal diamond and wurtzite boron nitride: A comparative study with cubic diamond and cubic boron nitride, *Carbon* **139**, 85 (2018).

[208] K. Chen, B. Song, N. K. Ravichandran, Q. Zheng, X. Chen, H. Lee, H. Sun, S. Li, G. A. G. Udalammata Gamage, F. Tian, *et al.*, Ultrahigh thermal conductivity in isotope-enriched cubic boron nitride, *Science* **367**, 555 (2020).

[209] C. Yuan, J. Li, L. Lindsay, D. Cherns, J. W. Pomeroy, S. Liu, J. H. Edgar, and M. Kuball, Modulating the thermal conductivity in hexagonal boron nitride via controlled boron isotope concentration, *Communications physics* **2**, 43 (2019).

[210] F. Corrigan, Thermal conductivity of polycrystalline cubic boron nitride compacts, *High-Pressure Science and Technology: Volume 1: Physical Properties and Material Synthesis/Volume 2: Applications and Mechanical Properties*, 994 (1979).

[211] E. Sichel, R. Miller, M. Abrahams, and C. Buiocchi, Heat capacity and thermal conductivity of hexagonal pyrolytic boron nitride, *Physical review B* **13**, 4607 (1976).

[212] L. Duclaux, B. Nysten, J.-P. Issi, and A. Moore, Structure and low-temperature thermal conductivity of pyrolytic boron nitride, *Physical Review B* **46**, 3362 (1992).

[213] O. Buzhinskij, V. Lopatin, and B. Sharupin, Rhombohedral pyrolytic boron nitride as a protection material in fusion devices, *Journal of nuclear materials* **196**, 1118 (1992).

[214] F. Cataldo and S. Iglesias-Groth, Neutron damage of hexagonal boron nitride: h-bn, *Journal of radioanalytical and nuclear chemistry* **313**, 261 (2017).

[215] O. Buzhinskij, I. Opimach, A. Kabishev, V. Lopatin, and Y. P. Surov, Application of pyrolytic boron nitride in fusion devices, *Journal of Nuclear Materials* **173**, 179 (1990).

[216] S. K. Bull, T. Champ, S. Raj, A. W. Weimer, and C. B. Musgrave, Ab initio screening of refractory nitrides and carbides for high temperature hydrogen permeation barriers, *Journal of Nuclear Materials* **563**, 153611 (2022).

[217] R. A. Causey, W. R. Wampler, and O. Buzhinskij, Tritium retention characteristics of several low-z materials, *Journal of nuclear materials* **196**, 977 (1992).

[218] A. Lale, S. Bernard, and U. B. Demirci, Boron nitride for hydrogen storage, *ChemPlusChem* **83**, 893 (2018).

[219] J. S. Kang, M. Li, H. Wu, H. Nguyen, and Y. Hu, Experimental observation of high thermal conductivity in boron arsenide, *Science* **361**, 575 (2018).

[220] J. Garg, N. Bonini, and N. Marzari, High thermal conductivity in short-period superlattices, *Nano letters* **11**, 5135 (2011).

[221] T. Chu and A. Hyslop, Preparation and properties of boron arsenide films, *Journal of The Electrochemical Society* **121**, 412 (1974).

[222] X. Luo, X. Guo, B. Xu, Q. Wu, Q. Hu, Z. Liu, J. He, D. Yu, Y. Tian, and H.-T. Wang, Body-centered superhard $b\bar{c}2n$ phases from first principles, *Physical Review B* **76**, 094103 (2007).

[223] L. Liu, Z. Zhao, T. Yu, S. Zhang, J. Lin, and G. Yang, Hexagonal $bc2n$ with remarkably high hardness, *The Journal of Physical Chemistry C* **122**, 6801 (2018).

[224] S. N. Sadeghi, S. M. V. Allaei, M. Zebarjadi, and K. Esfarjani, Ultra-high lattice thermal conductivity and the effect of pressure in superhard hexagonal $bc2n$, *Journal of Materials Chemistry C* **8**, 15705 (2020).

[225] X. Wang, Y. Wang, M. Zhang, and H. Liu, Superhard $bc2n$ in cubic diamondlike structure, *Physical Review B* **107**, 134101 (2023).

[226] S. Ju, R. Yoshida, C. Liu, S. Wu, K. Hongo, T. Tadano, and J. Shiomi, Exploring diamondlike lattice thermal conductivity crystals via feature-based transfer learning, *Physical Review Materials* **5**, 053801 (2021).

[227] J. Chang, Y. Cheng, and M. Fu, First-principles calculations of thermodynamic properties of superhard orthorhombic β - $bc2n$ elastic, *J. At. Mol. Sci* **1**, 243 (2010).

[228] S. Li, L. Shi, H. Zhu, and W. Xia, Elastic and bandgap modulations of hexagonal $bc2n$ from first-principles calculations, *physica status solidi (b)* **256**, 1900281 (2019).

[229] Y. Cheng, X. Wu, S. Li, and P. K. Chu, Ab initio determination of lattice dynamics and thermodynamics of β - $bc2n$, *Solid state communications* **146**, 69 (2008).

[230] G. G. Ross and D. Bourgoin, Improvement of carbon properties used as pfcs in tokamaks by nitrogen irradiation, in *AIP Conference Proceedings*, Vol. 669 (American Institute of Physics, 2003) pp. 248–252.

[231] H. Montigaud, B. Tanguy, G. Demazeau, I. Alves, and S. Courjault, C₃n4: Dream or reality? solvothermal synthesis as macroscopic samples of the c₃n4 graphitic form, *Journal of materials science* **35**, 2547 (2000).

[232] D. Morelli and J. Heremans, Thermal conductivity of germanium, silicon, and carbon nitrides, *Applied physics letters* **81**, 5126 (2002).

[233] D. T. Morelli and G. A. Slack, High lattice thermal conductivity solids, *High thermal conductivity materials* , 37 (2006).

[234] T. Zhu, S. Gong, T. Xie, P. Gorai, and J. C. Grossman, Charting lattice thermal conductivity of inorganic crystals, *arXiv preprint arXiv:2006.11712* (2020).

[235] L.-W. Ruan, G.-S. Xu, H.-Y. Chen, Y.-P. Yuan, X. Jiang, Y.-X. Lu, and Y.-J. Zhu, The elastic behavior of dense c₃n4 under high pressure: First-principles calculations, *Journal of Physics and Chemistry of Solids* **75**, 1324 (2014).

[236] M. N. Uddin and Y. S. Yang, Formation of nanocrystalline c₃n4 thin films on stainless steel from hexamethylenetetramine and urea using simple sol-gel method, *Thin solid films* **548**, 27 (2013).

[237] Š. Huber, O. Jankovský, D. Sedmidubský, J. Luxa, K. Klímová, J. Hejtmánek, and Z. Sofer, Synthesis, structure, thermal, transport and magnetic properties of vn ceramics, *Ceramics International* **42**, 18779 (2016).

[238] O. Ambacher, Growth and applications of group iii-nitrides, *Journal of physics D: Applied physics* **31**, 2653 (1998).

[239] M. Gonzalez and E. Hodgson, Radiation resistant bolometers using platinum on al₂o₃ and aln, *Fusion engineering and design* **74**, 875 (2005).

[240] A. Gusalov, S. Huysmans, L. Vermeeren, E. Hodgson, and M. Decréton, In situ in-reactor testing of potential bolometer materials for iter plasma diagnostics, *Fusion engineering and design* **82**, 1179 (2007).

[241] J. Wang, Q. Li, Q.-Y. Xiang, and J.-L. Cao, Performances of aln coatings as hydrogen isotopes permeation barriers, *Fusion Engineering and Design* **102**, 94 (2016).

[242] D. Cherkez, A. Spitsyn, A. Golubeva, O. Obrezkov, S. Ananyev, N. Bobyr, and V. Chernov, Deuterium permeation through reduced activation v-4cr-4ti alloy and v-4cr-4ti alloy with aln/al coatings, *Physics of Atomic Nuclei* **82**, 1010 (2019).

[243] M. Patino, R. Doerner, and G. Tynan, Exposure of aln and al₂o₃ to low energy d and he plasmas, *Nuclear Materials and Energy* **23**, 100753 (2020).

[244] T. Yano and T. Iseki, Thermal and mechanical properties of neutron-irradiated aluminum nitride, *Journal of nuclear materials* **179**, 387 (1991).

[245] L. Snead, S. Zinkle, and D. White, Thermal conductivity degradation of ceramic materials due to low temperature, low dose neutron irradiation, *Journal of nuclear materials* **340**, 187 (2005).

[246] K. Watari, T. Tsugoshi, T. Nagaoka, H. Nakano, K. Urabe, S. Cao, K. Mori, and K. Ishizaki, Microstructure and thermal conductivity of aln ceramic with eliminated grain boundary phase, *Key Engineering Materials* **247** (2003).

[247] a. S. Strite and H. Morkoç, Gan, aln, and inn: a review, *Journal of Vacuum Science & Technology B: Microelectronics and Nanometer Structures Processing, Measurement, and Phenomena* **10**, 1237 (1992).

[248] A. Kundu, X. Yang, J. Ma, T. Feng, J. Carrete, X. Ruan, G. K. Madsen, and W. Li, Ultrahigh thermal conductivity of θ -phase tantalum nitride, *Physical Review Letters* **126**, 115901 (2021).

[249] G. Glazunov, E. Volkov, V. Veremeyenko, N. Kosik, A. Kutsyn, J. Langner, E. Langner, Y. K. Mironov, N. Nazarov, J. Piekoszewski, *et al.*, Erosion and outgassing behavior of tin-coated plasma facing components of the uragan-3m torsatron, *Journal of nuclear materials* **290**, 266 (2001).

[250] S. Zhang, X. Huang, D. Zhao, Z. Hong, X. Zeng, and L. Cai, Fabrication and test of a conceptual first wall containing titanium nitride as a tritium permeation barrier, *Fusion Engineering and Design* **182**, 113244 (2022).

[251] M. Ghoranneviss, S. Meshkani, and A. Jafari, The study of plasma-tin interaction in tokamak, *Journal of Alloys and Compounds* **656**, 318 (2016).

[252] A. Wallner, K. Buczak, C. Lederer, H. Vonach, T. Faestermann, G. Korschinek, M. Poutivtsev, G. Rugel, A. Klix, K. Seidel, *et al.*, Production of long-lived radionuclides ^{10}be , ^{14}c , ^{53}mn , ^{55}fe , ^{59}ni and ^{202}gpb in a fusion environment, *J. Kor. Phys. Soc* **59**, 1378 (2011).

[253] B. N. Kolbasov, L. El-Guebaly, V. I. Khripunov, Y. Someya, K. Tobita, and M. Zucchetti, Some technological problems of fusion materials management, *Fusion Engineering and Design* **89**, 2013 (2014).

[254] T. Hirai, S. Carpentier-Chouchana, F. Escourbiac, S. Panayotis, A. Durocher, L. Ferrand, M. Garcia-Martinez, J. Gunn, V. Komarov, M. Merola, *et al.*, Design optimization of the iter tungsten divertor vertical targets, *Fusion Engineering and Design* **127**, 66 (2018).

[255] D. Fedoseev, S. Vnukov, V. Bukhovets, and B. Anikin, Surface graphitization of diamond at high temperatures, *Surface and Coatings Technology* **28**, 207 (1986).

[256] Y.-C. Ding, M. Chen, and W.-J. Wu, Theoretical calculations of stability, mechanical and thermodynamic properties of iva group willemite-ii nitrides, *Journal of Theoretical and Computational Chemistry* **14**, 1550024 (2015).

[257] V. Solozhenko, Thermodynamics of dense boron nitride modifications and a new phase p, t diagram for bn, *Thermochimica Acta* **218**, 221 (1993).

[258] G. K. White and S. Collocott, Heat capacity of reference materials: Cu and w, *Journal of physical and chemical reference data* **13**, 1251 (1984).

[259] G. Samsonov, A. Bolgar, E. Guseva, L. Klochkov, B. Kovenskaya, T. Serebryakova, I. Timofeeva, A. Turchanin, and V. Fesenko, *Thermophysical properties of transition metal carbides and diborides*, Tech. Rep. (AN Ukrainskoj SSR, Kiev. Inst. Problem Materialovedeniya, 1973).

[260] E. W. Neuman, M. Thompson, W. G. Fahrenholtz, and G. E. Hilmas, Thermal properties of zrb2-tib2 solid solutions, *Journal of the European Ceramic Society* **41**, 7434 (2021).

[261] G. Baysinger, L. I. Berger, R. Goldberg, H. Kehiaian, K. Kuchitsu, G. Rosenblatt, D. Roth, and D. Zwillinger, *Crc handbook of chemistry and physics*, National Institute of Standards and Technology (2015).

[262] H. Xiang, Z. Feng, Z. Li, and Y. Zhou, First-principles investigations on elevated temperature elastic and thermodynamic properties of zrb2 and hfb2, *Journal of the American Ceramic Society* **100**, 3662 (2017).

[263] Y. Liu, Q. Li, Y. Qian, Y. Yang, S. Wang, W. Li, and B. Sun, Thermal conductivity of high-temperature high-pressure synthesized θ -tan, *Applied Physics Letters* **122** (2023).

[264] H. Lee, Y. Zhou, S. Jung, H. Li, Z. Cheng, J. He, J. Chen, P. Sokalski, A. Dolocan, R. Gearba-Dolocan, *et al.*, High-pressure synthesis and thermal conductivity of semimetallic θ -tantalum nitride, *Advanced Functional Materials*, 2212957 (2023).

[265] T. Tabassum, *Correlating Thermal Properties Of Sputtered Tantalum And Tantalum Nitride Thin Films Of Varying N2 Content With Mechanical, Electrical And Structural Properties*, Ph.D. thesis, Cornell University (2017).

[266] R. Andon, J. Martin, K. Mills, and T. Jenkins, Heat capacity and entropy of tungsten carbide, *The Journal of Chemical Thermodynamics* **7**, 1079 (1975).

[267] I. Savchenko and S. Stankus, Thermal conductivity and thermal diffusivity of tantalum in the temperature range from 293 to 1800 k, *Thermophysics and Aeromechanics* **15**, 679 (2008).

[268] N. D. Milošević, G. Vuković, D. Pavićić, and K. Maglić, Thermal properties of tantalum between 300 and 2300 k, *International journal of thermophysics* **20**, 1129 (1999).

[269] R. Powell, R. Tye, and M. J. Woodman, The thermal conductivity and electrical resistivity of rhenium, *Journal of the Less Common Metals* **5**, 49 (1963).

[270] R. Taylor and R. Finch, *The Specific Heats and Resistivities of Molybdenum, Tantalum, and Rhenium from Low to Very High Temperatures* (Atomics International, 1961).

[271] S. Kravchenko, A. Burlakova, I. Domashnev, A. Vinokurov, and S. Shilkin, Nanosized vanadium diboride: Synthesis, structure, and properties, *Russian Journal of General Chemistry* **89**, 641 (2019).

[272] R. Kieffer, Mischkristallbildung bei hochschmelzenden metallischen hartstoffen, *Plansee Proc*, 1952, Reutte/Tirol, 283 (1953).

[273] K. Frisk and A. F. Guillermet, Gibbs energy coupling of the phase diagram and thermochemistry in the tantalum-carbon system, *Journal of alloys and compounds* **238**, 167 (1996).

[274] W. Bendick and W. Pepperhoff, The heat capacity of ti, v and cr, *Journal of Physics F: Metal Physics* **12**, 1085 (1982).

[275] R. Taylor, W. Kimbrough, and R. Powell, Thermophysical properties of tantalum, tungsten, and tantalum-10 wt. per cent tungsten at high temperatures, *Journal of the Less Common Metals* **24**, 369 (1971).

[276] G. Denman, *Recent Thermal Diffusivity Measurements of Tantalum-Tungsten and Hafnium-Tungsten Alloys*, Tech. Rep. (Air Force Materials Lab., Wright-Patterson AFB, Ohio, 1970).

[277] R. Taylor and J. Morreale, Thermal conductivity of titanium carbide, zirconium carbide, and titanium nitride at high temperatures, *Journal of the American Ceramic Society* **47**, 69 (1964).

[278] W. Lengauer, S. Binder, K. Aigner, P. Ettmayer, A. Guillou, J. Debuigne, and G. Groboth, Solid state properties of group ivb carbonitrides, *Journal of alloys and compounds* **217**, 137 (1995).

[279] Y. Zhang, Z. Wang, N. Li, Z. Che, X. Liu, G. Chang, J. Hao, J. Dai, X. Wang, F. Sun, *et al.*, Interfacial thermal conductance between cu and diamond with interconnected w- w2c interlayer, *ACS Applied Materials & Interfaces* **14**, 35215 (2022).

[280] F. Grønvold, S. Stølen, E. F. Westrum Jr, A. K. Labban, and B. Uhrenius, Heat capacity and thermodynamic properties of ditungsten carbide, w2c1- x, from 10 to 1000 k, *Thermochimica acta* **129**, 115 (1988).

[281] J. Jiang, Z. Shi, Arramel, J. Zhang, T. Deng, and N. Li, Temperature-dependent elastic and thermodynamic properties of zrc, hfc, and their solid solutions (zr0. 5hf0. 5) c, *Journal of the American Ceramic Society* **106**, 2024 (2023).

[282] J. Goss, R. Jones, M. Heggie, C. Ewels, P. Briddon, and S. Öberg, Theory of hydrogen in diamond, *Physical Review B* **65**, 115207 (2002).

[283] D. F. Johnson and E. A. Carter, Hydrogen in tungsten: Absorption, diffusion, vacancy trapping, and de-cohesion, *Journal of Materials Research* **25**, 315 (2010).

[284] P. Zhang, T. Wu, J. Tang, L. Deng, L. Wang, H. Deng, W. Hu, and X. Zhang, First-principles investigation of hydrogen interaction with cu/wc interface, *Computational Materials Science* **229**, 112422 (2023).

[285] C. Duan, Y.-L. Liu, H.-B. Zhou, Y. Zhang, S. Jin, G.-H. Lu, and G.-N. Luo, First-principles study on dissolution and diffusion properties of hydrogen in molybdenum, *Journal of nuclear materials* **404**, 109 (2010).

[286] X. Li, R. Zhao, C. Wan, T. Sui, and X. Ju, First-principles study on the hydrogen trapping by vacancy and substitutional helium in w–ta alloy, *Nuclear Materials and Energy* **36**, 101460 (2023).

[287] N. Fernandez, Y. Ferro, and D. Kato, Hydrogen diffusion and vacancies formation in tungsten: density functional theory calculations and statistical models, *Acta Materialia* **94**, 307 (2015).